TECHNISCHE UNIVERSITÄT WIEN
Vienna University of Technology

Diploma Thesis

Revision and assessment of a mechanobiologically regulated bone remodeling model, by means of model reduction, sensitivity and correlation analyses

submitted in satisfaction of the requirements for the degree of
Diplom-Ingenieur
of the TU Wien, Faculty of Civil Engineering

Diplomarbeit

Überarbeitung und Beurteilung eines mechanobiologisch geregelten Modells des Knochengewebeumbaus, mittels Modellvereinfachung, Sensitivitäts- und Korrelationsanalysen

ausgeführt zum Zwecke der Erlangung des akademischen Grades eines
Diplom-Ingenieurs
eingereicht an der Technischen Universität Wien, Fakultät für Bauingenieurswesen

von

Dipl.-Ing. Isabella Larcher
Matr.Nr.: 0826592

unter der Anleitung von

Associate Prof. Dipl.-Ing. Dr. techn. **Stefan Scheiner**

Institut für Mechanik der Werkstoffe und Strukturen
Technische Universität Wien
Karlsplatz 13/202, 1040 Wien

Wien, im Jänner 2020

Unterschrift

Abstract

Predicting the progress of bone remodeling by means of mathematical models has been one of the major challenges in bone research over the last decades. Bone cell population models seem to be a step in the right direction, but they often feature a large number of parameters, most of which cannot be directly measured experimentally. This deficit is the key obstacle for applying such models in clinical practice. In this thesis, the question is addressed whether bone cell population models can be effectively reduced and the role of single parameters is thoroughly scrutinized.

To that end, the coupled bone cell population/micromechanics model of Scheiner et al. (2013) is considered, which includes the well-known RANK/RANKL/OPG-regulatory pathway of bone remodeling. Originally, this model is based on 26 independent parameters, obtained by fitting and plausibility considerations. By merging parameters which occur in groups, this number could be reduced to 17, without compromising the versatility and reliability in any way. Furthermore, the revised model was subjected to comprehensive sensitivity analyses, based on varying only one, two, and three parameters at a time. This way, single parameters could be identified as hardly influential, while other parameters have turned out as very influential. Moreover, the sensitivity analyses suggest that the sensitivity behavior is partly considerably intricate, because for some parameter pairs the changes of the model predictions are qualitatively different, when varying both parameters at once (as compared to varying the parameters separately from each other). The situation gets even more complicated when varying three parameters at a time. Due to the multidimensionality of this problem, pattern recognition methods must be applied here, making interpretation of such sensitivity analyses difficult. Finally, the one-factor-at-a-time method was complemented by direct comparisons of the model prediction and curve fitting studies, and correlation analyses were performed.

In conclusion, this study provides some valuable new insights as to how complex, multiply interwoven mathematical models can be effectively studied and reduced. In further consequence, the results of the sensitivity studies could be utilized in terms of further model reductions, and of designing complementing experimental studies. It is believed that such kind of analysis is indispensible when eventually aspring acceptance of complex mathematical models by clinicians.

Kurzfassung

Den Verlauf des Knochenumbaus zu prognostizieren stellt in den letzten Jahrzehnten eine der größten Herausforderungen in der Knochenforschung dar. Zellpopulationsmodelle scheinen ein vielversprechendes Werkzeug zur Lösung dieses Problems zu sein. Diese beinhalten jedoch oft eine Vielzahl an Parametern, deren Werte zum Großteil nicht experimentell gemessen werden können, was sie momentan noch ungeeignet für den klinischen Gebrauch macht. Diese Diplomarbeit beschäftigt sich mit der Frage, ob Zellpopulationsmodelle im Hinblick auf die Anzahl ihrer Parameter effektiv reduziert werden können und untersucht den Einfluss einzelner Parameter.

Als Basis der Arbeit dient das Knochenumbau-Modell von Scheiner et al. (2013), das sowohl biochemische Faktoren als auch mechanische Reize in einem kombinierten Zellpopulations-/Mikromechanik-Modell berücksichtigt. Ursprünglich beruht dieses Modell auf 26 unabhängigen Parametern, welche durch Modell-Fitting unter Rücksichtnahme auf biologische Einschränkungen bestimmt wurden. Durch Zusammenfassen von Parametergruppen konnte die Anzahl der Parameter auf 17 reduziert werden, ohne dabei Einschränkungen bezüglich der Zuverlässigkeit oder Anwendbarkeit des Modells hinnehmen zu müssen. Weiters wurde das vereinfachte Modell einer umfassenden Sensitivitätsanalyse unterzogen, die auf Variation von je einem, je zwei und je drei Parametern zur gleichen Zeit beruht. Auf diese Weise konnten einzelne Parameter identifizert werden, die einen besonders großen bzw. kleinen Einfluss auf das Modell haben. Variation spezieller Parameterpaare ließen eine Veränderung des qualitativen Verhaltens des Modells erkennen (im Vergleich zu den Ergebnissen, die durch Variation der einzelnen Parameter erhalten wurden). Bei gleichzeitiger Variation von drei Parametern kamen weitere Wechselwirkungen zum Vorschein. Um dieses Problem systematisch behandeln zu können, müssen spezielle Techniken der Mustererkennung angewandt werden, was die Interpretation dieser Sensitivitätsanalysen sehr schwierig macht. Weiters wurde die sogenannte one-factor-at-a-time-Methode noch durch den direkten Vergleich der Modellresultate sowie durch Regressionsanalysen ergänzt. Außerdem wurde eine umfassende Korrelationsanalyse durchgeführt.

Zusammenfassend liefert diese Arbeit einige wertvolle neue Einblicke wie komplexe mathematische Modelle effektiv untersucht und vereinfacht werden können. In weiterer Konsequenz könnten die durch die Sensitivitätsanalyse erhaltenen Resultate als Grundlage für weitere Modellvereinfachungen dienen und einen Anstoß für weitere experimentelle Studien geben.

Acknowledgments

First of all, I want to thank my supervisor, Dr. Stefan Scheiner, for his support and the friendly and encouraging atmosphere that he provided throughout the whole process of writing my thesis. I enjoyed our discussions and I am thankful that he introduced me to the interesting topic of mathematical systems biology in the first place.

Furthermore, I want to thank my boyfriend, Philipp, who not only helped me with his excellent programming skills, but also with his constant support and care.

Finally, I want to thank my family for encouraging me throughout my whole life and for always being there for me.

Contents

Chapter 1

Introduction

Bone is a remarkable material which can, unlike standard engineering materials, react to changing environmental conditions, in terms of adapting its shape or composition. The underlying processes are usually termed bone modeling, when referring to externally triggered shape changes (such as thickening or thinning of bone organs), or bone remodeling, when referring to porosity changes within the bone substance. While the differences between bone modeling and remodeling are still debated and not fully clear yet (Seeman, 2009), both have in common a multiply interwoven mechanobiological regulation, stretching over several orders of magnitude in length scale (from the organ scale down to the subcellular scale), whereby the involved processes additionally feature significantly varying time scales (Carter and Beaupré, 2007; Martin et al., 1998; Mulvihill and Prendergast, 2010).

Understanding and being able to predict the above-mentioned processes is believed to be important for various problems in biomedical engineering, especially when it comes to the long-aspired goal of personalized medicine (Hamburg and Collins, 2010). Due to the involved intricacies, experimental studies provide only fragmentary insights, and simply connecting the experimentally revealed "dots" does not give access to the overall picture.

Owing to the significant advances in computer technology, due to which computer simulations have started to become a more and more capable vehicle, utilizing the latter strategy for predicting the behavior of bone (organs) in response to specific (mechanical and biochemical) initial and boundary conditions was identified as promising alternative in the 1980s, and substantially driven forward ever since (Mishnaevsky and Schmauder, 2001; Weinans et al., 1992; Yosibash et al., 2008). Essentially, two, so far more or less separated approaches have gained widespread acceptance. On the one hand, structural simulations on the macroscopic (organ) scale typically aim at relating specific mechanical loading regimes to corresponding macro- and microstruc-

tures changes in the studied bone organ (Hambli et al., 2011; Jacobs, 2000; Dejaco et al., 2012), whereas, on the other hand, material models, typically considering quasi-homogeneous representative volume elements (Holzapfel et al., 2000; Fritsch and Hellmich, 2007), aim at simulating the minute regulatory pathways, leading eventually to mechanobiological regulation. The last-mentioned material models are often based on comprehensive consideration of the involved regulatory pathways. While such models are undoubtedly sound and reasonable from a conceptual point of view, they are often based on a multitude of material and process parameters (Bertrand and Hellmich, 2009; Pivonka et al., 2013; Scheiner et al., 2014), most of which cannot be measured directly.

Hence, the question arises, whether models of bone (re-) modeling on the material scale are not unnecessarily extensive, or maybe even overdetermined. This thought has been the starting point of the research project described in this thesis. In particular, the hypothesis that mathematical bone remodeling models can be reduced in complexity without losing their validity and versatility has been pursued; considering for that purpose the model proposed by Scheiner et al. (2013).

This thesis is organized as follows: Chapter 2 presents the (generally accepted) fundamental basics of the mechanobiological processes which together constitute the process of bone remodeling, describing in particular the main players of the process, the sequence of the bone remodeling events in isolated manner, and possible irregularities leading to pathologies. In Chapter 3, the basis of this thesis, that is the combined bone cell population kinetics/micromechanics-model of Scheiner et al. (2013), is introduced in detail. Chapter 4 presents the attempt to reduce the model of Scheiner et al. (2013) in terms of the involved material and process parameters. In Chapter 5, the model is subjected to a comprehensive (one- and multidimensional) sensitivity analysis campaign in order to find out which parts of the model need to be calibrated and which not. Finally, correlation measures are computed, aiming at quantification of the parameter-dependence of the results. All results and insights are thoroughly discussed in Chapter 6, including also an outlook to potential follow-up future research directions.

Chapter 2

Molecular biology of bone remodeling

Bone remodeling relies on the well-balanced interactions between the two major bone cells, namely the bone-resorbing osteoclasts and the bone-forming osteoblasts, whereas osteocytes are considered to be the conductors of the cell-related processes, thereby influenced by their biochemical and mechanical environment. This dynamic process is important for various reasons. First of all, it is needed to substitute primary (infantile) bone with the mechanically more stable secondary bone. Furthermore, it constitutes the skeletal system's mechanism to heal microfractures in bone and to allow for an adequate calcium homeostasis (Rucci, 2008; Martin et al., 1998). If the highly coordinated process of bone remodeling is disturbed, mutations of the bone tissue may occur, potentially leading to severe skeletal pathologies. A particularly common one is osteoporosis, resulting from an excessive bone resorption by osteoclasts and an inadequate formation of new bone by osteoblasts. Therefore, osteoporosis leads to fragile bones potentially entailing an increased fracture risk (Kanis et al., 1994).

In addition to osteoblasts and osteoclasts, the process of bone remodeling involves many other protagonists, such as growth factors that are released from the bone matrix and signals from osteocytes and immune cells. Thus, to maintain this intact interplay between the immune and the skeletal system, a wide range of cell types and control mechanisms needs to be properly coupled (Hadjidakis and Androulakis, 2006; Raggatt and Partridge, 2010).

The bone remodeling process is often claimed to be performed by so-called basic multicellular units (BMUs), which are temporary anatomical units consisting of groups of bone cells that resorb and form bone. It appears to consist of five consecutive phases that take place asynchronously throughout the whole skeleton: quiescence, activation, resorption, reversal and formation (Sims and Martin, 2014; Raggatt and Partridge, 2010). Subsequently, the most important cells involved in bone remodeling are introduced and their functions and interactions are explained (Rucci, 2008).

2.1 Cells involved in bone remodeling

Osteoblasts are bone cells specialized in synthesizing bone tissue. They secrete bone matrix proteins (e.g. collagen type I, non-collagenous proteins, osteonectin, etc.), in order to lay down uncalcified bone matrix (osteoid) before provoking its subsequent mineralization. Furthermore, they express parathyroid hormone (PTH) receptors, which are crucial for regulating osteoclast differentiation. Osteoblastic cells occur in several maturation stages (see Figure 2.1). They are derived from mesenchymal stem cells through a multistep differentiation pathway, including immature osteoblast lineage cells, differentiating osteoblasts (pre-osteoblasts) and mature matrix-producing (active) osteoblasts (Raggatt and Partridge, 2010).

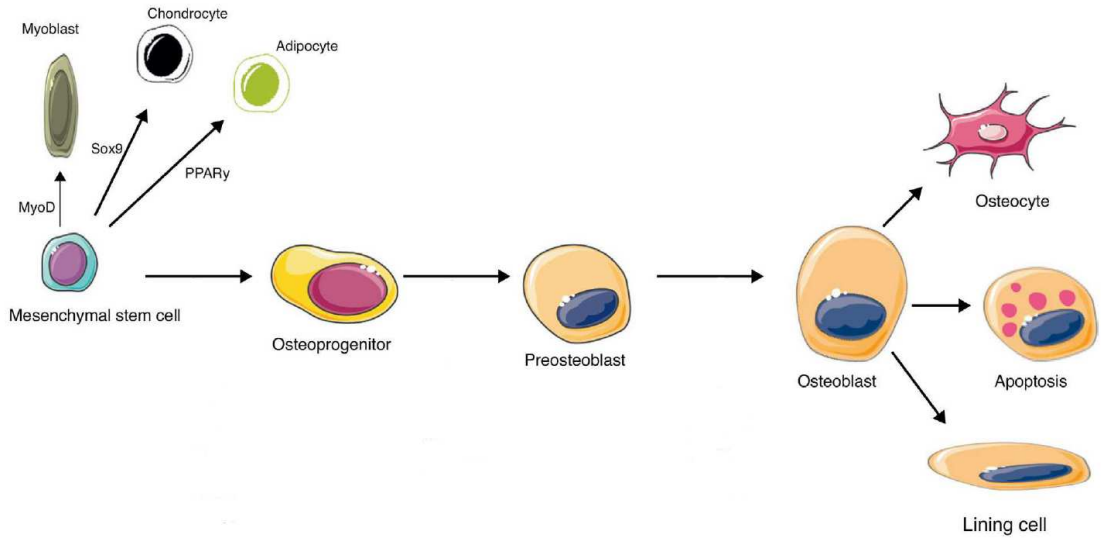

Figure 2.1: Differentiation stages of osteoblasts, adapted from **?**, governed by various factors, including myogenic differentiation 1 protein (MyoD), peroxisome proliferator-activated receptor gamma (PPARγ), sex determining region Y-box 9 Sox9).

After bone formation, osteoblasts are exposed to different scenarios. Some of them undergo apoptosis, while others become inactive bone lining cells. A subpopulation of osteoblasts becomes trapped by osteoid and constitute the so-called osteocytes that form a network throughout the mineralized bone (see Figure 2.1). In fact, osteocyctes represent the most abundant type of bone cells. They appear as spider-shaped cells embedded in so-called lacunar cells, evenly dispersed throughout the bone matrix and are connected with each other via their dendritic processes running through small canals called canaliculi. Besides their main function as mechanosensors, they perform other important functions, such as the regulation of phosphate and calcium homeostasis. After bone resorption, osteocytes are dissolved like the other components of the bone matrix (Bonewald, 2011; Del Fattore et al., 2012).

Osteoclasts are bone cells whose function is to remove mineralized bone matrix. They are polykarya possessing several nuclei, derived by fusion of mononuclear cells, called pre-osteoclasts (see Figure 2.2). Osteoclast differentiation starts with hematopoietic stem cells which give rise to colony-forming unit granulocytes/macrophages (CFU-M). These cells differentiate further into cells of the monocyte/macrophage lineage in the bone marrow, which are attracted to prospective resorption sites and then attach to the bone matrix to differentiate into osteoclasts in response to M-CSF and RANKL (Feng and McDonald, 2011). In order to dissolve bone, osteoclasts have to polarize and subsequently acidify the matrix and secrete proteolytic enzymes (Del Fattore et al., 2012). Once their resorption work is done they undergo apoptosis in order to avoid an excessive bone loss (Xing and Boyce, 2005).

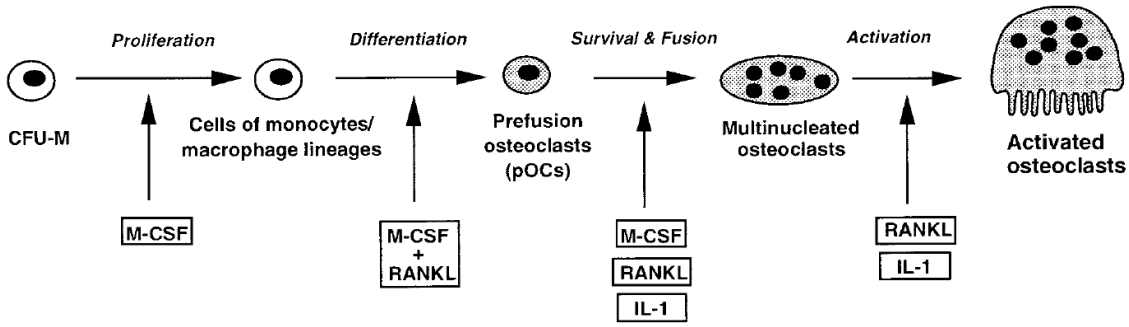

Figure 2.2: Differentiation stages of osteoclasts, adapted from Suda et al. (1999, Fig. 5), governed by various factors, including macrophage colony stimulating factor (M-CSF), interleukin 1 (IL-1), receptor activator of nuclear κB ligand (RANKL).

All bone cells work together, influence each other and are coupled in a highly organized cycle of bone removal and formation, consisting of five consecutive steps that are explained in the following, see also Figure 2.3.

2.2 Phases of Bone Remodeling

Quiescence. The first phase of bone remodeling is the so-called quiescence or resting phase. This is the stage in which the bone lining cells, which are actually inactive osteoblasts, remain attached to the bone surface.

Activation. The quiescence phase is followed by the activation phase, in which the aforementioned bone lining cells get activated by various inputs. This initiating remodeling signal can either be caused by micro-fractures that occur from mechanical loading (e.g. walking) and is sensed by osteocytes, or by an alteration in the release of factors, such as insulin growth factor-I (IGFI), tumor necrosis factor-α (TNF-α),

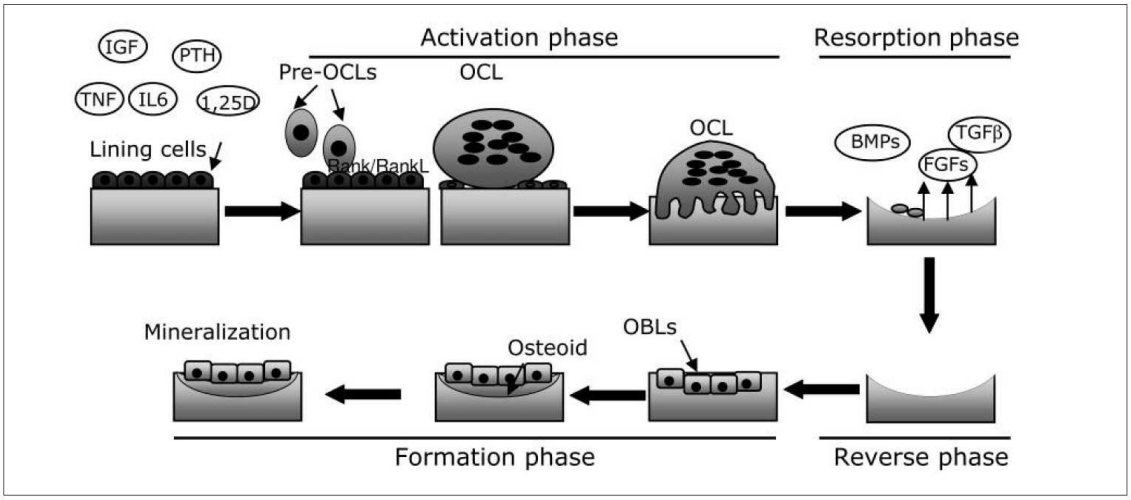

Figure 2.3: Scheme of the bone remodeling process, (Rucci, 2008, Fig. 2), governed by various factors, including insulin growth factor (IGF), parathyroid hormone (PTH), tumor necrosis factor (TNF), interleukin 6 (IL6), 1,25-dihydroxyvitamin (1,25D), osteoclasts (OCLs), bone morphogenetic proteins (BMPs), transforming growth factor β (TGF-β), fibroblast growth factors (FGFs), osteoblasts (OBLs).

parathyroid hormone (PTH) and interleukin-6 (IL-6). Under basal conditions, osteocytes secrete TGF-β, which inhibits osteoclastogenesis. Damaged bone or immobilization may lead to osteocyte apoptosis, which induces lowering of the TGF-β level and entails an amplified osteoclast population. Moreover, the binding of PTH to its receptors on osteoblastic cells, activates protein kinase A and C, as well as intracellular signaling pathways, resulting in a secretion of molecules which recruit osteoclast precursors and induce osteoclast differentiation and activation (Raggatt and Partridge, 2010).

The activated lining cells induce an increased expression of the TNF-related transmembrane cytokine RANKL (receptor activator of nuclear κB ligand), which is expressed by committed osteoblast progenitors and interacts with its membrane-bound receptor RANK (receptor activator of nuclear κB) that itself is expressed in osteoclast precursors. This interaction promotes proliferation of osteoclast precursors and triggers the fusion of these pre-osteoclasts to multinucleated osteoclasts. While the action of RANKL binding to RANK stimulates the differentiation and activation of osteoclasts, the soluble receptor osteoprotegerin (OPG) that is produced and released by osteoblasts acts as antagonist to RANKL. It binds to RANK and thereby inhibits the binding of RANKL to RANK and consequently also the formation of osteoclasts.

Notably, the discovery of the RANK/RANKL/OPG system was one of the most important advances in bone biology in the recent decade (Boyce and Xing, 2008).

Resorption. Additionally to the master osteoblastogenesis cytokines CSF-1 and RANKL, osteoblasts secrete matrix metalloproteinases (MMPs) in response to mechanical loading and endocrine remodeling signals. These MMPs degrade unmineralized osteoid that lines the bone surface and thereby expose Arg-Gly-Asp (RGD) attachment sites. Osteoclasts anchor these RGD-binding sites by means of integrin molecules and create the so-called "sealed zone", which is a dynamic microenvironment that defines the resorption area of the bone. Upon the release of hydrogen ions into the sealed zone, the mineralized matrix dissolves in the acidic space, which yields the Howship's resorption lacunae (Raggatt and Partridge, 2010). Once the organic part of the bone matrix is dissolved by means of acidification, lysosomal enzymes, such as cathepsin K and MMPs, are released to degrade the remaining organic components.

During bone resorption growth factors and other specific components that were embedded in the bone matrix are released. One particularly important growth factor is TGF-β, which is known for various functions. One effect of TGF-β is that it promotes osteoclast apoptosis in order to avoid an excessive bone loss once the resorption process dissolved a sufficient amount of the bone (Bonewald and Dallas, 1994; Lemaire et al., 2004).

Reversal. The osteoclastic bone resorption yields an undigested demineralised collagen matrix covering the surface of the bone. The so-called "reversal" cells, which are still of undetermined lineage, remove this debris produced during resorption. Due to the resorption process and some coupling signals produced by the reversal cells, growth factors (e.g. TGF-β) are released that induce a recruitment of osteoblasts to the site of resorption. Depending on the state of maturation of the osteoblasts TGF-β has different effects. It can cause an increased osteoblast recruitment and inhibit the differentiation into active osteoblasts. Thereby, TGF-β acts as coupling factor that links bone resorption to formation (Alliston et al., 2001; Erlebacher et al., 1998).

Formation. The precise coupling mechanism that coordinates the transition from reversal to bone formation is still not fully understood and allows for several reasonable hypotheses. It is likely that both direct contact and soluble signals may be involved. Under basal conditions osteocytes express sclerostin, which prevents Wnt signaling (Wnt being the so-called wingless gene), an inducer of bone formation. Due to mechanical loading and PTH the sclerostin expression is inhibited, and thus bone formation can occur (Raggatt and Partridge, 2010). Once osteoblast progenitors are

present at the resorption site they differentiate into active osteoblasts that secrete molecules, which facilitate the formation of osteoid. In order to finish the formation process hydroxyapatite is progressively incorporated into the newly formed osteoid, which implies mineralization, yielding eventually the material that is usually referred to as solid bone.

2.3 Behavior of bone cells during bone pathologies

The physiological process of bone remodeling can be disturbed by a variety of factors, including menopause-associated hormonal changes, age-related factors, changes in physical activity, drugs, and secondary diseases, leading to various bone disorders. One of the most abundant bone diseases is osteoporosis. It is characterized by a decrease in bone density (or, in other words, an increase in bone porosity), causing increased fragility and increased fracture risks, see Figure 2.4. Osteoporosis is classified into primary and secondary types (Feng and McDonald, 2011). Primary osteoporosis is further divided into two subtypes: Type I osteoporosis is better known as postmenopausal osteoporosis, which occurs frequently in postmenopausal women, initiated by the associated drop of the estrogen level.

In the 1980s, studies showed that osteoclast differentiation and activity are regulated by various cytokines, including interleukin-1 (IL-1), IL-6, and IL-7, and tumor necrosis factor (TNF). It appears that estrogen suppresses the express of these cytokines in monocytes and/or osteoblasts and stromal cells, leading to an increased bone resorption by means of distinct mechanisms (Feng and McDonald, 2011). While IL-6 increases osteoclastogenesis, IL-1 and TNF amplify the osteoclastic activity and provoke osteoclastogenesis indirectly by upregulating the expression of IL-6. Additionally, IL-1 and TNF also stimulate RANKL gene expression in osteoblasts and stromal cells, which as well entails an increased bone resorption. Furthermore, estrogen regulates the TGF-β level, thereby controlling the life span of osteoclasts. There are many further hypotheses concerning the influences of estrogen on the bone remodeling process (Felson et al., 1993; Kobayashi et al., 1996; Horsman et al., 1983).

Type II osteoporosis is also referred to as age-related osteoporosis and affects both men and women as a consequence of aging. Secondary osteoporosis characterizes bone disorders that are consequences of various other medical conditions (such as hypogonadism, endocrine disorders, gastro-intestinal (GI) diseases, transplantation, genetic disorders, and medications (Stein and Shane, 2003), or changes in physical activity (Raggatt and Partridge, 2010).

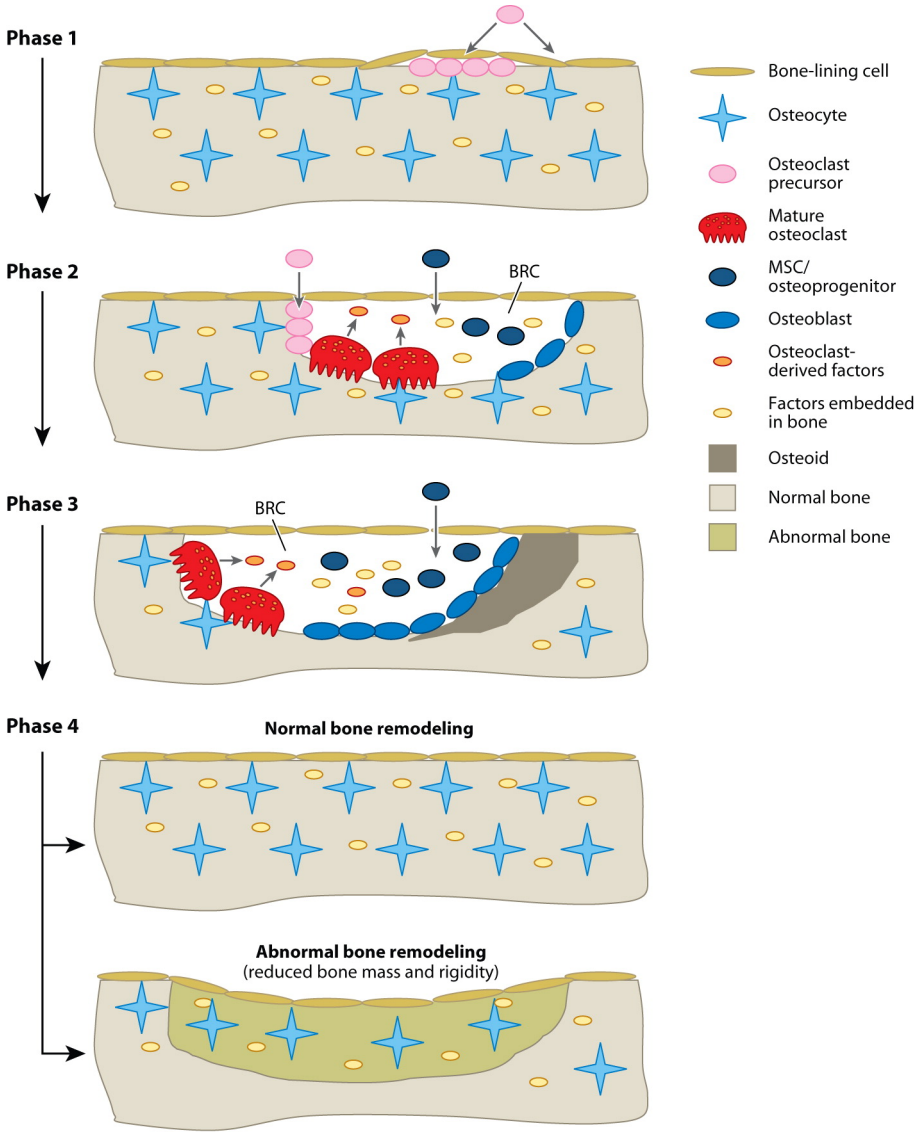

Figure 2.4: Schematic sketch of the sequence of bone remodeling stages, including both normal and pathological bone, adopted from (Feng and McDonald, 2011).

One of the major functions of bone remodeling is to adapt the bone mass and structural properties to the mechanical demands that are placed on the skeleton. A prolonged bed rest, immobilization as a consequence of paralysis or plaster casts, as well as a prolonged exposure to microgravity, reflects a decrease of the mechanical requirements. As a consequence, the mechanosensing pathways and corresponding signaling pathways that are involved in provoking bone formation are inactive, leading to a decreased bone mass and strength (Feng and McDonald, 2011). As the major mechanosensing cells, osteocytes play a crucial role in the pathogenesis of

immobilization-induced osteoporosis. However, several studies indicate that probably all bone cells respond in some way to mechanical loading (Papachroni et al., 2009; Rubin et al., 1999, 2002; Wiltink et al., 1995; Rubin et al., 2006; Saxena et al., 2011), although the precise mechanisms are not fully understood yet.

Apart from osteoporosis there are various other bone disorders, such as renal osteodystrophy (Hruska and Teitelbaum, 1995), Paget's disease (Ralston and Layfield, 2012), osteopetrosis (Tolar et al., 2004), or Rickets (Wharton and Bishop, 2003).

Chapter 3

Coupled model for bone remodeling simulation

3.1 Bone cell population model

In this chapter, the bone cell population model (BCPM) proposed by Scheiner et al. (2013) is presented. This model considers the hierarchical structure of bone and involves both biochemical and mechanobiological activator and repressor functions. The model equations are formulated for so-called (biochemical and mechanical) representative volume elements (RVEs), across which the cell concentrations and all related quantities are assumed to be uniform, hence transport can be neglected. Furthermore, the model considers populations of osteoblasts and osteoclasts (in distinct developmental stages), while osteocytes are not taken into account explicitly. The following three types of bone cells are contained as variable quantities (state variables), which are expressed in terms of molar concentrations:

- osteoblast precursor cells, C_{OB_p},
- active osteoblasts, C_{OB_a},
- active osteoclasts, C_{OC_a}.

As suggested in (Pivonka et al., 2008, 2010) the concentrations of the uncommitted osteoblast progenitor cells, C_{OB_u}, as well as the osteoclast precursor cells, C_{OC_p}, are kept constant, since they are assumed to be much larger than C_{OB_p}, C_{OB_a}, and C_{OC_a}. Throughout this thesis, the concentrations of these cell populations are set to $C_{OB_u} = 0.01$ pM and $C_{OC_p} = 0.001$ pM (picomolar, that is $10^{-12}\text{M} = 10^{-12}\frac{\text{mol}}{\text{l}}$) for all simulations. The steady-state concentrations of the state variables, and therefore also their initial values, are chosen to be $C_{OB_p}(t_0) = 0.001$ pM, $C_{OB_a}(t_0) = 0.0005$ pM, and $C_{OC_a}(t_0) = 0.0001$ pM (Scheiner et al., 2013).

The cellular development is governed by differentiation, proliferation, and apoptosis processes, regulated biochemically (via the RANK/RANKL/OPG-pathway, PTH and TGF-β), and biomechanically (driven by the bone matrix-scale strain energy density). Figure 3.1 summarizes the bone cell population model which describes the developments of the considered cell populations by the following three state equations:

$$\frac{dC_{OB_p}}{dt} = \mathcal{D}_{OB_u}\pi^{TGF-\beta}_{act,OB_u}C_{OB_u} + \mathcal{P}_{OB_p}\Pi^{mech}_{act,OB_p}C_{OB_p} - \mathcal{D}_{OB_p}\pi^{TGF-\beta}_{rep,OB_p}C_{OB_p}, \tag{3.1}$$

$$\frac{dC_{OB_a}}{dt} = \mathcal{D}_{OB_p}\pi^{TGF-\beta}_{rep,OB_p}C_{OB_p} - \mathcal{A}_{OB_a}C_{OB_a}, \tag{3.2}$$

$$\frac{dC_{OC_a}}{dt} = \mathcal{D}_{OC_p}\pi^{RANKL}_{act,OC_p}C_{OC_p} - \mathcal{A}_{OC_a}\pi^{TGF-\beta}_{act,OC_a}C_{OC_a}, \tag{3.3}$$

where $\mathcal{D}_{OB_u}$, $\mathcal{D}_{OB_p}$ and $\mathcal{D}_{OC_p}$ denote the differentiation rates of the respective bone cells, and $\mathcal{P}_{OBp}$ denotes the proliferation rate of osteoblast precursors, dictating the continuous redistribution of the concentrations among the individual cell types. $\mathcal{A}_{OB_a}$ and $\mathcal{A}_{OC_a}$ are the apoptosis rates of the active bone-forming and bone-resorbing cells, specifying the degree of decrease in the corresponding concentrations per unit time (day).

Additionally, differentiation and apoptosis are regulated by means of activator functions π_{act} and repressor functions π_{rep} (Pivonka et al., 2010), which are defined by so-called Hill functions. These functions are used to describe the fraction of a macromolecule that is saturated by a ligand as a function of the ligand concentration. It provides a measure for the degree of cooperativeness of the ligand binding to the enzyme or receptor. Typically, the function is a monotonic S-shaped function of the form (Alon, 2006)

$$f(X) = \frac{\beta X^n}{K^n + X^n}, \qquad \text{for activation,} \tag{3.4}$$

and

$$f(X) = \frac{\beta K^n}{K^n + X^n}, \qquad \text{for repression.} \tag{3.5}$$

Thereby, K denotes the activation/repression coefficient, which defines the concentration of active X that is needed for significant activation/repression. The parameter β is the maximum of the function, that is achieved for very large values of x, *i.e.* $X \gg K$. Finally, the Hill parameter n determines the steepness of the curve (see Figure 3.2); in this work, $n = 1$ for all Hill functions.

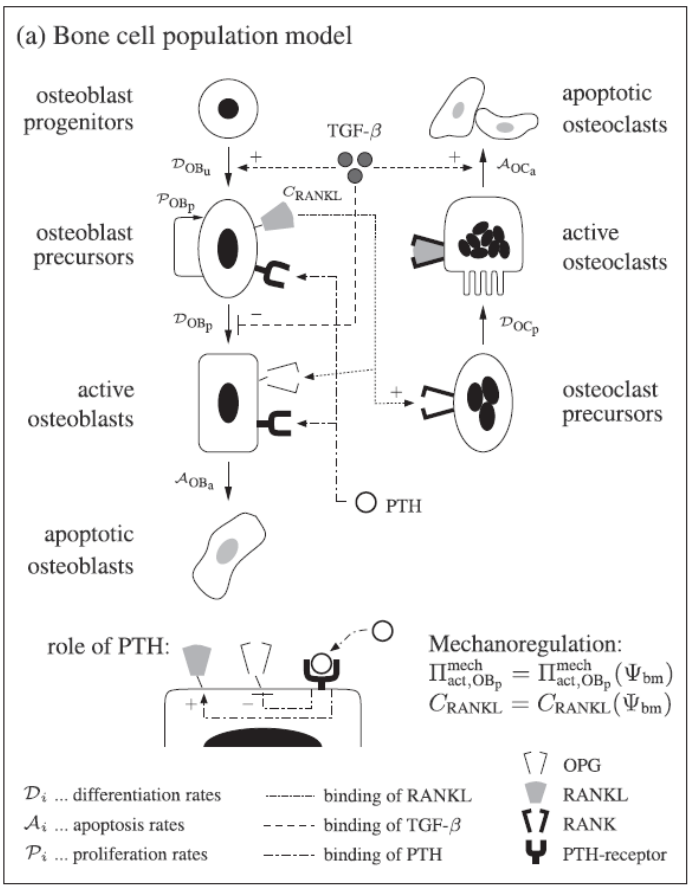

Figure 3.1: Scheme of the bone cell population model, adopted from (Scheiner et al., 2013).

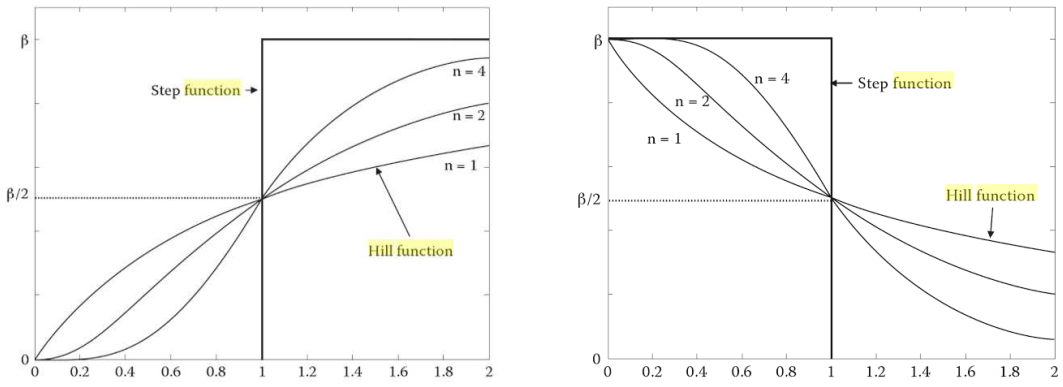

Figure 3.2: (a) Hill-type activator function, see Eq. (3.4), and (b) Hill-type repressor function, see Eq. (3.5), both evaluated for $n = 1, 2, 4$; images taken from (Alon, 2006).

The bone composition is quantified based on volume fractions of the involved constituents. In the considered RVE, fulfilling the separation-of-scales-requirement (Zaoui, 2002), bone tissue is assumed to be composed of extravascular bone matrix and vascular pore space. Changes in the relative amount of active osteoblasts and active osteoclasts over time lead to a change in the bone volume via

$$\frac{df_{bm}}{dt} = -k_{res}C_{OC_a} + k_{form}C_{OB_a}, \tag{3.6}$$

and

$$\frac{df_{vas}}{dt} = -\frac{f_{bm}}{dt} = k_{res}C_{OC_a} - k_{form}C_{OB_a}, \tag{3.7}$$

where f_{bm} and f_{vas} denote the volume fractions of the bone matrix and of the vascular pore space, respectively, *i.e.* $f_{bm} + f_{vas} = 1$. Throughout the simulations, the steady-state values $f_{vas}(t_0) = 0.05$ and $f_{bm}(t_0) = 0.95$ are used. As can be seen in Eqs. (3.6) and (3.7), the BCPM assumes the changes in the bone volume to be proportional to the number of active bone cells. The parameters k_{res} and k_{form} express the resorption/formation rates that quantify how much bone is resorbed by active osteoclasts and how much bone matrix is laid down by active osteoblasts per unit time, *i.e.* the percentage of change of the bone volume per pM cells per unit time (Pivonka et al., 2010).

In the steady state (at $t = t_0$), the bone volume should stay constant, *i.e.*

$$\frac{df_{bm}}{dt}(t_0) = -k_{res}C_{OC_a}(t_0) + k_{form}C_{OB_a}(t_0) = 0. \tag{3.8}$$

This condition directly implies $k_{form}C_{OB_a}(t_0) = k_{res}C_{OC_a}(t_0)$, which yields

$$k_{form} = k_{res} \cdot \frac{C_{OC_a}(t_0)}{C_{OB_a}(t_0)}. \tag{3.9}$$

3.1.1 Regulatory functions related to TGF-β

The BCPM considers receptors of TGF-β to be located on uncommitted osteoblast progenitors, osteoblast precursor cells, as well as on active osteoclasts. The action of TGF-β binding to its receptors on different cells leads to diverse responses. The binding to receptors on uncommitted osteoblast progenitors promotes their differentiation into osteoblast precursor cells, while the binding to receptors on pre-osteoblasts reduces their differentiation into active osteoblasts, see Eqs. (3.1) and (3.2). Moreover, the binding of TGF-β to receptors on active osteoclasts promotes osteoclast apoptosis, see Eq. (3.3). The activator and repressor functions representing the regulatory

effects of TGF-β read as (Pivonka et al., 2010)

$$\pi_{act,OB_u}^{TGF-\beta} = \frac{C_{TGF-\beta}}{K_{act,OB_u}^{TGF-\beta} + C_{TGF-\beta}}, \tag{3.10}$$

$$\pi_{rep,OB_p}^{TGF-\beta} = \frac{K_{rep,OB_p}^{TGF-\beta}}{K_{rep,OB_p}^{TGF-\beta} + C_{TGF-\beta}}, \tag{3.11}$$

and

$$\pi_{act,OC_a}^{TGF-\beta} = \frac{C_{TGF-\beta}}{K_{act,OC_a}^{TGF-\beta} + C_{TGF-\beta}}, \tag{3.12}$$

where $K_{act,OB_u}^{TGF-\beta}$, $K_{rep,OB_p}^{TGF-\beta}$ and $K_{act,OC_a}^{TGF-\beta}$ are the apparent equilibrium dissociation constants related to binding of TGF-β to its respective receptors. These parameters can be interpreted as activation/repression coefficients for differentiation and apoptosis, respectively.

The concentration of TGF-β, $C_{TGF-\beta}$, is given by

$$C_{TGF-\beta} = \frac{\alpha k_{res} C_{OC_a}}{\tilde{D}_{TGF-\beta}}, \tag{3.13}$$

with α denoting the constant measure for the TGF-β content in the bone matrix and $\tilde{D}_{TGF-\beta}$ denoting the constant degradation rate of TGF-β.

Note that in the BCPM, the release rate of TGF-β from the bone matrix by active osteoclasts is assumed to be constant, while in general it could be a function of space and time.

3.1.2 Regulatory functions related to the RANK/RANKL/OPG-system

Equation (3.3) contains one further Hill-function-shaped activator function, namely π_{act,OC_p}^{RANKL}. This function incorporates the action of RANKL binding to RANK, which is expressed on osteoclast precursor cells. It promotes their differentiation into active osteoclasts and reads as

$$\pi_{act,OC_p}^{RANKL} = \frac{C_{[RANKL-RANK]}}{K_{act,OCp}^{RANK-RANKL} + C_{[RANKL-RANK]}}, \tag{3.14}$$

where $C_{[RANKL-RANK]}$ denotes the concentration of the RANKL-RANK complex, and $K_{act,OCp}^{RANK-RANKL}$ is the apparent dissociation equilibrium constant related to binding of RANKL to RANK (interpretable as activation coefficient for osteoclast precursor differentiation). $C_{[RANKL-RANK]}$ follows straightforwardly from

$$C_{[RANKL-RANK]} = K_{a,[RANKL-RANK]} C_{RANKL} C_{RANK}. \tag{3.15}$$

where $K_{a,[RANKL-RANK]}$ is the equilibrium association constant related to binding of RANKL to RANK. C_{RANK} denotes the concentration of RANK which is assumed to be proportional to the amount of osteoclast precursors (since the RANK-receptors are found on their membranes), and described via

$$C_{RANK} = 10^4 \cdot C_{OC_p}. \tag{3.16}$$

The proportionality factor 10^4 describes how much RANK is produced per cell ([pM/pM]). C_{RANKL}, denoting the concentration of RANKL that is available for binding onto RANK, is given by (Pivonka et al., 2008)

$$C_{RANKL} = \frac{C^{\max}_{RANKL} \frac{\beta_{RANKL}+P_{RANKL}}{\beta_{RANKL}+\tilde{D}_{RANKL}C^{max}_{RANKL}}}{1 + K_{a,[RANKL-OPG]}C_{OPG} + K_{a,[RANKL-RANK]}C_{RANK}}, \tag{3.17}$$

where $K_{a,[RANKL-OPG]}$ denotes the equilibrium association constant for binding OPG to RANKL, β_{RANKL} is the intrinsic RANKL production rate and $\tilde{D}_{RANKL}$ denotes the constant degradation rate of RANKL. P_{RANKL} is the external dosage term of RANKL, which arises from mechanical loading and will be explained later in Section 3.1.4. C_{OPG} denotes the concentration of OPG given below in Eq. (3.19) and C^{max}_{RANKL} denotes the maximum concentration of RANKL that is regulated by PTH in the following way:

$$C^{max}_{RANKL} = N^{OB_p}_{RANKL}\pi^{PTH}_{act,OB} \cdot C_{OB_p}. \tag{3.18}$$

The dependence on C_{OB_p} in Eq. (3.18) arises from the fact that RANKL is assumed to be produced by osteoblast precursors only. The factor $N^{OB_p}_{RANKL}$ in Eq. (3.18) denotes the maximum number of RANKL receptors on osteoblast precursors and $\pi^{PTH}_{act,OB}$ presents a Hill-typed regulatory considering that PTH promotes the availability of RANKL, see Eq. (3.21).

The concentration of OPG, C_{OPG}, occurring in Eq. (3.17) is given by

$$C_{OPG} = \frac{\beta_{OPG}C^{max}_{OPG}}{\beta_{OPG} + \tilde{D}_{OPG}C^{max}_{OPG}}, \tag{3.19}$$

with C^{max}_{OPG} being the maximum OPG concentration, $\tilde{D}_{OPG}$ being the constant OPG degradation rate and β_{OPG} denoting the intrinsic OPG production rate, which itself is determined by

$$\beta_{OPG} = p^{OPG}_{OB}\pi^{PTH}_{rep,OB}C_{OB_a}. \tag{3.20}$$

Thereby p^{OPG}_{OB} is the maximum OPG-production rate per active osteoblast, and $\pi^{PTH}_{rep,OB}$ is the PTH-related, Hill-typed repression function, see Eq. (3.22).

3.1.3 Regulatory functions related to PTH

Eqs. (3.18) and (3.20) include Hill-type activation and repression functions governed by PTH, which read as

$$\pi_{act,OB}^{PTH} = \frac{C_{PTH}}{K_{act,OB}^{PTH} + C_{PTH}}. \tag{3.21}$$

and

$$\pi_{rep,OB}^{PTH} = \frac{K_{rep,OB}^{PTH}}{K_{rep,OB}^{PTH} + C_{PTH}}. \tag{3.22}$$

Here $K_{act,OB}^{PTH}$ and $K_{rep,OB}^{PTH}$ denote the apparent equilibrium dissociation constants related to the binding of PTH to its receptors, which can be interpreted as activation coefficient for the maximum RANKL production, and repression coefficient for the production of OPG, respectively. Finally, C_{PTH} denotes the constant concentration of PTH, defined by the fraction of the intrinsic PTH production rate β_{PTH} and the PTH degradation rate $\tilde{D}_{PTH}$, *i.e.*

$$C_{PTH} = \frac{\beta_{PTH}}{\tilde{D}_{PTH}}. \tag{3.23}$$

Note that C_{PTH}, and thus also $\pi_{act,OB}^{PTH}$ and $\pi_{rep,OB}^{PTH}$, are constant functions. Thus, the intrinsic OPG production rate β_{OPG}, that is defined in Eq. (3.20), is proportional to C_{OB_a}. This reflects the fact that the BCPM assumes OPG to be exclusively produced by active osteoblasts.

It can easily be seen that the majority of the equations of the BCPM (and therefore also the majority of the model parameters) are needed to describe the signaling pathway of RANK-RANKL-OPG. In (Pivonka et al., 2010), it has been shown that this pathway is highly important for diseases that induce bone loss due to an increased osteoclastic resorption, such as osteoporosis.

3.1.4 Mechanically driven regulatory functions

The model proposed by (Scheiner et al., 2013) includes two mechanobiological regulatory mechanisms. On the one hand, $\mathcal{P}_{OB_p}$, which denotes the maximum proliferation rate of osteoblast precursors, is regulated by means of an activator function Π_{act,OB_p}^{mech} that restricts the proliferation rate depending on the mechanical strains in the extravascular bone matrix. Low strains reduce the proliferation rate, while for high strains the maximum proliferation $\mathcal{P}_{OB_p}$ is achieved. As a measure for the strains in the extravascular matrix the strain energy density (SED) Ψ_{bm} is chosen; note that computation of Ψ_{bm} is described in Section 3.2. Thus, Π_{act,OB_p}^{mech} is a continuous function

of the SED Ψ_{bm} that is defined stepwise by

$$\Pi^{mech}_{act,OB_p}(\Psi_{bm}) = \begin{cases} 0.5 & \text{for } \frac{\Psi_{bm}}{\Psi_{bm_0}} < 1 \\ 0.5 \cdot \left[1 + \lambda \left(\frac{\Psi_{bm}}{\Psi_{bm_0}} - 1\right)\right] & \text{for } 1 \leq \frac{\Psi_{bm}}{\Psi_{bm_0}} \leq \frac{1}{\lambda} + 1 \\ 1 & \text{for } \frac{\Psi_{bm}}{\Psi_{bm_0}} > \frac{1}{\lambda} + 1 \end{cases}. \tag{3.24}$$

The parameter λ is called "anabolic strength parameter" and determines for which increase of Ψ_{bm} from the initial value Ψ_{bm_0} the maximum of the function, *i.e.* $\Pi^{mech}_{act,OB_p} = 1$, and therefore the maximum proliferation $\mathcal{P}_{OB_p}$, is reached (see Figure 3.3). Throughout the simulations this anabolic strength parameter is set to $\lambda = 1.25$, which relates to the physiological behavior of bone during osteoporosis and disuse scenarios (Scheiner et al., 2013).

The value of the maximum proliferation rate itself is determined in the steady state case via (Scheiner et al., 2013)

$$\mathcal{P}_{OB_p} = \frac{\mathcal{D}^{Pivonka}_{OB_u} C_{OB_u} \pi^{TGF-\beta}_{act,OB_u}}{0.5 \cdot C_{OB_p}(t_0)} \cdot a_{\mathcal{P}_{OB_p}}, \tag{3.25}$$

and held constant during the simulations. The parameter $a_{\mathcal{P}_{OB_p}}$ in Eq. (3.25) is called "preosteoblastic proliferation fraction", and describes the fraction of gain of osteoblast precursor cells by proliferation compared to the gain by differentiation, and for physiological conditions, is set to $a_{\mathcal{P}_{OB_p}} = 0.1$. The parameter $\mathcal{D}^{Pivonka}_{OB_u}$ is taken from Pivonka et al. (2008) and reads as $\mathcal{D}^{Pivonka}_{OB_u} = 7 \cdot 10^{-2}$ pM/day.

Additionally, strains in the bone matrix lead to a decreased RANKL expression, which is implemented in the model by means of a RANKL dosage term P_{RANKL}. This dosage term is again a function of the SED Ψ_{bm} and reads as

$$P_{RANKL}(\Psi_{bm}) = \begin{cases} \kappa \left(1 - \frac{\Psi_{bm}}{\Psi_{bm_0}}\right) & \text{for } \frac{\Psi_{bm}}{\Psi_{bm_0}} < 1 \\ 0 & \text{for } \frac{\Psi_{bm}}{\Psi_{bm_0}} > 1 \end{cases}, \tag{3.26}$$

where κ is a so-called inhibition parameter. In (Scheiner et al., 2013), the parameter κ has been investigated thoroughly and it has been observed that for $\kappa = 10^5$ the model results fit the actual behavior of bone exposed to decreased mechanical loading best.

In Table 3.1 all the model parameters are summarized together with their values and units.

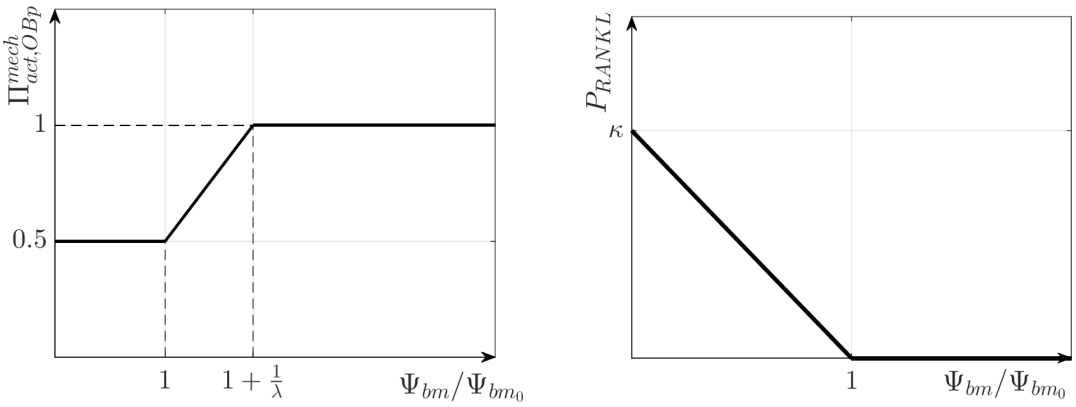

(a) Π^{mech}_{act,OB_p} (b) P_{RANKL}

Figure 3.3: Sketch of (a) the mechanical proliferation activator function, Π^{mech}_{act,OB_p}, and (b) the mechanically regulated dosage function of RANKL, P_{RANKL}.

Table 3.1: Parameters of the bone cell population model, as suggested in (Scheiner et al., 2013).

Parameter	Numerical value	Unit
$\mathcal{A}_{OB_a}$	$2.1107 \cdot 10^{-1}$	pM/day
$\mathcal{A}_{OC_a}$	5.6487	pM/day
$\mathcal{D}_{OB_u}$	$6.3 \cdot 10^{-2}$	pM/day
$\mathcal{D}_{OB_p}$	$1.657 \cdot 10^{-1}$	pM/day
$\mathcal{D}_{OC_p}$	2.1	pM/day
C^{max}_{OPG}	$2 \cdot 10^{8}$	pM
$\tilde{D}_{OPG}$	$3.5 \cdot 10^{-1}$	day^{-1}
$\tilde{D}_{PTH}$	$8.6 \cdot 10$	day^{-1}
$\tilde{D}_{RANKL}$	$1.0132 \cdot 10$	day^{-1}
$\tilde{D}_{TGF-\beta}$	1	day^{-1}
k_{res}	2	$(\text{pM day})^{-1}$
$K^{TGF-\beta}_{act,OB_u}$	$5.6328 \cdot 10^{-4}$	pM
$K^{PTH}_{act,OB}$	$1.5 \cdot 10^{2}$	pM
$K^{TGF-\beta}_{act,OC_a}$	$5.6328 \cdot 10^{-4}$	pM
$K^{RANKL-RANK}_{act,OCp}$	5.6797	pM
$K_{a,[RANKL-RANK]}$	$3.4117 \cdot 10^{-2}$	pM^{-1}
$K_{a,[RANKL-OPG]}$	$1 \cdot 10^{-3}$	pM^{-1}
$K^{PTH}_{rep,OB}$	$2.2258 \cdot 10^{-1}$	pM
$K^{TGF-\beta}_{rep,OB_p}$	$1.7543 \cdot 10^{-4}$	pM
$N^{OB_p}_{RANKL}$	$2.7035 \cdot 10^{6}$	
p^{OPG}_{OB}	$1.6249 \cdot 10^{8}$	day^{-1}
α	0.5	pM
β_{PTH}	$2.5 \cdot 10^{2}$	pM/day
β_{RANKL}	$1.6841 \cdot 10^{2}$	pM/day
$\mathcal{P}_{OBp}$	$2.1107 \cdot 10^{-2}$	1/day
k_{form}	$4 \cdot 10^{-1}$	$(\text{pM day})^{-1}$

3.2 Mechanoregulation through scaling of strains

In this section, the relation between the macroscopic strains that act on a piece of cortical bone and the corresponding microscopic strains in the extravascular matrix are explained. These microscopic strains contribute to the strain energy density Ψ_{bm}, which is used as input argument for the mechanoregulating functions Π^{mech}_{act,OB_p} and P_{RANKL}, see Eqs. (3.24) and (3.26). In order to briefly describe the employed concept of continuum micromechanics for computation of Ψ_{bm}, the respective description provided in (Scheiner et al., 2013) is reiterated, reading as follows: In continuum micromechanics (Hill, 1963, 1965; Zaoui, 2002) a material is understood as a macro-homogeneous, but micro-heterogeneous body filling a rep- resentative volume element (RVE) with characteristic length l_{RVE}, $l_{RVE} \gg d_{RVE}$, d_{RVE} representing the characteristic length of inhomogeneities within the RVE, and $l_{RVE} \ll \{\mathcal{L}, \mathcal{P}\}$, $\mathcal{L}$ representing the characteristic length of the geometry and $\mathcal{P}$ representing the characteristic length of the loading of a structure built up by the material defined on the RVE. In general, the microstructure within one RVE is so complicated that it cannot be described in complete detail. Therefore, quasi-homogeneous subdomains with known physical properties are reasonably chosen. They are called material phases. The homogenized (upscaled) elastic behavior of the material on the observation scale of the RVE, *i.e.* the relation between homogeneous deformations acting on the boundary of the RVE and resulting macroscopic (average) stresses, can then be estimated from the elastic behavior of the material phases, their volume fractions within the RVE, their characteristic shapes, and their interactions. We choose the characteristic length of the RVE such that cortical bone is reasonably represented as two-phase composite material (Hellmich et al., 2008): Fluid-filled, vascular pore space is morphologically approximated by cylindrical inclusions in the extravascular (solid) bone matrix. The overall constitutive behavior is anisotropic, stemming, on the one hand, from (i) the anisotropic orientation of the pore space (Fritsch and Hellmich, 2007; Hellmich et al., 2004; Hellmich, 2005), and, on the other hand, from (ii) the anisotropic constitutive behavior of the extravascular bone matrix (Lees et al., 1983, 1990; Turner et al., 1999).

Then, in the framework of continuum mechanics, the homogenized fourth-order stiffness tensor of cortical bone is given by

$$\mathbb{C}^{hom}_{cort} = \sum_r f_r \mathbb{c}_r : \mathbb{A}^{est}_r, \tag{3.27}$$

where the sum is over the different constituents r = vas, bm, and $\mathbb{c}_r$ denotes the respective microscopic fourth-order stiffness tensor, and $\mathbb{A}^{est}_r$ is the estimate of the corresponding fourth-order strain concentration tensor. In the present case, it is

derived based on the Mori-Tanaka scheme, reading as

$$\mathbb{A}_r^{est} = [\mathbb{I} + \mathbb{P}_r^{bm} : (\mathbb{c}_r - \mathbb{c}_{bm})]^{-1} : \left\{ \sum_s f_s [\mathbb{I} + \mathbb{P}_s^{bm} : (\mathbb{c}_s - \mathbb{c}_{bm})]^{-1} \right\}^{-1}, \tag{3.28}$$

where the sum is again over both phases $s =$ vas, bm, while $\mathbb{I}$ denotes the fourth-order unit tensor, and $\mathbb{P}_r^{bm}$ is the fourth-order Hill-tensor of phase r embedded in a matrix with stiffness $\mathbb{c}_{bm}$, which is given by (Scheiner et al., 2013),

$$\mathbb{c}_{bm} = \begin{pmatrix} 18.5 & 10.3 & 10.4 & 0 & 0 & 0 \\ 10.3 & 20.8 & 11.0 & 0 & 0 & 0 \\ 10.4 & 11.0 & 28.4 & 0 & 0 & 0 \\ 0 & 0 & 0 & 12.9 & 0 & 0 \\ 0 & 0 & 0 & 0 & 11.5 & 0 \\ 0 & 0 & 0 & 0 & 0 & 9.3 \end{pmatrix} \text{GPa}. \tag{3.29}$$

For a detailed explanation how the Hill tensor of a cylindrical phase (such as vascular pore space) is calculated, see (Hellmich et al., 2008; Fritsch et al., 2006). The stiffness tensor of the vascular porosity reads as

$$\mathbb{c}_{vas} = 3k_{H_2O}\mathbb{K} + 2\mu_{H_2O}\mathbb{J}, \tag{3.30}$$

with $k_{H_2O} = 2.3$ GPa as the bulk modulus, $\mu_{H_2O} = 0$ as the shear modulus, and $\mathbb{K}$ and $\mathbb{J}$ as the volumetric and the deviatoric part of the fourth-order unit tensor $\mathbb{I}$,

$$\mathbb{K} = \frac{1}{3} \cdot \begin{pmatrix} 1 & 1 & 1 & 0 & 0 & 0 \\ 1 & 1 & 1 & 0 & 0 & 0 \\ 1 & 1 & 1 & 0 & 0 & 0 \\ 0 & 0 & 0 & 0 & 0 & 0 \\ 0 & 0 & 0 & 0 & 0 & 0 \\ 0 & 0 & 0 & 0 & 0 & 0 \end{pmatrix}, \tag{3.31}$$

and $\mathbb{J} = \mathbb{I} - \mathbb{K}$.

Using the linear elastic constitutive law

$$\boldsymbol{\Sigma}_{cort} = \mathbb{C}_{cort}^{hom} : \boldsymbol{E}_{cort}, \tag{3.32}$$

one can determine the strain tensor of the extravascular bone matrix via

$$\boldsymbol{\varepsilon}_{bm} = \mathbb{A}_{bm}^{est} : \boldsymbol{E}_{cort} = \mathbb{A}_{bm}^{est} : \left[(\mathbb{C}_{cort}^{hom})^{-1} : \boldsymbol{\Sigma}_{cort} \right], \tag{3.33}$$

for a given macroscopic stress tensor $\boldsymbol{\Sigma}_{cort}$.

Finally, the microscopic SED Ψ_{bm} reads as

$$\Psi_{bm} = \frac{1}{2}\boldsymbol{\varepsilon}_{bm} : \mathbb{C}_{bm} : \boldsymbol{\varepsilon}_{bm}. \tag{3.34}$$

Figure 3.4 summarizes the basic idea of the mechanoregulation in the BCPM.

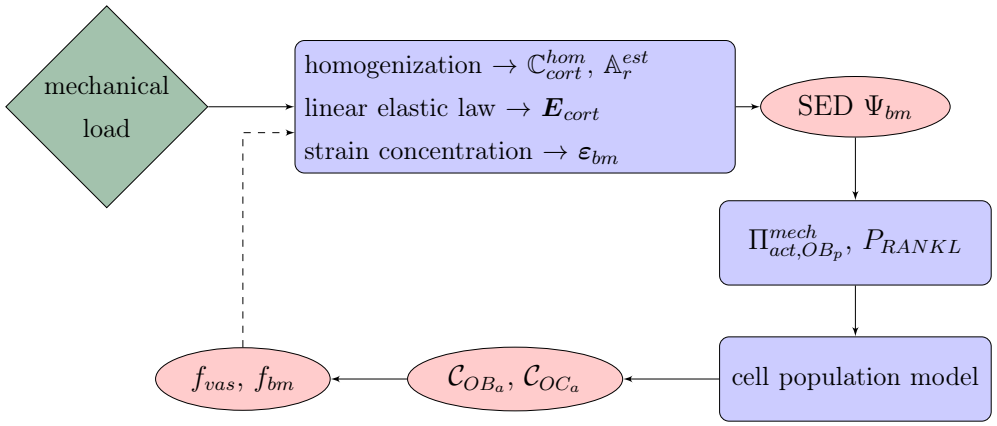

Figure 3.4: Scheme of the realization of the mechanoregulation in our model.

The subsequent sections introduce two scenarios that lead to an increased bone resorption and therefore to an amplified bone porosity inducing a higher fracture risk, namely postmenopausal osteoporosis and a microgravity-induced disuse scenario. After giving a brief explanation as to how these scenarios are implemented within the BCPM, the thereby obtained results are presented as well as interpreted.

3.2.1 Mechanobiological regulation in postmenopausal osteoporosis

Osteoporosis is among the ten most frequent diseases worldwide. According to recent statistics from the International Osteoporosis Foundation (IOF), worldwide, 1 in 3 women over the age of 50 years and 1 in 5 men suffer a fracture caused by osteoporosis (Sözen et al., 2017). The disease is characterized by skeletal fragility and microarchitectural deterioration (Black and Rosen, 2016). As mentioned in Section 2.3, experiments indicate that PMO is accompanied by changes within the RANK-RANKL-OPG system. In (Lemaire et al., 2004) it is suggested that these changes can be modeled by adding a PTH dosage term $P_{PTH,PMO} = 5 \cdot 10^4$ pM/day that is initiated at $t = t_0$ altering Eq. (3.23) in the following way (Scheiner et al., 2013):

$$C_{PTH} = \frac{\beta_{PTH} + P_{PTH,PMO}}{\tilde{D}_{PTH}}. \tag{3.35}$$

For the simulations of the osteoporosis scenario a constant loading with

$$\Sigma_{cort}^{normal} = \begin{pmatrix} 0 & 0 & 0 \\ 0 & 0 & 0 \\ 0 & 0 & -30 \end{pmatrix} \text{MPa} \tag{3.36}$$

is considered.

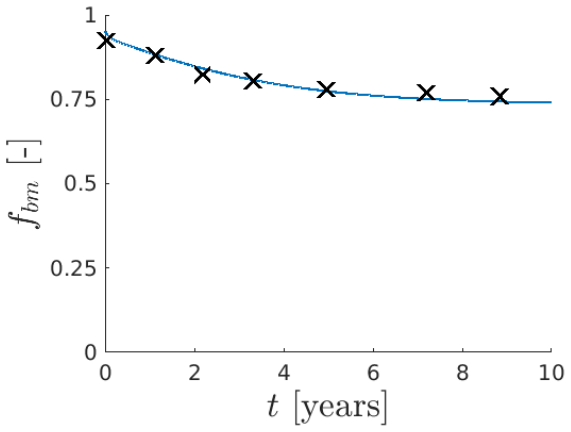

Figure 3.5: Numerical simulation of the volume fraction f_{bm} over ten years under conditions representing osteoporosis. The crosses indicate the experimental results (Bonnet and Ferrari, 2010).

Figure 3.5 shows the development of the bone matrix volume fraction of a woman suffering from osteoporosis. As in (Scheiner et al., 2013, Fig. 5) the experimental results shown by Bonnet and Ferrari (2010) are presented by the crosses in Figure 3.5. These results arose from studies on the bone mass evolution averaged over the whole skeleton. Thus, it is very difficult to validate the accuracy of the BCPM with these data. However, it can be seen that qualitatively the behavior of the model closely resembles the *in vivo* loss of bone matrix suggested by Bonnet and Ferrari (2010).

3.2.2 Mechanobiological regulation in microgravity-induced disuse

Bone features remarkable capabilities in terms of adapting to a changing environment. In order to do so, it grows more densely in areas where high stresses are experienced, while it resorbs bone matrix in areas experiencing lower stresses. Astronauts that are exposed to microgravity for long times therefore often suffer a severe decrease in bone mass and density, which is accompanied with higher fracture risks and thus represents a serious issue for their health. In order to simulate a disuse scenario, the loading

during the first 2000 days ($0 \leq t \leq 2000$) is reduced to

$$\Sigma_{cort}^{disuse} = \begin{pmatrix} 0 & 0 & 0 \\ 0 & 0 & 0 \\ 0 & 0 & -25 \end{pmatrix} \text{MPa}. \tag{3.37}$$

After these 2000 days, the loading is set back to Σ_{cort}^{normal}, see Eq. (3.36), and the simulation continues for further 8000 days (*i.e.* 10000 days in total).

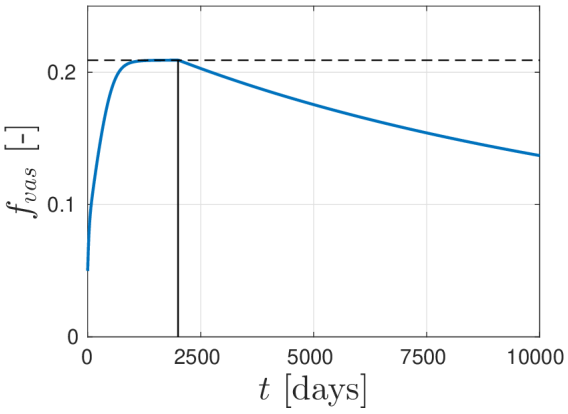

Figure 3.6: Computed development of the volume fraction f_{vas} over a time period of 10000 days for the disuse scenario introduced in Eq. (3.37).

The model responses to the disuse scenario are visualized in Figure 3.6. The disuse that is expressed by a decreased stress leads to the initial drop of the microscopic strain energy density, Ψ_{bm}. This drop leads on the one hand to an increased production of RANKL, see Eq. (3.26), which itself causes an amplified osteoclast activity, and on the other hand to a decreased proliferation of osteoblast precursors (see Eq. (3.1)). Altogether, the result is an increased bone resorption that explains the increase of the volume fraction of vascular pore space in Figure 3.6(c), see Eq. (3.7). As a consequence of the increased amount of vascular pore space, the RVE gets more compliant, *i.e.*, the macroscopic stiffness decreases. A decrease of the stiffness results in an increased deformation. Consequently, the strain energy density Ψ_{bm} increases, as can be observed in Figure 3.6(a). Figure 3.6 shows that the model reaches a new equilibrium after approximately 1000 days, where the volume fraction of the vascular pore space does not increase any more, but stays on an amplified constant level. After 2000 days, when the macroscopic stress it reset to its normal value, the SED immediately increases, which induces the exact contrary effect, namely the proliferation rate of osteoblast precursors is increased and there is no additional RANKL production based on Eq. (3.26). Thus, the mechanical steady state slowly returns to its original state with $f_{vas} = 0.05$.

Chapter 4

Revised bone remodeling model

In the previous chapter, the bone remodeling model that has been established in (Pivonka et al., 2008), together with the extension of mechanoregulation that was introduced in (Scheiner et al., 2013), has been presented. The results of the model fit reasonably well to experimental data, and therefore it seems to describe the fundamental mechanisms of bone remodeling accurately. However, it comprises a multitude of model parameters whose individual values are not accessible experimentally. Thus, the values have to be chosen merely based on plausibility considerations. Of course one can not exclude the possibility of there being other parameter values that would yield a similar (or even better) output. The goal of this chapter is to considerably reduce the number of parameters without changing the mechanism and the accuracy of the model.

4.1 Revised regulatory functions related to TGF-β

By inserting the definition of $C_{TGF-\beta}$ according to Eq. (3.13) into Eqs. (3.10) to (3.12) the Hill functions that represent the activator and repressor functions related to TGF-β can be simplified to

$$\pi_{act}^{TGF-\beta} = \frac{C_{OC_a}}{R_{act}^{TGF-\beta} + C_{OC_a}}, \tag{4.1}$$

and

$$\pi_{rep}^{TGF-\beta} = \frac{R_{rep}^{TGF-\beta}}{R_{rep}^{TGF-\beta} + C_{OC_a}}, \tag{4.2}$$

where the new parameters $R_{act}^{TGF-\beta}$ and $R_{rep}^{TGF-\beta}$ are defined as

$$R_{act}^{TGF-\beta} = \frac{K_{act}^{TGF-\beta}\tilde{D}_{TGF-\beta}}{\alpha k_{res}} = 5.6328 \times 10^{-4} \text{ pM}, \tag{4.3}$$

and

$$R_{rep}^{TGF-\beta} = \frac{K_{rep,OB_p}^{TGF-\beta}\tilde{D}_{TGF-\beta}}{\alpha k_{res}} = 1.7543 \times 10^{-4} \text{ pM}. \tag{4.4}$$

It is emphasized that one does not longer distinguish between the two TGF-β activation functions $\pi_{act,OB_u}^{TGF-\beta}$ and $\pi_{act,OC_a}^{TGF-\beta}$, since they were chosen to be identical anyway in the original model. Therefore, by setting $K_{act}^{TGF-\beta} = K_{act,OB_u}^{TGF-\beta} = K_{act,OC_a}^{TGF-\beta}$, the same activator function can be used in Eq. (3.1) and (3.3) and only the two parameters $R_{act}^{TGF-\beta}$ and $R_{rep}^{TGF-\beta}$ are needed to describe all the TGF-β related terms.

4.2 Revised regulatory functions related to PTH

As has already been pointed out in the previous chapter, one can easily check that the concentration of PTH, C_{PTH}, defined through Eq. (3.23) is constant. However, depending on the considered scenario it takes different values. In case of healthy bone there is no additional PTH production, *i.e.* $P_{PTH} = 0$, while in osteoporotic bone the parameter is set to $P_{PTH}^{PMO} = 5 \times 10^4$ pM/day.

The related Hill-typed regulatory functions given in Eqs. (3.21) and (3.22) are also constant, but dependent on C_{PTH}, and therefore they differ as well between the healthy and the osteoporotic case:

$$\pi_{act,OB_p}^{PTH} = \begin{cases} 1.9011 \times 10^{-2} & \text{if bone is healthy} \\ 7.9572 \times 10^{-1} & \text{if bone is osteoporotic} \end{cases}, \tag{4.5}$$

and

$$\pi_{rep,OB}^{PTH} = \begin{cases} 7.1124 \times 10^{-2} & \text{if bone is healthy} \\ 3.8078 \times 10^{-4} & \text{if bone is osteoporotic} \end{cases}. \tag{4.6}$$

4.3 Revised regulatory functions related to the RANK/RANKL/OPG-system

As can be seen in Eq. (3.18), the maximum concentration of RANKL, C_{RANKL}^{max}, depends linearly on $N_{RANKL}^{OB_p}$, $\pi_{act,OB}^{PTH}$ and C_{OB_p}. Since the former two quantities are both constant, C_{RANKL}^{max} is proportional to the concentration C_{OB_p} of osteoblast precursor cells, which gives rise to the following simplification of Eq. (3.18) to

$$C_{RANKL}^{max} = R_{RANKL}^{max} C_{OB_p}. \tag{4.7}$$

Due to the dependence on $\pi^{PTH}_{act,OB}$ the new parameter R^{max}_{RANKL} takes again different values depending on the considered scenario:

$$R^{max}_{RANKL} = \begin{cases} 5.1396 \times 10^4 & \text{if bone is healthy} \\ 2.1512 \times 10^6 & \text{if bone is osteoporotic} \end{cases}. \tag{4.8}$$

Using (3.20), Eq. (3.19), which expresses the OPG concentration, C_{OPG}, can be rewritten as

$$C_{OPG} = \frac{1}{\frac{1}{C^{max}_{OPG}} + \frac{R^{max}_{OPG}}{C_{OB_a}}}, \tag{4.9}$$

where R^{max}_{OPG} is defined through

$$R^{max}_{OPG} = \frac{\tilde{D}_{OPG}}{p^{OPG}_{OB_a}\pi^{PTH}_{rep,OB}}, \tag{4.10}$$

which gives

$$R^{max}_{OPG} = \begin{cases} 3.0285 \times 10^{-8} & \text{if bone is healthy} \\ 5.6568 \times 10^{-6} & \text{if bone is osteoporotic} \end{cases}. \tag{4.11}$$

The different values for the healthy and the osteoporotic scenario arise again from the dependence of R^{max}_{OPG} on $\pi^{PTH}_{rep,OB}$.

The equation for the RANKL concentration, C_{RANKL}, that was given in (3.17) can be modified to

$$C_{RANKL} = \frac{C^{max}_{RANKL}\frac{1+\hat{P}_{RANKL}}{1+R_{RANKL}C^{max}_{RANKL}}}{1 + K_{a,[RANKL-OPG]}C_{OPG} + K_{a,[RANKL-RANK]}C_{RANK}}, \tag{4.12}$$

with R_{RANKL} denoting the quotient

$$R_{RANKL} = \frac{\tilde{D}_{RANKL}}{\beta_{RANKL}} = 6.0163 \times 10^{-2} \ \ pM^{-1}. \tag{4.13}$$

Note that also the external RANKL dosage term, P_{RANKL}, has to be normalized with respect to the systemic production rate, thus

$$\hat{P}_{RANKL}(\Psi_{bm}) = \frac{P_{RANKL}(\Psi_{bm})}{\beta_{RANKL}}. \tag{4.14}$$

The remaining model equations stay unaltered, but for the sake of completeness they are given by

$$\pi^{RANKL}_{act,OC_p} = \frac{C_{[RANKL-RANK]}}{K^{RANKL-RANK}_{act,OCp} + C_{[RANKL-RANK]}}, \tag{4.15}$$

$$C_{[RANKL-RANK]} = K_{a,[RANKL-RANK]}C_{RANKL}C_{RANK}, \tag{4.16}$$

and

$$C_{RANK} = 10^4 \cdot C_{OC_p}. \tag{4.17}$$

Figure 4.1 contains all the equations of the revised bone cell population model and clearly illustrates its structure. The Matlab code that is used for all further calculations within this thesis is given in Appendix B.

Table 4.1 summarizes the parameters of the revised bone remodeling model, together with their values and units. It can be seen that the number of parameters has considerably reduced from 26 to 17 parameters, which already decreases the required computational effort needed for sensitivity and stability analyses drastically. However, the system is still very complex and the following chapter is devoted to revealing the relevance and the impact of the new set of model parameters.

Table 4.1: Parameters of the revised cell population model, their values and units.

Parameter	Numerical value		Unit
	healthy bone	osteoporotic bone	
$\mathcal{A}_{OB_a}$	$2.1107 \cdot 10^{-1}$		pM/day
$\mathcal{A}_{OC_a}$	5.6487		pM/day
$\mathcal{D}_{OB_u}$	$6.3 \cdot 10^{-2}$		pM/day
$\mathcal{D}_{OB_p}$	$1.657 \cdot 10^{-1}$		pM/day
$\mathcal{D}_{OC_p}$	2.1		pM/day
C_{OPG}^{max}	$2 \cdot 10^8$		pM
k_{res}	2		$(\text{pM day})^{-1}$
$K_{a,[RANKL-RANK]}$	$3.4117 \cdot 10^{-2}$		pM^{-1}
$K_{a,[RANKL-OPG]}$	$1 \cdot 10^{-3}$		pM^{-1}
$R_{act}^{TGF-\beta}$	$5.6328 \cdot 10^{-4}$		pM
$R_{rep}^{TGF-\beta}$	$1.7543 \cdot 10^{-4}$		pM
R_{RANKL}^{max}	$5.1396 \cdot 10^4$	$2.1512 \cdot 10^6$	-
R_{OPG}^{max}	$3.0285 \cdot 10^{-8}$	$5.6568 \cdot 10^{-6}$	-
R_{RANKL}	$6.0163 \cdot 10^{-2}$		pM^{-1}
$\mathcal{P}_{OB_p}$	$2.1107 \cdot 10^{-2}$		1/day
$K_{act,OC_p}^{RANK-RANKL}$	5.6797		pM
k_{form}	$4 \cdot 10^{-1}$		$(\text{pM day})^{-1}$

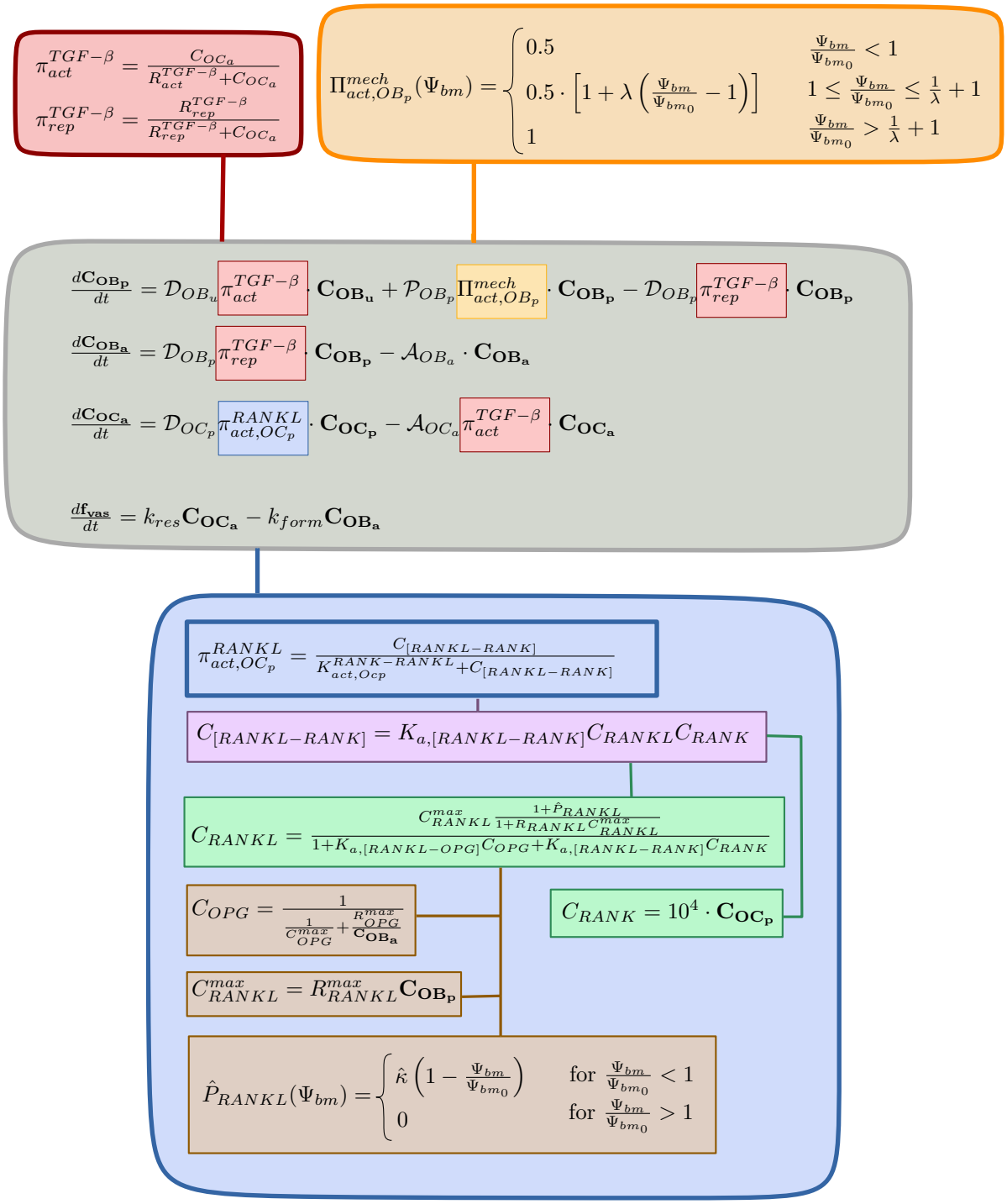

Figure 4.1: Flow chart of the equations of the revised bone remodeling model.

Chapter 5

Sensitivity analyses

There are many different approaches for performing a sensitivity analysis of a mathematical model. Biological systems (such as the one dealt with in this thesis) often comprise highly complex interrelations between several interacting factors, making it difficult to fully understand the influences between these parameters as well as their impact on the whole system. In order to better understand the influences of single parameters or combinations of parameters on the eventually obtained model predictions, sensitivity analyses were carried out.

5.1 Fundamental aspects and definition of analysis modalities

Generally speaking, sensitivity analyses are often based on the following principle:

1. Definition of reasonable ranges of the parameters of interest.

2. Identification of the model output according to which the sensitivity is assessed; it should allow for good comparability between the studied parameters.

3. Running the model numerous times, using some design of experiment-strategy (Sacks et al., 1989), depending on the input variability that has been identified in the first step.

4. Calculation of the chosen sensitivity measures.

In the following, these steps are briefly discussed, after which the results of the sensitivity studies are presented.

5.1.1 Definition of parameter ranges

The uncertainty related to the input variables of a complex model in general, and of the BCPM of bone remodeling studied here in particular may stem from two sources. On the one hand, parameters may be characterized by an inherent randomness. E.g., in bone remodeling there is a non-measurable and non-predictable variability from person to person. On the other hand, the certainty of parameters may be compromised by the fact that they are not known per se. E.g., in the bone remodeling model the resorption rate k_{res} of active osteoblasts is a (phenomenological but) well-defined parameter that in fact has a certain value (that may vary from person to person), but yet one lacks the capability of measuring this quantity. Biological models often involve parameters subjected to both types of uncertainties.

In the present case, parameter ranges are determined in the simplest possible way, leaving probability considerations (O'Hagan et al., 2006) aside, namely by simply varying each of the studied parameters by $\pm 90\,\%$. In particular, the following parameters are considered:

- apoptosis rate of active osteoblasts, $\mathcal{A}_{OBa}$
- apoptosis rate of active osteoclasts, $\mathcal{A}_{OCa}$
- differentiation rate of uncommited osteoblast precursors, $\mathcal{D}_{OBu}$
- differentiation rate of osteoblast precursors, $\mathcal{D}_{OBp}$
- differentiation rate of osteoclast precursors, $\mathcal{D}_{OCp}$
- maximum concentration of OPG, C_{OPG}^{max}
- bone resorption rate, k_{res}
- equilibrium association constant related to binding of RANKL to RANK, $K_{a,[RANKL-RANK]}$
- equilibrium association constant related to binding of OPF to RANKL, $K_{a,[RANKL-OPG]}$
- equilibrium constant related to binding of TGF-β to its respective receptors, $R_{act}^{TGF-\beta}$
- equilibrium constant related to binding of TGF-β to its respective receptors, $R_{rep}^{TGF-\beta}$
- maximum RANKL concentration coefficient, R_{RANKL}^{max}

- OPG degradation/production quotient, R_{OPG}^{max}
- RANKL degradation/production quotient, R_{RANKL}
- maximum proliferation rate, $\mathcal{P}_{OBp}$
- apparent dissociation equilibrium constant related to binding of RANKL to RANK, $K_{act,OCp}^{RANK-RANKL}$
- bone formation rate, k_{form}.

5.1.2 Identification of model output

Obviously, the bone remodeling model does respond to parameter variations by correspondingly changing single values representing the changed behavior of the modelled system, but by correspondingly changing time courses of several state variables. Hence, in order to nevertheless ensure good comparability and interpretability of the below presented and discussed sensitivity analyses, two simplifying assumptions are considered. Namely, it is assumed that the model behavior is sufficiently represented by the mean squared relative error (MSRE) between the time course of the original solution and the time course of the solution due to varied parameters, defined through

$$\text{MSRE}(Q,\ \text{parameter setting}) = \frac{1}{r}\sum_{i=0}^{r}\left(\frac{Q_{ref}(t_i) - Q_{var}(t_i)}{Q_{ref}(t_i)}\right)^2, \tag{5.1}$$

where $Q_{ref}(t_i)$ denotes the quantity of interest computed at time t_i with respect to the original parameter values given in Table 4.1, while $Q_{var}(t_i)$ denotes the respective quantity based on the varied parameter setting. Calculations within this thesis are carried out for a time period of $t = [0, 10000]$ days, with an equidistant distribution of points in time, with $r = 10000$.

The second significant assumption made in this work is that not all output quantities provided by the BCPM are considered, but only the most relevant one, which also features the best interpretability, *i.e.* the vascular porosity f_{vas}. Also, it should be noted that f_{vas} implicitly gathers the collected parameter sensitivities of the other relevant output variables (such as the cell concentrations C_{OBp}, C_{OBa}, and C_{OCa}, or the strain energy density Ψ_{bm} governing the considered mechanoregulatory mechanisms).

In order to exclude possible normalisation effects (which could be particularly relevant for very small values), a second objective function is optionally considered, namely the mean squared error (MSE), defined through

$$\text{MSE}(Q,\ \text{parameter setting}) = \frac{1}{r}\sum_{i=0}^{r}\left(Q_{ref}(t_i) - Q_{var}(t_i)\right)^2. \tag{5.2}$$

5.1.3 Considered load cases

Three specific load cases are considered for all subsequent sensitivity and other studies, including

- Load case I: The system is considered at steady state, without the effects of pathologies or mechanical scenarios deviating from "normal" loading. Hence, deviations from the steady-state solutions are only caused by parameter variations.

- Load case II: PMO is simulated, initiated through consideration of PMO-related PTH production, $P_{PTH,PMO} = 5 \cdot 10^4$ pM/day, from $t = 0$ onwards.

- Load case III: At $t = 0$, the mechanical loading is reduced from $\boldsymbol{\Sigma}_{\text{normal}} = [0, 0, 0; 0, 0, 0; 0, 0, -30]$ MPa to $\boldsymbol{\Sigma}_{\text{disuse}} = [0, 0, 0; 0, 0, 0; 0, 0, -25]$ MPa. At $t = 2000$ days, the loading is set back to $\boldsymbol{\Sigma}_{\text{normal}}$.

5.1.4 Analysis modes

The exact way of how parameters are varied in the course of a sensitivity analysis are usually referred to as design of experiments (Sacks et al., 1989; Pannell et al., 1997), see also Figure 5.1 for a generic graphical illustration on this matter. In principle, the more parameters govern the model behavior the more complex the corresponding sensitivity analysis. For the present BCPM, the most comprehensive way of performing the sensitivity analysis would be varying all 17 parameters at the same time. Considering then a small step size within the chosen parameter ranges would lead to a myriad of different parameter combinations, and in further consequence to a 17-dimensional solution space of the sensitivity measures. It goes without saying that the entailed CPU time would be excessively high and the interpretability of such results would be (while interesting) very limited. As a remedy, the model sensitivity to parameter variations is, in the first place, studied based on a very basic one-factor-at-a-time (OFAT) analysis. This means that only one parameter is varied while all other parameters are kept constant at the original value. Then, all possible combinations related to the simultaneous variations of a pair of two parameters are studied, in order to study interrelations between parameters. Furthermore, parameter triplets which are supposedly closely related to each other (from biological point of view) are varied simultaneously. Finally, all parameters are varied simultaneously in order to calculate suitable correlation measures.

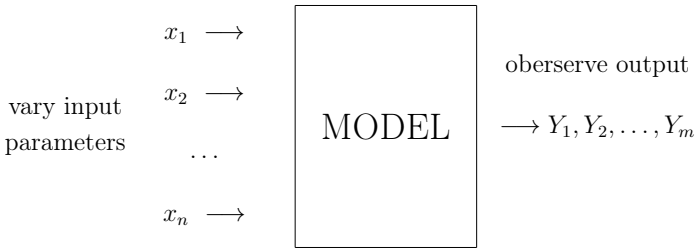

Figure 5.1: Schematic principle of sensitivity analysis.

5.2 One-dimensional (OFAT) sensitivity analyses

Within this thesis, parameter variations in the range of ±90% (with respect to the reference values given in Table 4.1) have been performed giving straightaway access to numerical values of parameters which yields physiologically meaningless results. In particular, a specific parameter value is considered to be meaningless if f_{vas} violates the condition $0 \leq f_{vas} \leq 0.9$. Table 5.1 summarizes the physiologically reasonable ranges in which the parameters can be varied, where the numbers represent the factors by which the original values (from Table 4.1) are multiplied. This procedure has been done for all three load cases introduced in Section 5.1.3. The intersection of the resulting reasonable parameter intervals for the individual load cases gives the overall interval, which is used subsequently for further calculations, see Table 5.1.

Figures 5.2 to 5.18 show the developments of the vascular porosity over time, which have been obtained by means of the OFAT studies for the three different scenarios. The variation step size chosen for this illustration was 0.05 and calculations were carried out for a total time span of 10000 days. The black graphs represent the results obtained for the original parameter values (from Table 4.1), the red lines present the results that are obtained by increasing the respective parameter compared to its reference value, while the blue ones show the results for decreased parameter values. The color intensity indicates how far the respective parameter is from its original value. It can be seen that the influence of the parameter C_{OPG}^{max}, which is varied in the range $[0.1, 1.9]$ according to Table 5.1, is very small for all three load cases, see Figure 5.7; especially increases of C_{OPG}^{max} seem to be virtually insignificant. Figure 5.8 shows that increasing k_{res} leads to an increased vascular porosity, which is not surprising considering that k_{res} determines the amount of bone that is resorbed by active osteoclasts. Thus, a decrease of k_{res} yields a reduced vascular porosity, and clearly for k_{form} the exact opposite behavior can be observed, see Figure 5.18. Note that for both, k_{res} and k_{form}, the range of physiologically reasonable resorption/formation rates is quite narrow – increasing k_{res} by a factor larger than 1.1, or decreasing k_{form} by more than

Table 5.1: Parameter intervals which yield, in the framework of the OFAT method, physiologically reasonable model predictions, for all three load cases separately (L I,II,III), as well as overall.

Parameter	L I	L II	L III	Overall
$\mathcal{A}_{OB_a}$	[0.8, 1.7]	[0.7, 1.1]	[0.8, 1.55]	[0.8, 1.1]
$\mathcal{A}_{OC_a}$	[0.1, 1.9]	[0.1, 1.9]	[0.1, 1.9]	[0.1, 1.9]
$\mathcal{D}_{OB_u}$	[0.6, 1.25]	[0.9, 1.45]	[0.65, 1.25]	[0.9, 1.25]
$\mathcal{D}_{OB_p}$	[0.55, 1.9]	[0.55, 1.25]	[0.55, 1.9]	[0.55, 1.25]
$\mathcal{D}_{OC_p}$	[0.1, 1.9]	[0.1, 1.9]	[0.1, 1.9]	[0.1, 1.9]
C_{OPG}^{max}	[0.1, 1.9]	[0.1, 1.9]	[0.1, 1.9]	[0.1, 1.9]
k_{res}	[0.8, 1.5]	[0.7, 1.1]	[0.8, 1.45]	[0.8, 1.1]
$K_{a,[RANKL-RANK]}$	[0.1, 1.9]	[0.1, 1.9]	[0.1, 1.9]	[0.1, 1.9]
$K_{a,[RANKL-OPG]}$	[0.1, 1.9]	[0.1, 1.9]	[0.1, 1.9]	[0.1, 1.9]
$R_{act}^{TGF-\beta}$	[0.7, 1.7]	[0.45, 1.2]	[0.7, 1.6]	[0.7, 1.2]
$R_{rep}^{TGF-\beta}$	[0.45, 1.9]	[0.5, 1.5]	[0.5, 1.9]	[0.5,1.5]
R_{RANKL}^{max}	[0.1, 1.9]	[0.1, 1.9]	[0.1, 1.9]	[0.1, 1.9]
R_{OPG}^{max}	[0.1, 1.9]	[0.1, 1.9]	[0.1, 1.9]	[0.1, 1.9]
R_{RANKL}	[0.1, 1.9]	[0.1, 1.9]	[0.1, 1.9]	[0.1, 1.9]
$\mathcal{P}_{OB_p}$	[0.1, 1.8]	[0.8, 1.8]	[0.1, 1.8]	[0.8, 1.8]
$K_{act,OC_p}^{RANK-RANKL}$	[0.1, 1.9]	[0.1, 1.9]	[0.1, 1.9]	[0.1, 1.9]
k_{form}	[0.55, 1.25]	[0.9, 1.45]	[0.6, 1.25]	[0.9, 1.25]

10%, induces a vascular porosity that is larger than 0.9, while multiplying k_{res} by a factor smaller than 0.9, or k_{form} by a factor larger than 1.25, yields a negative vascular porosity.

Furthermore, Figures 5.12 and 5.16 show that for load case III the model reacts more sensitively to changes of the parameter $R_{rep}^{TGF-\beta}$ and $\mathcal{P}_{OBp}$, as compared to the other load cases. However, for changes of other parameters such as $K_{a,[RANKL-RANK]}$ (Figure 5.9) and R_{RANKL}^{max} (Figure 5.13) the maximal errors are obtained in load case I.

In order to improve the perceptibility of the parameter sensitivity, Figures 5.19 to 5.35 show the relative errors $RE(f_{vas})$ of the model-predicted vascular porosities over time for all 17 parameters and all 3 load cases, defined as

$$RE(f_{vas},\ \text{parameter setting}) = \frac{f_{vas,var} - f_{vas,ref}}{f_{vas,ref}}, \tag{5.3}$$

where $f_{vas,ref}$ denotes the vascular porosity obtained with the original parameter values (from Table 4.1) and $f_{vas,var}$ is the vascular porosity for modified parameter settings. To ensure an improved comparability between the figures corresponding

to different parameter variations, while at the same time capturing the information obtained by the OFAT-method, the y-axes in Figures 5.19 to 5.35 were chosen to either reach a value of 0.75 or 3 for all parameters. This way of presenting the results confirms the aforementioned predication that C_{OPG}^{max} has very little influence on the BCPM, see Figure 5.24. Furthermore, the comparability between the considered load cases is much improved. While the BCPM responds with approximately the same sensitivity in all load cases for variations of $\mathcal{D}_{OBp}$ (see Figure 5.22), this is not the case for variations of $K_{a,[RANKL-RANK]}$, $K_{a,[RANKL-OPG]}$, or R_{OPG}^{max} where the relative error in load case I is visibly larger compared to the other load cases, see Figures 5.26, 5.27 and 5.31. In load case II, there are several cases where a variation of the parameter leads initially to higher relative errors, which tend to zero in the long run, see Figures 5.20, 5.23, 5.26, 5.27, 5.31, 5.32 and 5.34 (b). This phenomenon cannot be observed for the other two load cases. For load case I the relative errors are strictly increasing over time, while for load case III the BCPM seems to be very sensitive to variations of the parameters in the beginning, then the relative errors decrease rapidly, followed by a steady increase over time.

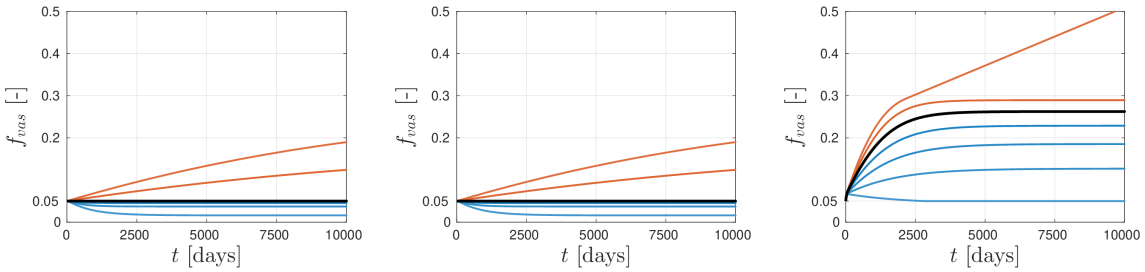

(a) L I, $\mathcal{A}_{OBa}$ (b) L II, $\mathcal{A}_{OBa}$ (c) L III, $\mathcal{A}_{OBa}$

Figure 5.2: Model-predicted vascular porosities over time, when applying the OFAT-method for the parameter $\mathcal{A}_{OBa}$ and all three load cases.

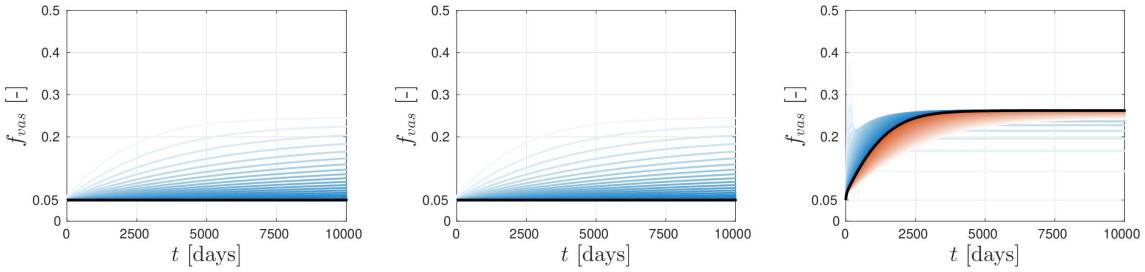

(a) L I, $\mathcal{A}_{OCa}$ (b) L II, $\mathcal{A}_{OCa}$ (c) L III, $\mathcal{A}_{OCa}$

Figure 5.3: Model-predicted vascular porosities over time, when applying the OFAT-method for the parameter $\mathcal{A}_{OCa}$ and all three load cases.

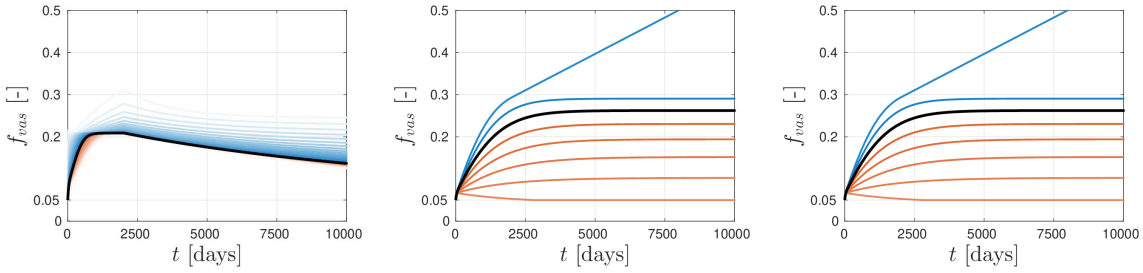

(a) L I, $\mathcal{D}_{OBu}$ (b) L II, $\mathcal{D}_{OBu}$ (c) L III, $\mathcal{D}_{OBu}$

Figure 5.4: Model-predicted vascular porosities over time, when applying the OFAT-method for the parameter $\mathcal{D}_{OBu}$ and all three load cases.

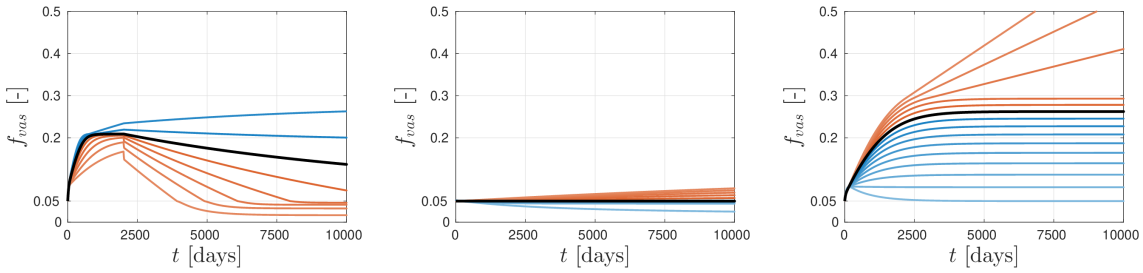

(a) L I, $\mathcal{D}_{OBp}$ (b) L II, $\mathcal{D}_{OBp}$ (c) L III, $\mathcal{D}_{OBp}$

Figure 5.5: Model-predicted vascular porosities over time, when applying the OFAT-method for the parameter $\mathcal{D}_{OBp}$ and all three load cases.

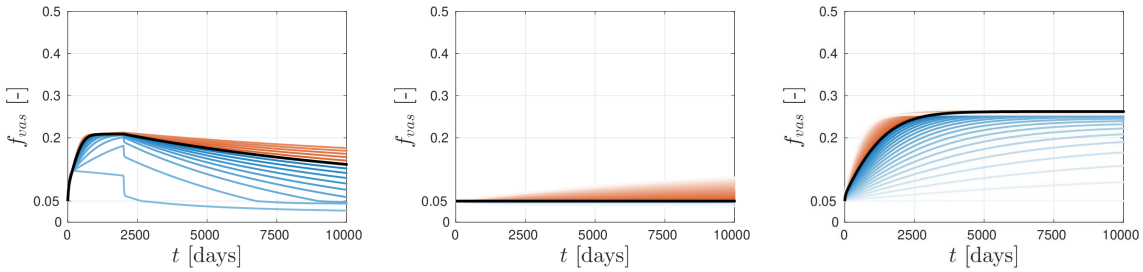

(a) L I, $\mathcal{D}_{OCp}$ (b) L II, $\mathcal{D}_{OCp}$ (c) L III, $\mathcal{D}_{OCp}$

Figure 5.6: Model-predicted vascular porosities over time, when applying the OFAT-method for the parameter $\mathcal{D}_{OCp}$ and all three load cases.

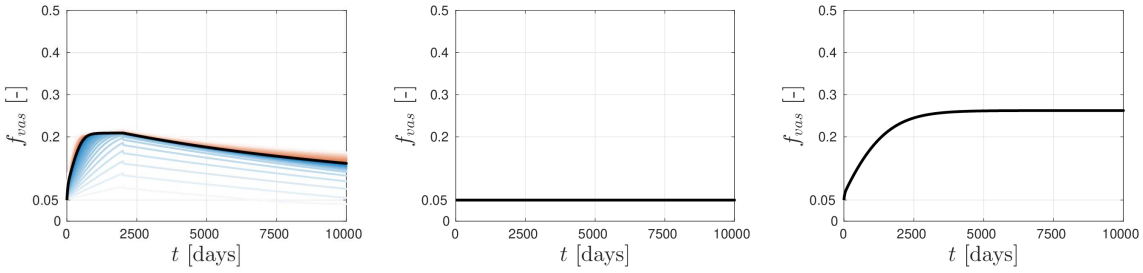

(a) L I, C_{OPG}^{max} (b) L II, C_{OPG}^{max} (c) L III, C_{OPG}^{max}

Figure 5.7: Model-predicted vascular porosities over time, when applying the OFAT-method for the parameter C_{OPG}^{max} and all three load cases.

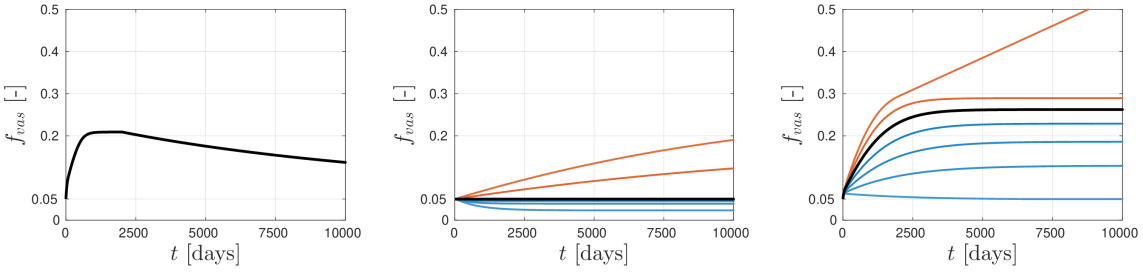

(a) L I, k_{res} (b) L II, k_{res} (c) L III, k_{res}

Figure 5.8: Model-predicted vascular porosities over time, when applying the OFAT-method for the parameter k_{res} and all three load cases.

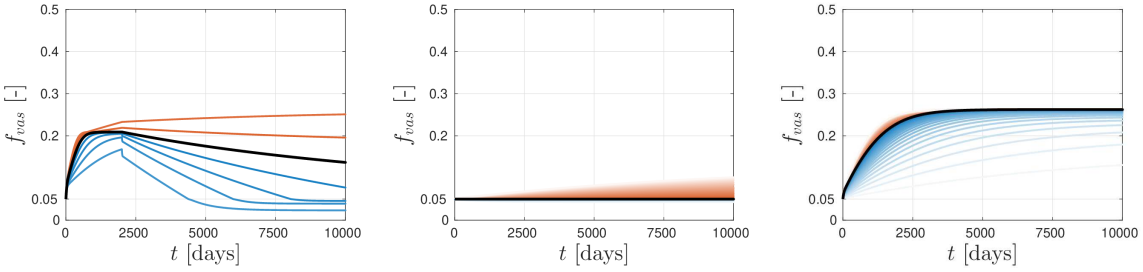

(a) L I, $K_{a,[RANKL-RANK]}$ (b) L II, $K_{a,[RANKL-RANK]}$ (c) L III, $K_{a,[RANKL-RANK]}$

Figure 5.9: Model-predicted vascular porosities over time, when applying the OFAT-method for the parameter $K_{a,[RANKL-RANK]}$ and all three load cases.

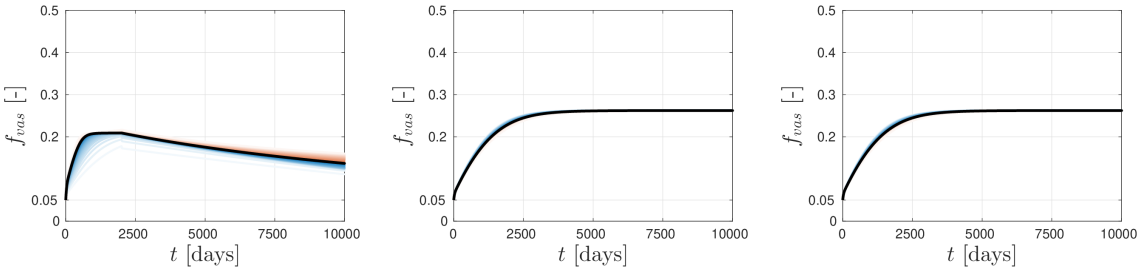

(a) L I, $K_{a,[RANKL-OPG]}$ (b) L II, $K_{a,[RANKL-OPG]}$ (c) L III, $K_{a,[RANKL-OPG]}$

Figure 5.10: Model-predicted vascular porosities over time, when applying the OFAT-method for the parameter $K_{a,[RANKL-OPG]}$ and all three load cases.

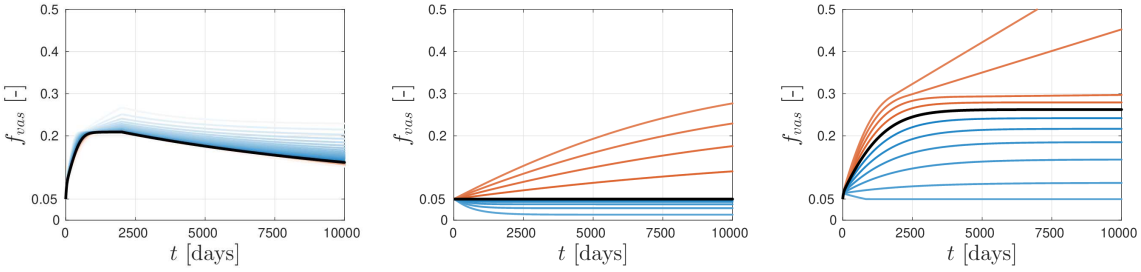

(a) L I, $R_{act}^{TGF-\beta}$ (b) L II, $R_{act}^{TGF-\beta}$ (c) L III, $R_{act}^{TGF-\beta}$

Figure 5.11: Model-predicted vascular porosities over time, when applying the OFAT-method for the parameter $R_{act}^{TGF-\beta}$ and all three load cases.

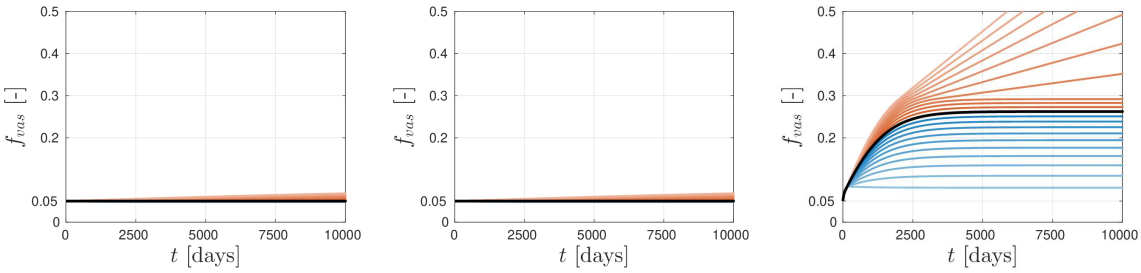

(a) L I, $R_{rep}^{TGF-\beta}$ (b) L II, $R_{rep}^{TGF-\beta}$ (c) L III, $R_{rep}^{TGF-\beta}$

Figure 5.12: Model-predicted vascular porosities over time, when applying the OFAT-method for the parameter $R_{rep}^{TGF-\beta}$ and all three load cases.

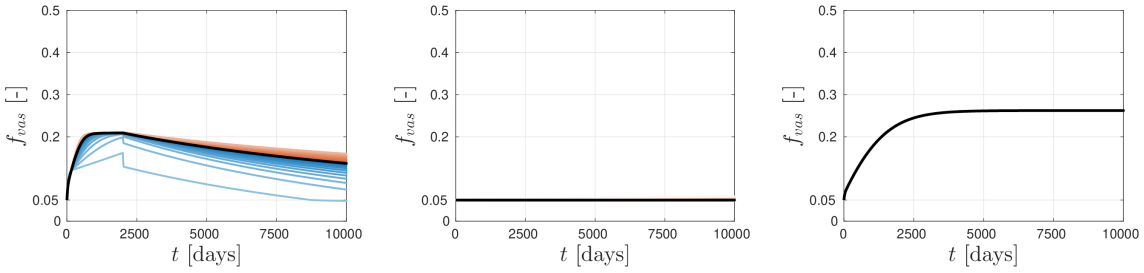

(a) L I, R^{max}_{RANKL} (b) L II, R^{max}_{RANKL} (c) L III, R^{max}_{RANKL}

Figure 5.13: Model-predicted vascular porosities over time, when applying the OFAT-method for the parameter R^{max}_{RANKL} and all three load cases.

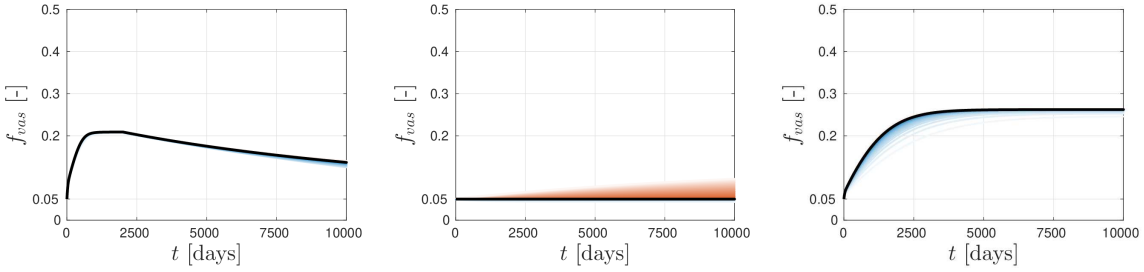

(a) L I, R^{max}_{OPG} (b) L II, R^{max}_{OPG} (c) L III, R^{max}_{OPG}

Figure 5.14: Model-predicted vascular porosities over time, when applying the OFAT-method for the parameter R^{max}_{OPG} and all three load cases.

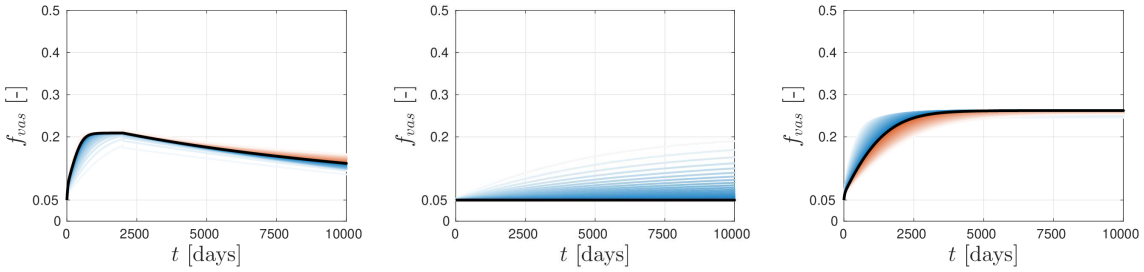

(a) L I, R_{RANKL} (b) L II, R_{RANKL} (c) L III, R_{RANKL}

Figure 5.15: Model-predicted vascular porosities over time, when applying the OFAT-method for the parameter R_{RANKL} and all three load cases.

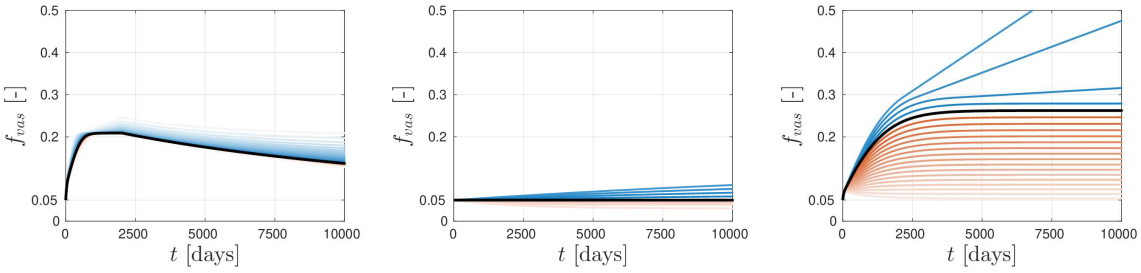

(a) L I, $\mathcal{P}_{OBp}$ (b) L II, $\mathcal{P}_{OBp}$ (c) L III, $\mathcal{P}_{OBp}$

Figure 5.16: Model-predicted vascular porosities over time, when applying the OFAT-method for the parameter $\mathcal{P}_{OBp}$ and all three load cases.

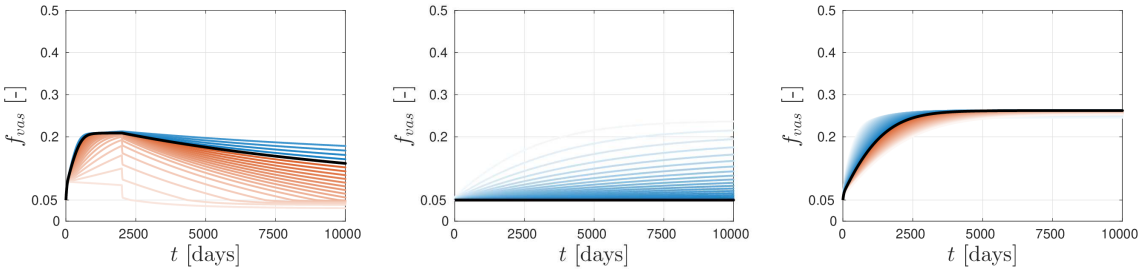

(a) L I, $K_{act,OCp}^{[RANKL-RANK]}$ (b) L II, $K_{act,OCp}^{[RANKL-RANK]}$ (c) L III, $K_{act,OCp}^{[RANKL-RANK]}$

Figure 5.17: Model-predicted vascular porosities over time, when applying the OFAT-method for the parameter $K_{act,OCp}^{[RANKL-RANK]}$ and all three load cases.

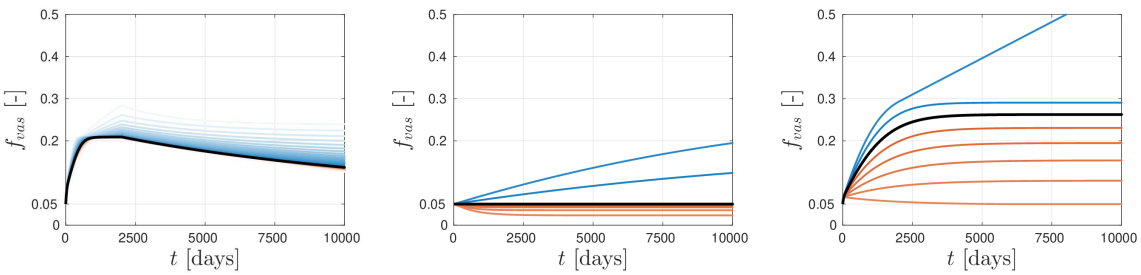

(a) L I, k_{form} (b) L II, k_{form} (c) L III, k_{form}

Figure 5.18: Model-predicted vascular porosities over time, when applying the OFAT-method for the parameter k_{form} and all three load cases.

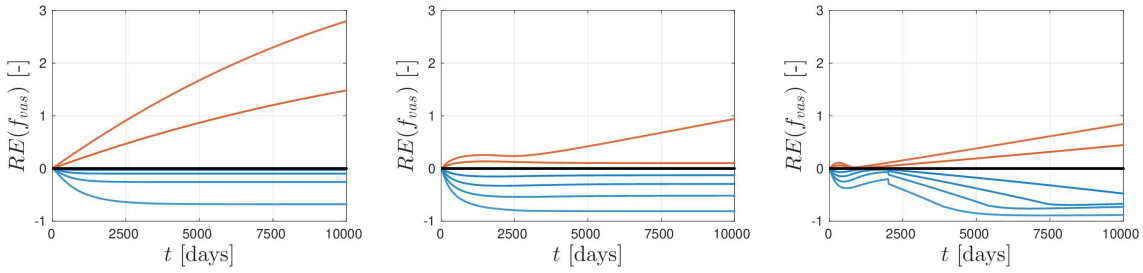

(a) L I, $\mathcal{A}_{OBa}$ (b) L II, $\mathcal{A}_{OBa}$ (c) L III, $\mathcal{A}_{OBa}$

Figure 5.19: Relative errors of model-predicted vascular porosities over time for the parameter $\mathcal{A}_{OBa}$ and all three load cases.

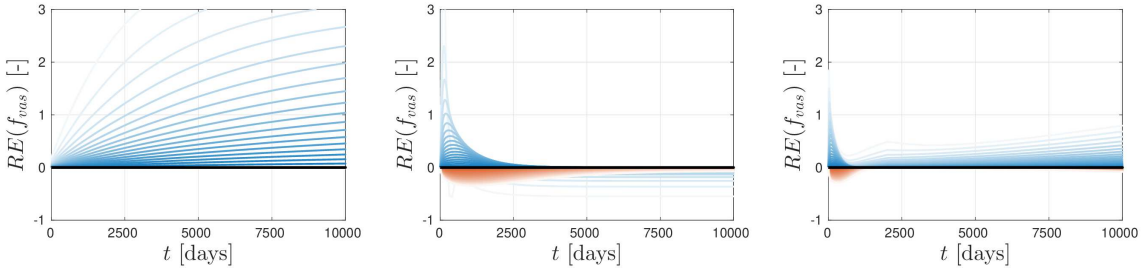

(a) L I, $\mathcal{A}_{OCa}$ (b) L II, $\mathcal{A}_{OCa}$ (c) L III, $\mathcal{A}_{OCa}$

Figure 5.20: Relative errors of model-predicted vascular porosities over time for the parameter $\mathcal{A}_{OCa}$ and all three load cases.

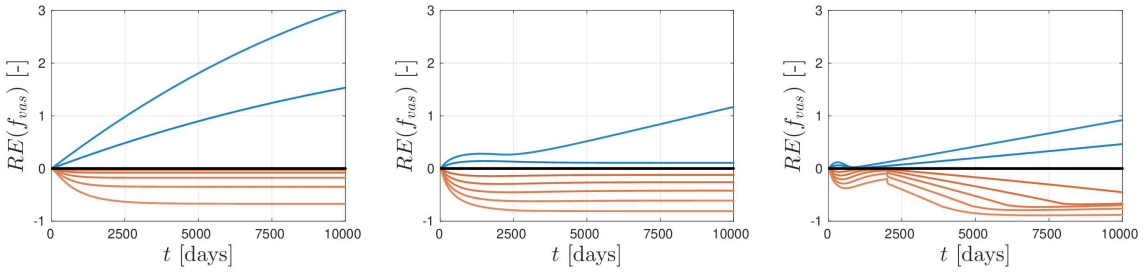

(a) L I, $\mathcal{D}_{OBu}$ (b) L II, $\mathcal{D}_{OBu}$ (c) L III, $\mathcal{D}_{OBu}$

Figure 5.21: Relative errors of model-predicted vascular porosities over time for the parameter $\mathcal{D}_{OBu}$ and all three load cases.

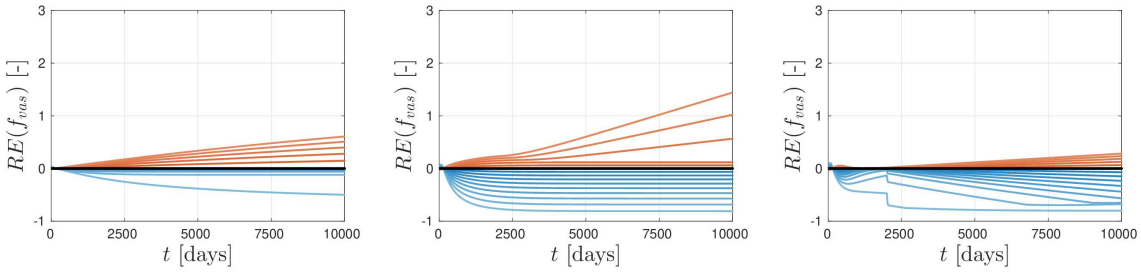

(a) L I, $\mathcal{D}_{OBp}$ (b) L II, $\mathcal{D}_{OBp}$ (c) L III, $\mathcal{D}_{OBp}$

Figure 5.22: Relative errors of model-predicted vascular porosities over time for the parameter $\mathcal{D}_{OBp}$ and all three load cases.

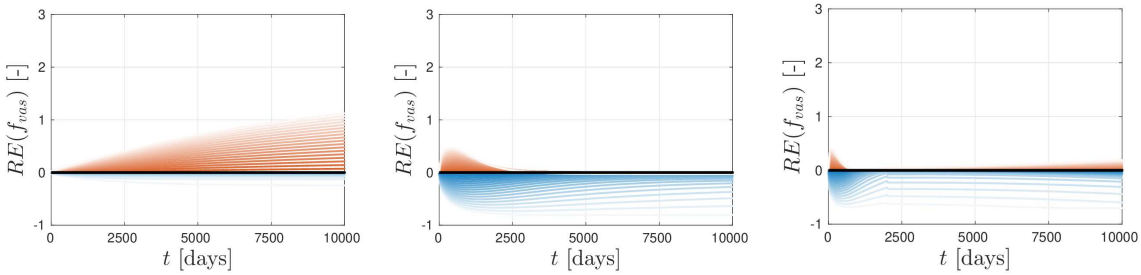

(a) L I, $\mathcal{D}_{OCp}$ (b) L II, $\mathcal{D}_{OCp}$ (c) L III, $\mathcal{D}_{OCp}$

Figure 5.23: Relative errors of model-predicted vascular porosities over time for the parameter $\mathcal{D}_{OCp}$ and all three load cases.

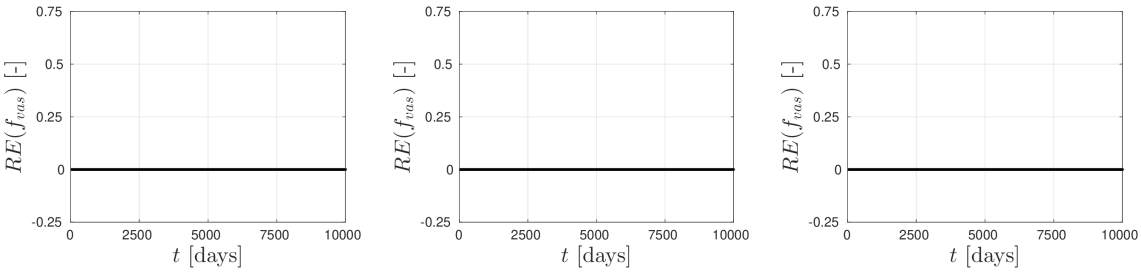

(a) L I, C_{OPG}^{max} (b) L II, C_{OPG}^{max} (c) L III, C_{OPG}^{max}

Figure 5.24: Relative errors of model-predicted vascular porosities over time for the parameter C_{OPG}^{max} and all three load cases.

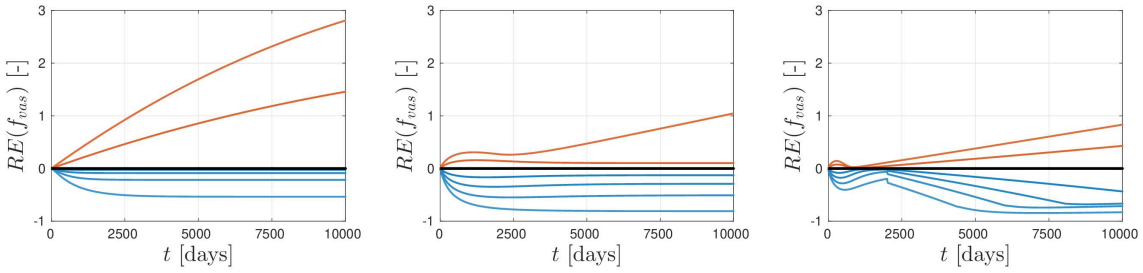

(a) L I, k_{res} (b) L II, k_{res} (c) L III, k_{res}

Figure 5.25: Relative errors of model-predicted vascular porosities over time for the parameter k_{res} and all three load cases.

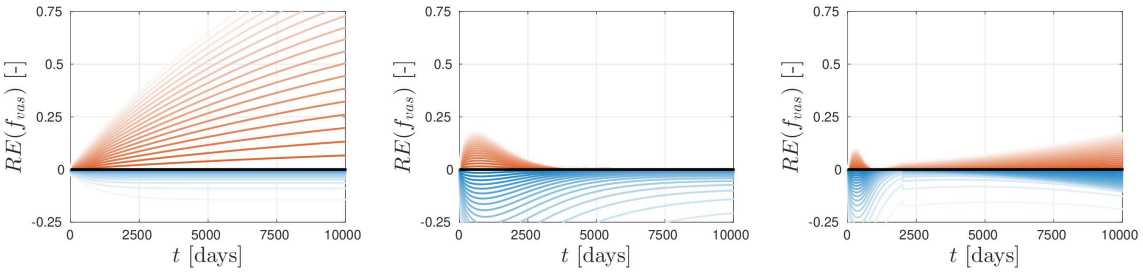

(a) L I, $K_{a,[RANKL-RANK]}$ (b) L II, $K_{a,[RANKL-RANK]}$ (c) L III, $K_{a,[RANKL-RANK]}$

Figure 5.26: Relative errors of model-predicted vascular porosities over time for the parameter $K_{a,[RANKL-RANK]}$ and all three load cases.

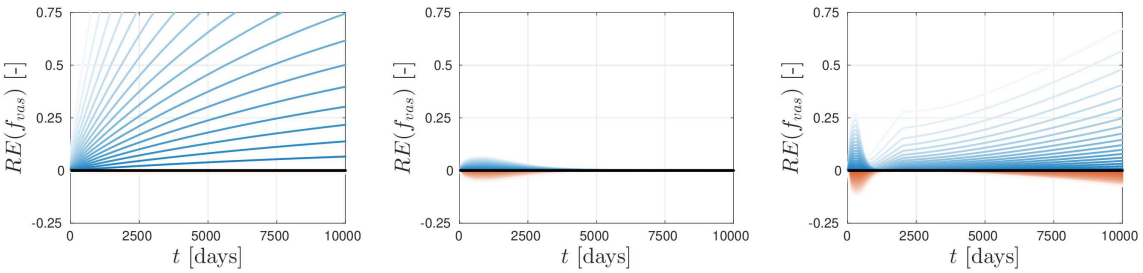

(a) L I, $K_{a,[RANKL-OPG]}$ (b) L II, $K_{a,[RANKL-OPG]}$ (c) L III, $K_{a,[RANKL-OPG]}$

Figure 5.27: Relative errors of model-predicted vascular porosities over time for the parameter $K_{a,[RANKL-OPG]}$ and all three load cases.

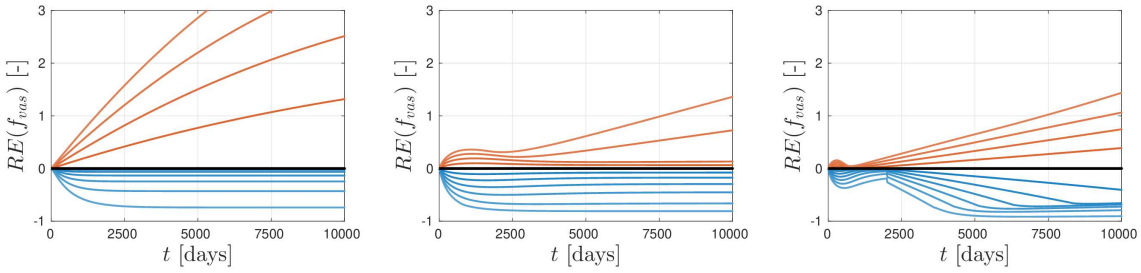

(a) L I, $R_{act}^{TGF-\beta}$ (b) L II, $R_{act}^{TGF-\beta}$ (c) L III, $R_{act}^{TGF-\beta}$

Figure 5.28: Relative errors of model-predicted vascular porosities over time for the parameter $R_{act}^{TGF-\beta}$ and all three load cases.

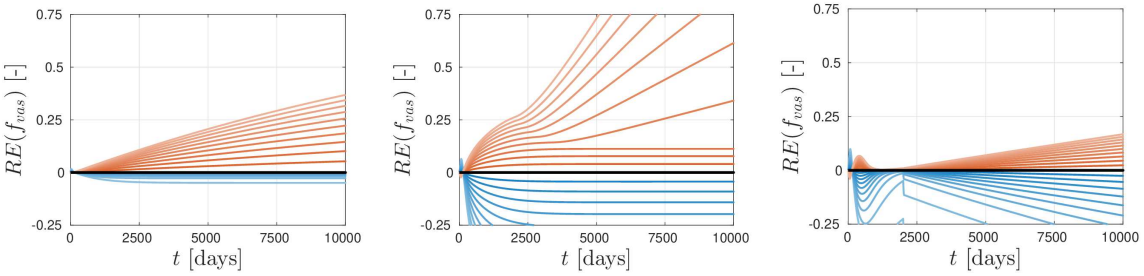

(a) L I, $R_{rep}^{TGF-\beta}$ (b) L II, $R_{rep}^{TGF-\beta}$ (c) L III, $R_{rep}^{TGF-\beta}$

Figure 5.29: Relative errors of model-predicted vascular porosities over time for the parameter $R_{rep}^{TGF-\beta}$ and all three load cases.

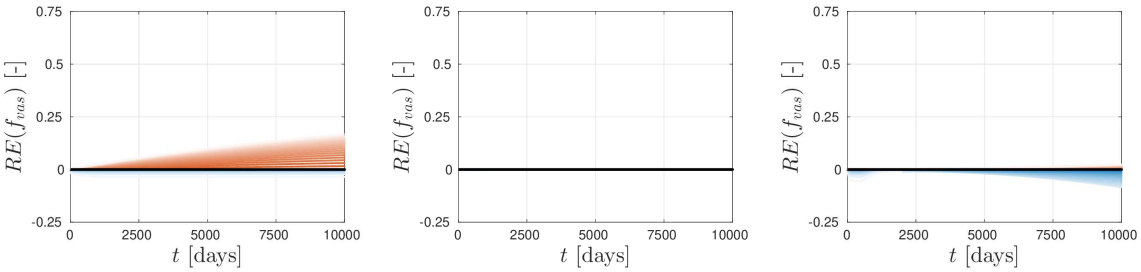

(a) L I, R_{RANKL}^{max} (b) L II, R_{RANKL}^{max} (c) L III, R_{RANKL}^{max}

Figure 5.30: Relative errors of model-predicted vascular porosities over time for the parameter R_{RANKL}^{max} and all three load cases.

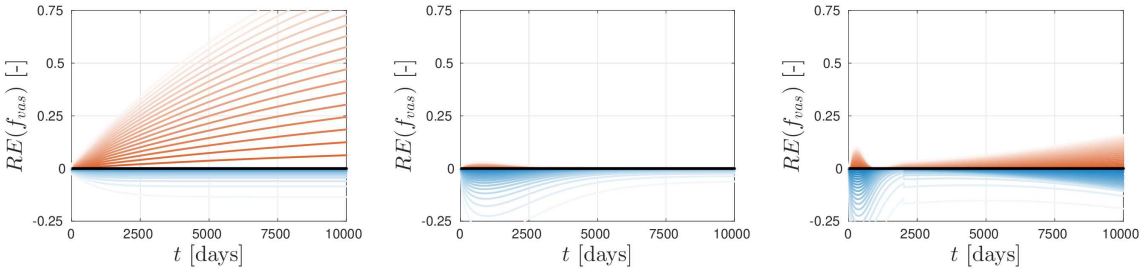

(a) L I, R^{max}_{OPG} (b) L II, R^{max}_{OPG} (c) L III, R^{max}_{OPG}

Figure 5.31: Relative errors of model-predicted vascular porosities over time for the parameter R^{max}_{OPG} and all three load cases.

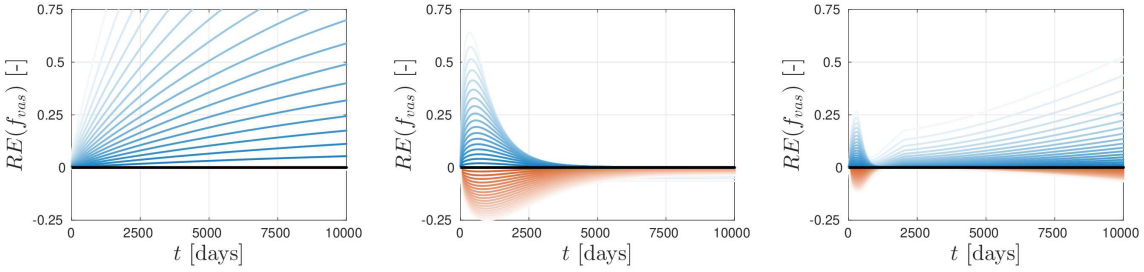

(a) L I, R_{RANKL} (b) L II, R_{RANKL} (c) L III, R_{RANKL}

Figure 5.32: Relative errors of model-predicted vascular porosities over time for the parameter R_{RANKL} and all three load cases.

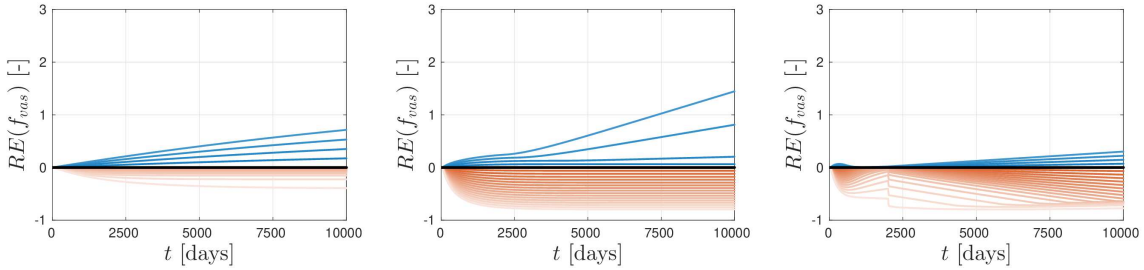

(a) L I, $\mathcal{P}_{OBp}$ (b) L II, $\mathcal{P}_{OBp}$ (c) L III, $\mathcal{P}_{OBp}$

Figure 5.33: Relative errors of model-predicted vascular porosities over time for the parameter $\mathcal{P}_{OBp}$ and all three load cases.

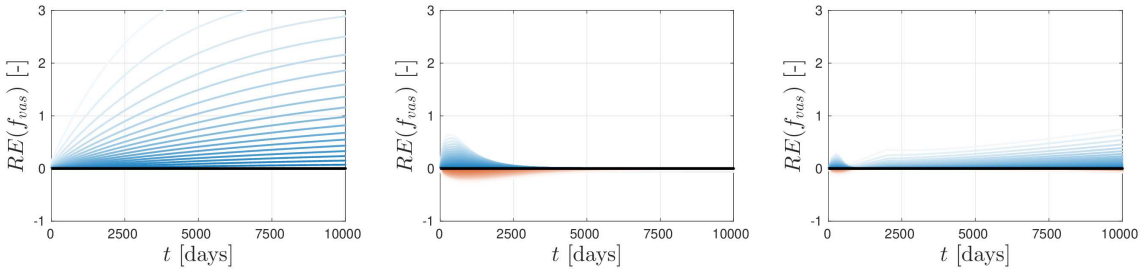

(a) L I, $K_{act,OCp}^{[RANKL-RANK]}$ (b) L II, $K_{act,OCp}^{[RANKL-RANK]}$ (c) L III, $K_{act,OCp}^{[RANKL-RANK]}$

Figure 5.34: Relative errors of model-predicted vascular porosities over time for the parameter $K_{act,OCp}^{[RANKL-RANK]}$ and all three load cases.

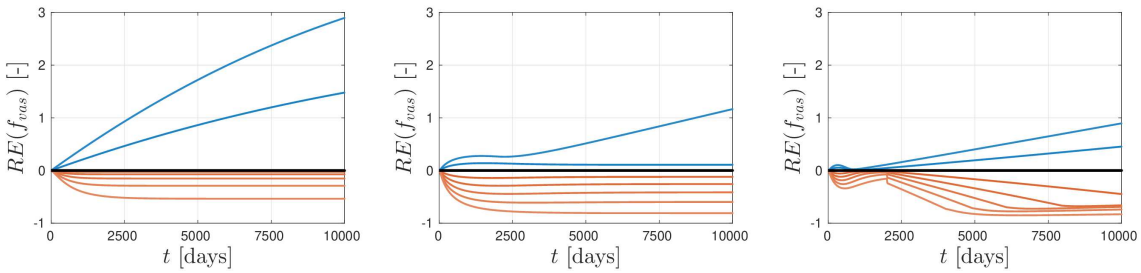

(a) L I, k_{form} (b) L II, k_{form} (c) L III, k_{form}

Figure 5.35: Relative errors of model-predicted vascular porosities over time for the parameter k_{form} and all three load cases.

Finally, the objective functions MSRE and MSE were computed for all parameter variations, according to Eqs. (5.1) and (5.2). Figure 5.36 shows the respective results for all load cases, which confirm the conclusions gained from interpreting Figures 5.2 to 5.18 and 5.19 to 5.35.

The computations presented so far have all been carried out for $f_{vas,ini} = 0.05$. However, all simulations were repeated with $f_{vas,ini} = 0.25$ (in order to consider endocortical bone which exhibits a higher porosity). The responses of the BCPM are qualitatively the same, although the BCPM sensitivity seems to be less pronounced for load case I and III when increasing $f_{vas,ini}$. For the sake of conciseness, Figure 5.37 solely shows the results for one examplary parameter, while the results for all parameters are given in the appendix in Figure A.1 to A.34.

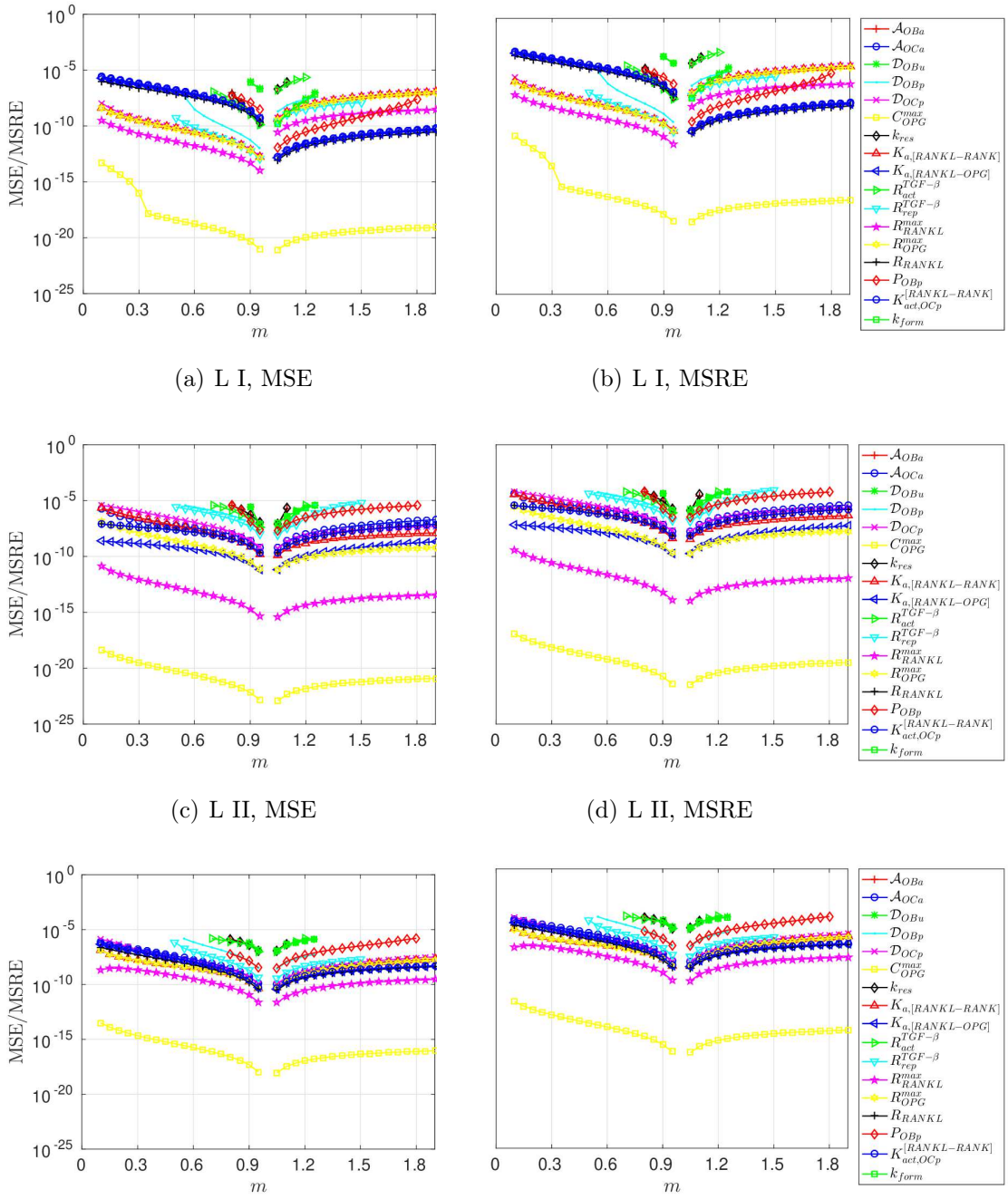

(a) L I, MSE (b) L I, MSRE

(c) L II, MSE (d) L II, MSRE

(e) L III, MSE (f) L III, MSRE

Figure 5.36: MSE ans MSRE according to Eqs. (5.1) and (5.2) over the factor m by which the respective parameter is varied for all three load cases.

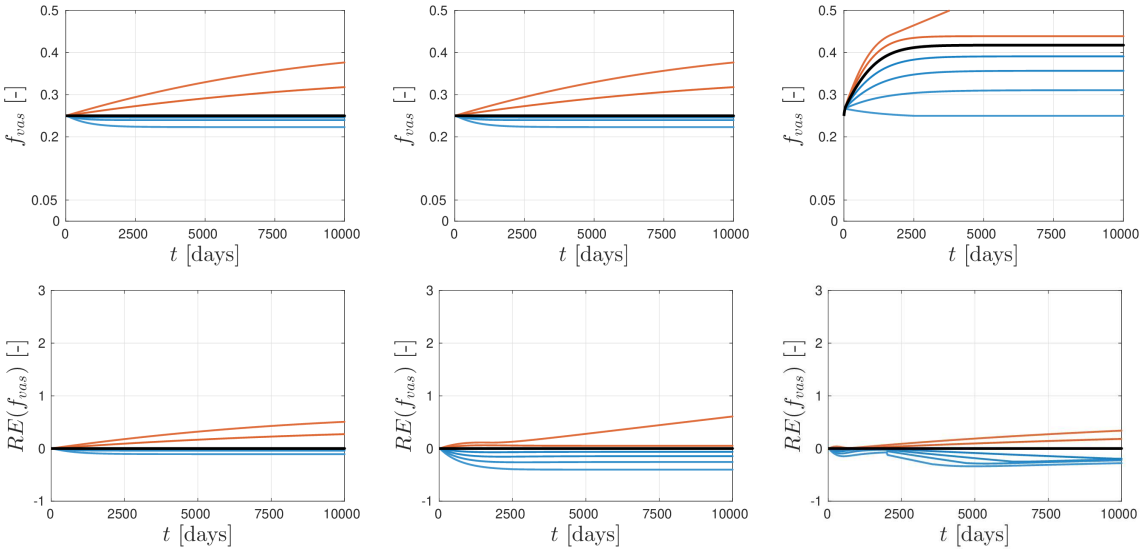

Figure 5.37: Model-predicted vascular porosities f_{vas}, as well as relative errors $RE(f_{vas})$, for variations of the parameter $\mathcal{A}_{OBa}$, for all three load cases and $f_{vas,ini} = 0.25$.

5.2.1 Direct comparison of model output

Based on the OFAT-results one can calculate the error between the curves obtained for the vascular porosity over time between each two parameters. Tables 5.2 to 5.4 summarize these errors averaged over the set of curves obtained from varying the two respective parameters by factors $m \in [0.1, 1.9]$ with a step size of 0.05, *i.e.* m takes 37 different values. Thus, the errors $E(p_1, p_2)$ are calculated as

$$E(p_1, p_2) = \frac{1}{37} \sum_{i=1}^{37} \frac{1}{10000} \sum_{j=1}^{10000} (f_{vas,p_1,m_i}(t_j) - f_{vas,p_2,m_i}(t_j)), \tag{5.4}$$

where p_1 and p_2 denote the respective two parameters and $f_{vas,p,m_i}(t_j)$ denotes the vascular porosity at time t_j when the parameter p is changed by a factor m_i.

When comparing Tables 5.2 to 5.4 one can see that the values in Table 5.2 that are obtained for load case I are much smaller than those for the other load cases, where the errors for load case II are particularly large. Overall, the smallest errors are obtained when comparing the parameters $K_{act,OCp}^{RANK-RANKL}$ and $K_{a,[RANKL-OPG]}$, thereby indicating a possible proportional relation between the two respective parameters. Figure 5.38 shows the evolution of the vascular porosity over time for (individual) variations of the parameters $K_{act,OCp}^{RANK-RANKL}$ and $K_{a,[RANKL-OPG]}$ in all three load cases. The graphs confirm the hypothesis that variations of these two parameters have basically the same influence on the models behavior.

Table 5.2: Direct comparison of the model output obtained by varying two distinct parameters based on the OFAT-method for load case I, calculated via Eq. (5.4). The matrix is in fact symmetric, *i.e.* the empty entries can be filled by flipping the upper half of the matrix over the diagonal; the entries of the diagonal are of course 0.

	$\mathcal{A}_{OCa}$	$\mathcal{D}_{OBu}$	$\mathcal{D}_{OBp}$	$\mathcal{D}_{OCp}$	C^{max}_{OPG}	k_{res}	$K_{a,[RANKL-RANK]}$	$K_{a,[RANKL-OPG]}$
$\mathcal{A}_{OBa}$	1.03e-06	2.46e-05	9.04e-07	9.11e-07	1.03e-06	2.10e-07	9.20e-07	1.03e-06
$\mathcal{A}_{OCa}$		1.55e-05	4.32e-09	3.89e-09	1.66e-12	2.18e-06	3.29e-09	3.50e-14
$\mathcal{D}_{OBu}$			1.61e-05	1.60e-05	1.56e-05	2.93e-05	1.60e-05	1.55e-05
$\mathcal{D}_{OBp}$				3.67e-11	4.17e-09	1.99e-06	9.25e-11	4.30e-09
$\mathcal{D}_{OCp}$					3.75e-09	2.00e-06	2.56e-11	3.87e-09
C^{max}_{OPG}						2.17e-06	3.15e-09	1.21e-12
k_{res}							2.01e-06	2.18e-06
$K_{a,[RANKL-RANK]}$								3.27e-09
$K_{a,[RANKL-OPG]}$								
$R^{TGF-\beta}_{act}$								
$R^{TGF-\beta}_{rep}$								
R^{max}_{RANKL}								
R^{max}_{OPG}								
R_{RANKL}								
$\mathcal{P}_{OBp}$								
$K^{RANK-RANKL}_{act,OCp}$								

	$R^{TGF-\beta}_{act}$	$R^{TGF-\beta}_{rep}$	R^{max}_{RANKL}	R^{max}_{OPG}	R_{RANKL}	$\mathcal{P}_{OBp}$	$K^{RANK-RANKL}_{act,OCp}$	k_{form}
$\mathcal{A}_{OBa}$	2.18e-10	9.78e-07	1.01e-06	9.28e-07	1.03e-06	1.52e-06	1.03e-06	2.52e-05
$\mathcal{A}_{OCa}$	1.06e-06	7.55e-10	9.93e-11	2.82e-09	1.50e-13	5.13e-08	9.63e-15	1.61e-05
$\mathcal{D}_{OBu}$	2.47e-05	1.58e-05	1.56e-05	1.60e-05	1.55e-05	1.39e-05	1.55e-05	4.13e-09
$\mathcal{D}_{OBp}$	9.31e-07	1.46e-09	3.11e-09	1.79e-10	4.27e-09	8.40e-08	4.31e-09	1.66e-05
$\mathcal{D}_{OCp}$	9.38e-07	1.22e-09	2.75e-09	8.63e-11	3.85e-09	8.15e-08	3.88e-09	1.66e-05
C^{max}_{OPG}	1.06e-06	6.93e-10	7.71e-11	2.70e-09	8.08e-13	5.17e-08	1.41e-12	1.61e-05
k_{res}	1.98e-07	2.10e-06	2.15e-06	2.02e-06	2.17e-06	2.87e-06	2.18e-06	3.00e-05
$K_{a,[RANKL-RANK]}$	9.48e-07	8.95e-10	2.24e-09	1.79e-11	3.25e-09	7.88e-08	3.28e-09	1.65e-05
$K_{a,[RANKL-OPG]}$	1.06e-06	7.46e-10	9.58e-11	2.80e-09	4.03e-14	5.13e-08	7.93e-15	1.61e-05
$R^{TGF-\beta}_{act}$		1.01e-06	1.04e-06	9.56e-07	1.06e-06	1.56e-06	1.06e-06	2.54e-05
$R^{TGF-\beta}_{rep}$			3.08e-10	6.59e-10	7.36e-10	6.38e-08	7.50e-10	1.63e-05
R^{max}_{RANKL}				1.86e-09	9.22e-11	5.56e-08	9.75e-11	1.61e-05
R^{max}_{OPG}					2.78e-09	7.65e-08	2.81e-09	1.65e-05
R_{RANKL}						5.14e-08	8.40e-14	1.61e-05
$\mathcal{P}_{OBp}$							5.13e-08	1.44e-05
$K^{RANK-RANKL}_{act,OCp}$								1.61e-05

Table 5.3: Direct comparison of the model output obtained by varying two distinct parameters based on the OFAT-method for load case II, calculated via Eq. (5.4). The matrix is in fact symmetric, *i.e.* the empty entries can be filled by flipping the upper half of the matrix over the diagonal; the entries of the diagonal are of course 0.

	$\mathcal{A}_{OCa}$	$\mathcal{D}_{OBu}$	$\mathcal{D}_{OBp}$	$\mathcal{D}_{OCp}$	C^{max}_{OPG}	k_{res}	$K_{a,[RANKL-RANK]}$	$K_{a,[RANKL-OPG]}$
$\mathcal{A}_{OBa}$	1.73e-05	7.18e-05	9.20e-06	1.71e-05	1.70e-05	4.80e-05	1.70e-05	1.70e-05
$\mathcal{A}_{OCa}$		1.89e-05	1.32e-06	9.23e-09	5.42e-09	1.22e-04	7.88e-09	4.43e-09
$\mathcal{D}_{OBu}$			3.02e-05	1.93e-05	1.93e-05	2.36e-04	1.94e-05	1.93e-05
$\mathcal{D}_{OBp}$				1.24e-06	1.22e-06	9.84e-05	1.22e-06	1.23e-06
$\mathcal{D}_{OCp}$					1.39e-09	1.22e-04	4.63e-10	1.85e-09
C^{max}_{OPG}						1.21e-04	3.57e-10	5.79e-11
k_{res}							1.21e-04	1.21e-04
$K_{a,[RANKL-RANK]}$								6.84e-10
$K_{a,[RANKL-OPG]}$								
$R^{TGF-\beta}_{act}$								
$R^{TGF-\beta}_{rep}$								
R^{max}_{RANKL}								
R^{max}_{OPG}								
R_{RANKL}								
$\mathcal{P}_{OBp}$								
$K^{RANK-RANKL}_{act,OCp}$								

	$R^{TGF-\beta}_{act}$	$R^{TGF-\beta}_{rep}$	R^{max}_{RANKL}	R^{max}_{OPG}	R_{RANKL}	$\mathcal{P}_{OBp}$	$K^{RANK-RANKL}_{act,OCp}$	k_{form}
$\mathcal{A}_{OBa}$	1.54e-06	1.19e-05	1.70e-05	1.70e-05	1.72e-05	3.53e-05	1.72e-05	7.19e-05
$\mathcal{A}_{OCa}$	8.71e-06	5.32e-07	5.42e-09	5.98e-09	8.43e-10	3.22e-06	8.38e-10	1.90e-05
$\mathcal{D}_{OBu}$	5.28e-05	2.58e-05	1.93e-05	1.94e-05	1.91e-05	6.68e-06	1.91e-05	4.20e-11
$\mathcal{D}_{OBp}$	3.35e-06	1.77e-07	1.22e-06	1.22e-06	1.27e-06	8.64e-06	1.27e-06	3.03e-05
$\mathcal{D}_{OCp}$	8.51e-06	4.81e-07	1.39e-09	1.16e-09	5.32e-09	3.34e-06	5.33e-09	1.93e-05
C^{max}_{OPG}	8.47e-06	4.70e-07	9.82e-16	1.77e-11	2.08e-09	3.37e-06	2.09e-09	1.94e-05
k_{res}	6.64e-05	1.07e-04	1.21e-04	1.21e-04	1.22e-04	1.65e-04	1.22e-04	2.36e-04
$K_{a,[RANKL-RANK]}$	8.46e-06	4.68e-07	3.56e-10	2.21e-10	3.87e-09	3.37e-06	3.88e-09	1.94e-05
$K_{a,[RANKL-OPG]}$	8.49e-06	4.74e-07	5.84e-11	1.39e-10	1.46e-09	3.36e-06	1.47e-09	1.94e-05
$R^{TGF-\beta}_{act}$		5.00e-06	8.47e-06	8.47e-06	8.60e-06	2.24e-05	8.60e-06	5.29e-05
$R^{TGF-\beta}_{rep}$			4.70e-07	4.69e-07	5.02e-07	6.35e-06	5.02e-07	2.59e-05
R^{max}_{RANKL}				1.75e-11	2.08e-09	3.37e-06	2.09e-09	1.94e-05
R^{max}_{OPG}					2.46e-09	3.37e-06	2.47e-09	1.94e-05
R_{RANKL}						3.29e-06	7.04e-15	1.92e-05
$\mathcal{P}_{OBp}$							3.29e-06	6.71e-06
$K^{RANK-RANKL}_{act,OCp}$								1.92e-05

Table 5.4: Direct comparison of the model output obtained by varying two distinct parameters based on the OFAT-method for load case III, calculated via Eq. (5.4). The matrix is in fact symmetric, *i.e.* the empty entries can be filled by flipping the upper half of the matrix over the diagonal; the entries of the diagonal are of course 0.

	$\mathcal{A}_{OCa}$	$\mathcal{D}_{OBu}$	$\mathcal{D}_{OBp}$	$\mathcal{D}_{OCp}$	C^{max}_{OPG}	k_{res}	$K_{a,[RANKL-RANK]}$	$K_{a,[RANKL-OPG]}$
$\mathcal{A}_{OBa}$	1.09e-06	2.68e-05	8.90e-07	1.01e-06	1.07e-06	2.12e-07	1.02e-06	1.08e-06
$\mathcal{A}_{OCa}$		1.71e-05	1.05e-08	2.47e-09	5.56e-10	2.26e-06	1.81e-09	1.89e-10
$\mathcal{D}_{OBu}$			1.80e-05	1.74e-05	1.72e-05	3.18e-05	1.74e-05	1.71e-05
$\mathcal{D}_{OBp}$				4.08e-09	7.96e-09	1.97e-06	4.34e-09	9.67e-09
$\mathcal{D}_{OCp}$					9.09e-10	2.15e-06	1.01e-10	1.66e-09
C^{max}_{OPG}						2.23e-06	5.80e-10	1.33e-10
k_{res}							2.16e-06	2.25e-06
$K_{a,[RANKL-RANK]}$								1.19e-09
$K_{a,[RANKL-OPG]}$								
$R^{TGF-\beta}_{act}$								
$R^{TGF-\beta}_{rep}$								
R^{max}_{RANKL}								
R^{max}_{OPG}								
R_{RANKL}								
$\mathcal{P}_{OBp}$								
$K^{RANK-RANKL}_{act,OCp}$								

	$R^{TGF-\beta}_{act}$	$R^{TGF-\beta}_{rep}$	R^{max}_{RANKL}	R^{max}_{OPG}	R_{RANKL}	$\mathcal{P}_{OBp}$	$K^{RANK-RANKL}_{act,OCp}$	k_{form}
$\mathcal{A}_{OBa}$	9.92e-11	9.99e-07	1.06e-06	1.02e-06	1.08e-06	2.79e-06	1.08e-06	2.73e-05
$\mathcal{A}_{OCa}$	1.11e-06	2.47e-09	6.29e-10	1.68e-09	1.96e-10	3.99e-07	1.82e-10	1.75e-05
$\mathcal{D}_{OBu}$	2.69e-05	1.75e-05	1.72e-05	1.74e-05	1.71e-05	1.23e-05	1.71e-05	2.39e-09
$\mathcal{D}_{OBp}$	9.08e-07	3.17e-09	7.46e-09	4.59e-09	9.51e-09	5.34e-07	9.73e-09	1.84e-05
$\mathcal{D}_{OCp}$	1.03e-06	1.94e-10	7.64e-10	1.19e-10	1.60e-09	4.49e-07	1.69e-09	1.78e-05
C^{max}_{OPG}	1.09e-06	1.10e-09	8.10e-12	4.93e-10	1.17e-10	4.14e-07	1.41e-10	1.76e-05
k_{res}	2.03e-07	2.13e-06	2.22e-06	2.16e-06	2.25e-06	4.54e-06	2.26e-06	3.24e-05
$K_{a,[RANKL-RANK]}$	1.04e-06	1.04e-10	4.54e-10	3.69e-12	1.13e-09	4.45e-07	1.21e-09	1.78e-05
$K_{a,[RANKL-OPG]}$	1.10e-06	1.85e-09	1.92e-10	1.07e-09	7.06e-13	4.02e-07	1.21e-13	1.75e-05
$R^{TGF-\beta}_{act}$		1.02e-06	1.08e-06	1.04e-06	1.10e-06	2.82e-06	1.10e-06	2.74e-05
$R^{TGF-\beta}_{rep}$			9.18e-10	1.41e-10	1.78e-09	4.56e-07	1.87e-09	1.79e-05
R^{max}_{RANKL}				3.78e-10	1.72e-10	4.17e-07	2.02e-10	1.76e-05
R^{max}_{OPG}					1.01e-09	4.42e-07	1.09e-09	1.78e-05
R_{RANKL}						4.03e-07	1.37e-12	1.76e-05
$\mathcal{P}_{OBp}$							4.02e-07	1.27e-05
$K^{RANK-RANKL}_{act,OCp}$								1.75e-05

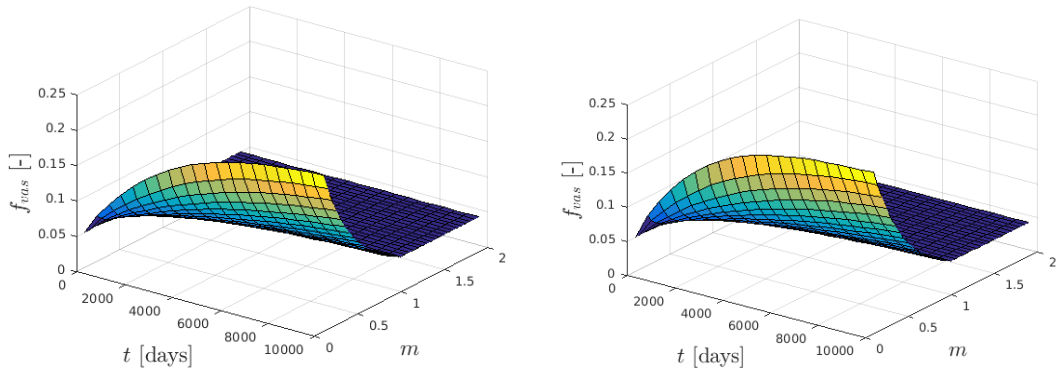

(a) L I, $K_{a,[RANKL-OPG]}$

(b) L I, $K_{act,OCp}^{RANK-RANKL}$

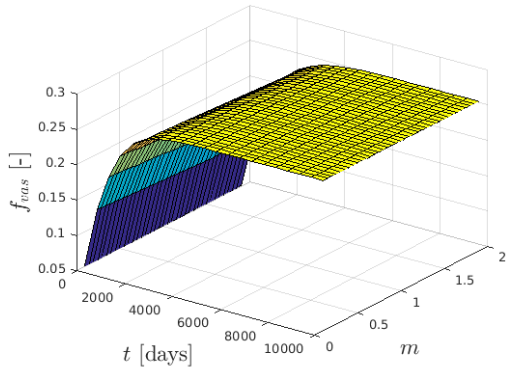

(c) L II, $K_{a,[RANKL-OPG]}$

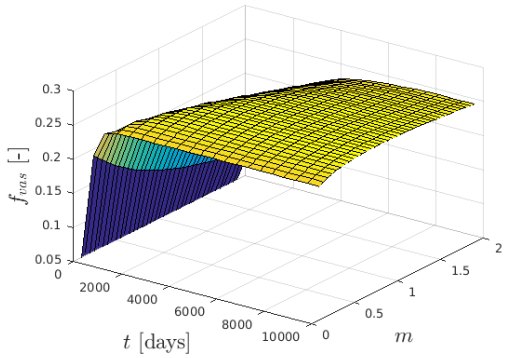

(d) L II, $K_{act,OCp}^{RANK-RANKL}$

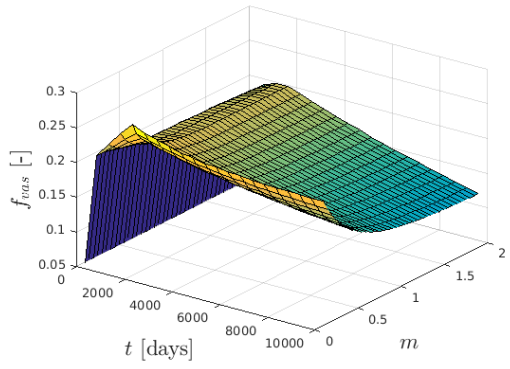

(e) L III, $K_{a,[RANKL-OPG]}$

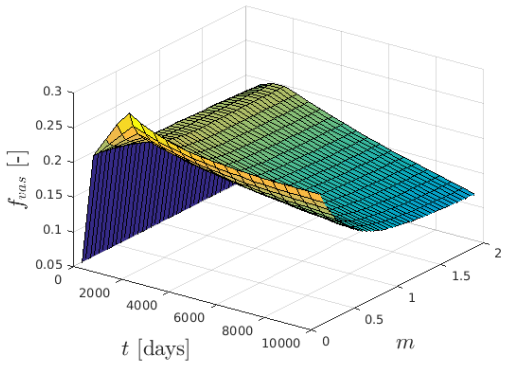

(f) L III, $K_{act,OCp}^{RANK-RANKL}$

Figure 5.38: Evolution of the vascular porosities f_{vas} over time, for variations of the parameters $K_{a,[RANKL-OPG]}$ and $K_{act,OCp}^{RANK-RANKL}$, for all three load cases.

It is emphasized that the similarity of the graphs in Figure 5.38 is exceptional and not obtained for arbitrary pairs of parameters, see for example Figure 5.39.

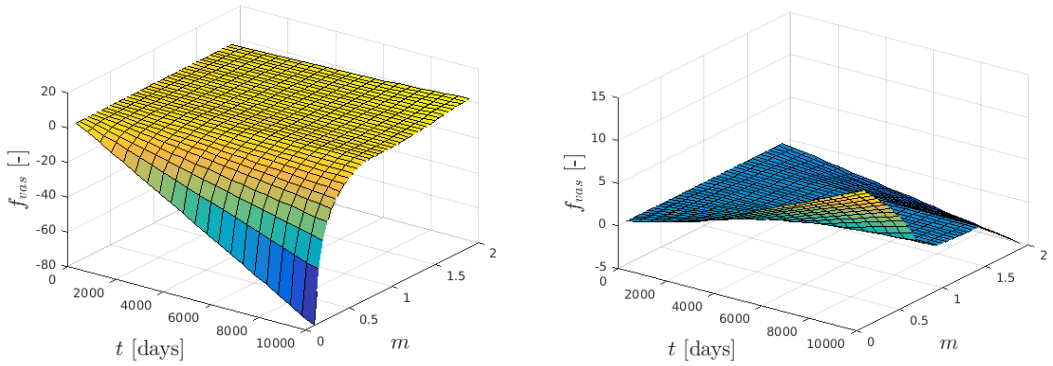

(a) L II, $\mathcal{A}_{OBa}$ (b) L II, $\mathcal{D}_{OBu}$

Figure 5.39: Evolution of the vascular porosities f_{vas} over time, for variations of the parameters $\mathcal{A}_{OBa}$ and $\mathcal{D}_{OBu}$, for load case II.

5.2.2 Establishment of functional relations describing sensitivity measure

In order to detect functional relations between two variables apart from linear and monotonic ones, which can easily be derived by means of correlation measures, one can use regression to calculate the best-approximating curve of a specific shape and then estimate the MSE or MSRE. Figures 5.40 to 5.42 show the regression results for the MSRE for the three exemplary parameters $\mathcal{A}_{OBa}$, $\mathcal{D}_{OCp}$ and $\mathcal{P}_{OBp}$, when varied by a factor m within the reasonable interval given in Table 5.1 for all load cases. The regression curves were generated by means of the Matlab function `fit`. The green curve shows the quadratic regression function, the red graph the cubic one, the blue graph presents the exponential regression function and the magenta curve shows the best-approximating rational function that has linear polynomials in the nominator and denominator (*i.e.* a function $f(x)$ of the form $f(x) = \frac{ax+b}{cx+d}$).

For $\mathcal{A}_{OBa}$ and $\mathcal{P}_{OBp}$, the cubic curve seems to provide the best fit, while the exponential curve might be a better approximation for variations of $\mathcal{D}_{OCp}$. The rational fit yields rather bad approximations for all the considered parameters and load cases. Note that, by using this approach, one can test for various different functional relationships. However, it is emphasized that the method solely tests for the qualitative dependence of the MSRE on the respective parameter, while forgetting about the quantitative aspect, *i.e.* the magnitude of the influence of this parameter on the model. Thus, further investigations are necessary in order to enable predictions on the precise relation between a parameter and the model.

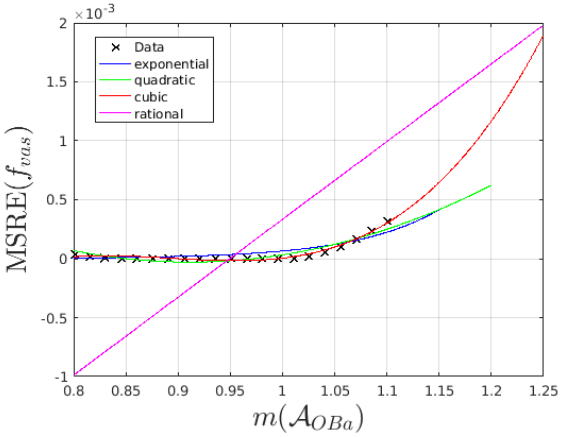

L I: $f_1 = 2.741e-10 \cdot \exp 12.38x$, $f_2 = 0.00784x^2 - 0.01429x + 0.006485$, $f_3 = 0.04569x^3 - 0.1224x^2 + 0.1087x - 0.03204$, $f_4 = \frac{0.8495x-0.8066}{x+127.6}$

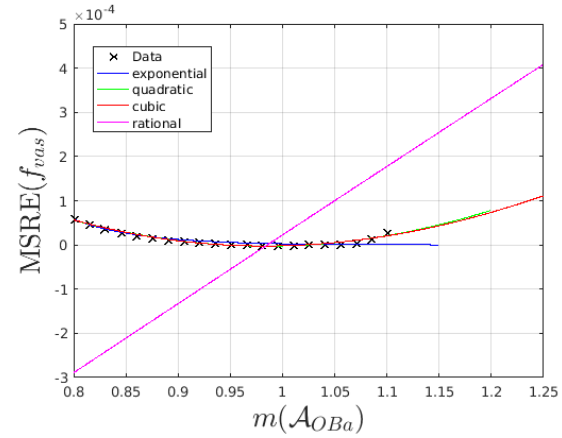

L II: $g_1 = 12.76 \cdot \exp -15.39x$, $g_2 = 0.001737x^2 - 0.003419x + 0.001679$, $g_3 = -0.0004036x^3 + 0.002888x^2 - 0.004506x + 0.00202$, $g_4 = \frac{0.07483x-0.07374}{x+47.19}$

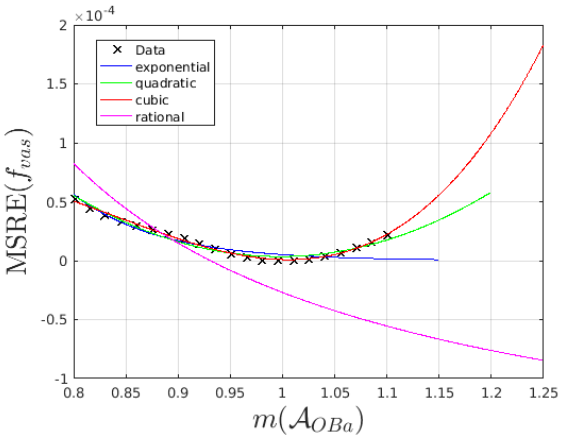

L III: $h_1 = 0.8034 \cdot \exp -11.96x$, $h_2 = 0.001331x^2 - 0.002655x + 0.001327$, $h_3 = 0.00421x^3 - 0.01067x^2 + 0.00868x - 0.002223$, $h_4 = \frac{-0.0002061x+0.0001919}{x-0.4727}$

Figure 5.40: Nonlinear fit for the MSRE over the factor m by which the parameter $\mathcal{A}_{OBa}$ is varied, for all three load cases.

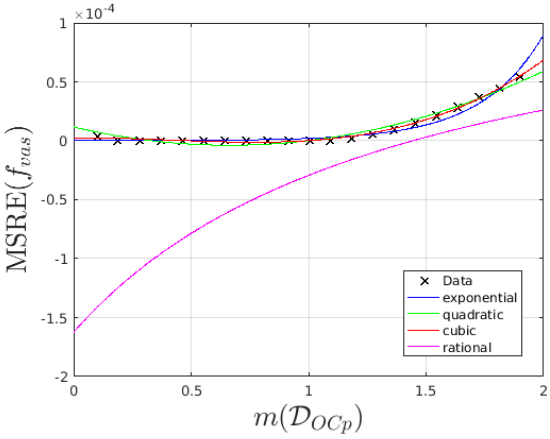

L I: $f_1 = 4.539e-08 \cdot \exp 3.796x$, $f_2 = 3.523e-05x^2 - 4.679e-05x + 1.172e-05$, $f_3 = 2.016e-05x^3 - 2.526e-05x^2 + 2.958e-06x + 2.298e-06$, $f_4 = \frac{0.0001606x - 0.0002318}{x + 1.428}$

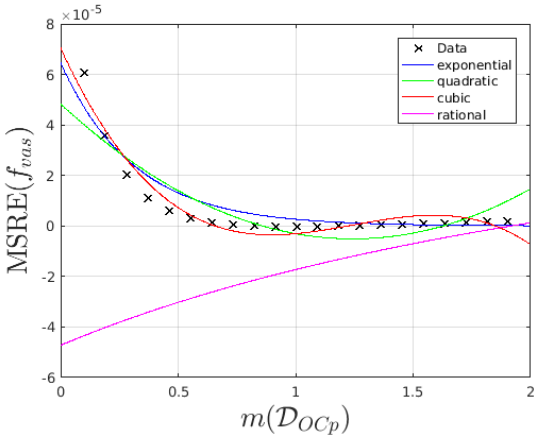

L II: $g_1 = 6.462e-05 \cdot \exp -3.189x$, $g_2 = 3.456e-05x^2 - 8.593e-05x + 4.831e-05$, $g_3 = -4.737e-05x^3 + 0.0001767x^2 - 0.0002028x + 7.043e-05$, $g_4 = \frac{8.021e-05x - 0.0001537}{x + 3.254}$

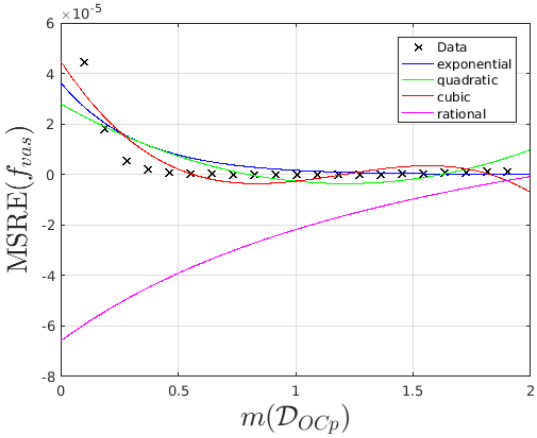

L III:$h_1 = 3.643e-05 \cdot \exp -3.097x$, $h_2 = 2.154e-05x^2 - 5.216e-05x + 2.794e-05$, $h_3 = -3.624e-05x^3 + 0.0001303x^2 - 0.0001416x + 4.486e-05$, $h_4 = \frac{5.845e-05x - 0.00012}{x + 1.819}$

Figure 5.41: Nonlinear fit for the MSRE over the factor m by which the parameter $\mathcal{D}_{OCp}$ is varied, for all three load cases.

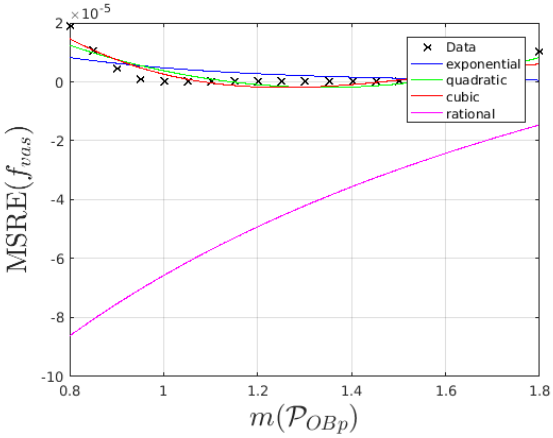

L I: $f_1 = 7.371e-05 \cdot \exp -2.738x$, $f_2 = 4.87e-05x^2 - 0.0001307x + 8.58e-05$, $f_3 = -5.256e-05x^3 + 0.0002537x^2 - 0.0003885x + 0.00019$, $f_4 = \frac{0.0001035x-0.0002251}{x+0.85}$

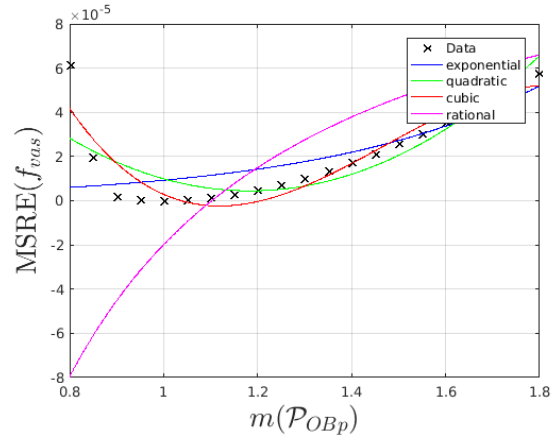

L II: $g_1 = 1.074e-06 \cdot \exp 2.155x$, $g_2 = 0.0001611x^2 - 0.0003817x + 0.0002305$, $g_3 = -0.0003157x^3 + 0.001392x^2 - 0.00193x + 0.0008565$, $g_4 = \frac{0.0001478x-0.000163}{x-0.2383}$

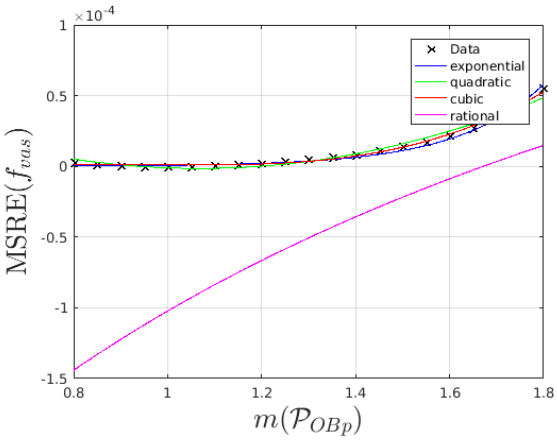

L III: $h_1 = 2.94e-09 \cdot \exp 5.495x$, $h_2 = 9.321e-05x^2 - 0.000199x + 0.0001047$, $h_3 = 9.657e-05x^3 - 0.0002834x^2 + 0.0002747x - 8.679e-05$, $h_4 = \frac{0.000386x-0.0006453}{x+1.535}$

Figure 5.42: Nonlinear fit for the MSRE over the factor m by which the parameter $\mathcal{P}_{OBp}$ is varied, for all three load cases.

5.3 Two-dimensional (TwFAT) sensitivity analyses

When aiming to detect interrelations between the individual model parameters the OFAT method reaches its limits, since it requires to change several parameter values simultaneously. Within this section all various possible 2-parameter-combinations are considered for that purpose, *i.e.* $\binom{17}{2} = 136$ combinations. The advantage of varying not more than two parameters at the same time, while keeping all remaining parameters constant, is on the one hand that it allows for relatively simple interpretations of the results, and on the other hand that it enables a visualization by means of surface plots.

Figure 5.43 shows the surface plots for varying the parameter pairs $(\mathcal{A}_{OCa}, k_{form})$, $(\mathcal{A}_{OCa}, \mathcal{D}_{OBp})$, $(R_{RANKL}, \mathcal{P}_{OBp})$ and $(R^{max}_{OPG}, R_{RANKL})$ within the intervals given in Table 5.1 when considering load case I. When comparing the plots in Figure 5.43 with the results from the OFAT-method (see Figure 5.36), it seems that the errors are just amplified, while the qualitative behavior of the model stays unaltered.

For the pairs $(\mathcal{A}_{OCa}, k_{form})$ and $(R_{RANKL}, \mathcal{P}_{OBp})$ the MSRE reaches its maximum when both parameters are small. This behavior reflects exactly the OFAT-results, which are given in Figure 5.36. In case of the pairs $(\mathcal{A}_{OCa}, \mathcal{D}_{OBp})$ and $(R^{max}_{OPG}, R_{RANKL})$ the MSRE is maximal when $\mathcal{A}_{OCa}$, and R_{RANKL} respectively, is large, while the respective other parameter is small. By taking a look at Figure 5.36 one can see that this phenomenon again just presents an amplification of the already obtained OFAT-errors. Thus, it is rather unlikely that the model comprises a direct relationship between the respective two parameters.

The majority of the 2-parameter-combinations yields surface plots that are qualitatively of the same nature as the ones given in Figure 5.43, *i.e.* they essentially just reflect the OFAT-data. When investigating parameter combinations that contain C^{max}_{OPG}, one can see that this particular parameter does rarely contribute to the MSRE, while the errors are solely determined by altering the respective other parameter value, see Figure 5.44.

However, there are some parameter combinations that yield a qualitative change of the models behavior compared to when altering the parameters separately, indicating a potential dependence between these respective parameters. Figure 5.45 (a) shows the surface plot resulting from simultaneous alteration of the two parameters k_{res} and k_{form}, which exhibits its peak for k_{res} being small and k_{form} being large. This phenomenon can not be observed by means of the OFAT-analysis, see Figure 5.36. However, considering Eq. (3.7) that comprises the connection between k_{form} and k_{res},

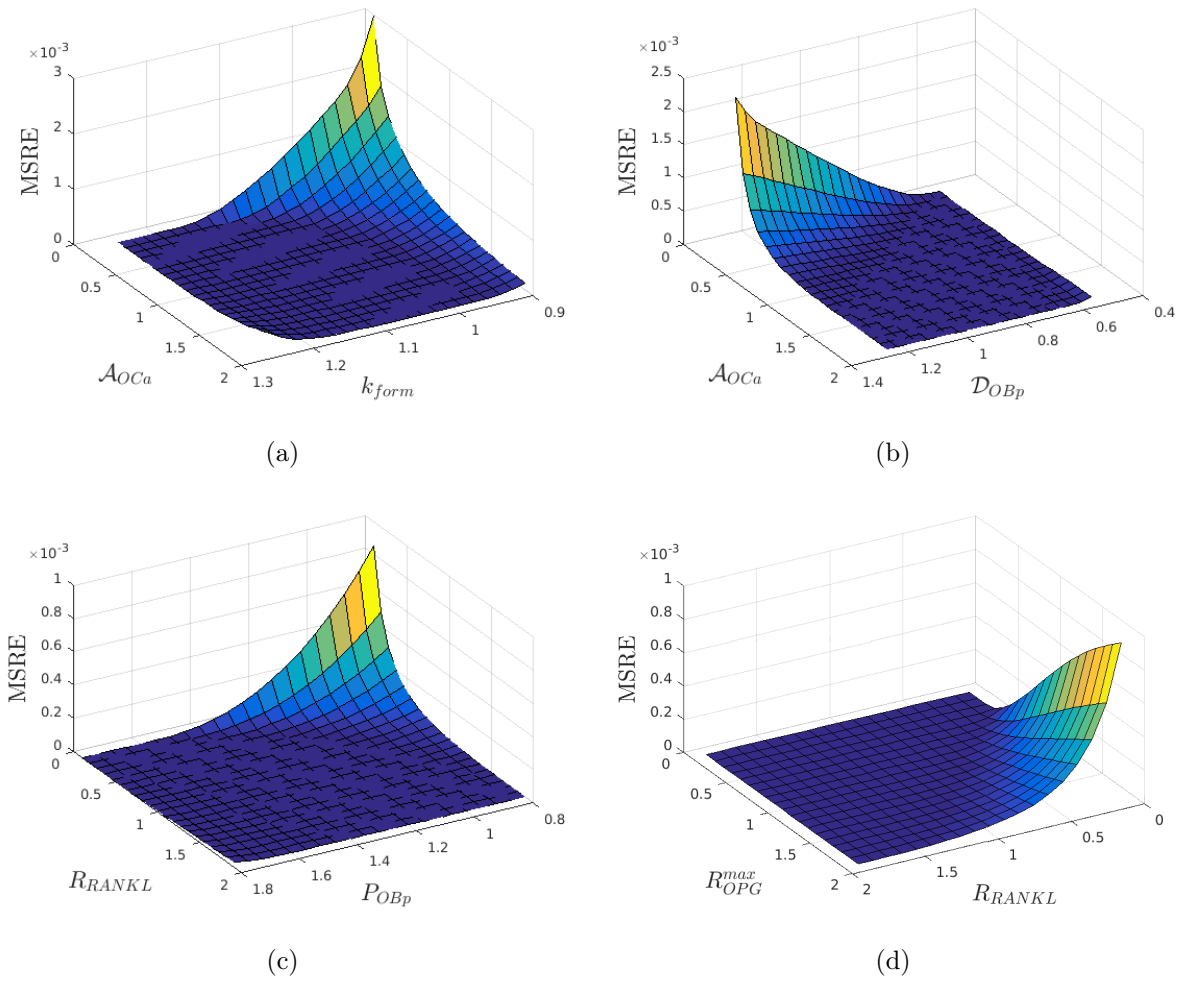

Figure 5.43: Surface plots showing the MSRE upon simultaneous variation of two parameters in load case I: (a) $(\mathcal{A}_{OCa}, k_{form})$, (b) $(\mathcal{A}_{OCa}, \mathcal{D}_{OBp})$, (c) $(R_{RANKL}, \mathcal{P}_{OBp})$ and (d) $(R^{max}_{OPG}, R_{RANKL})$. The x- and y-axis show the factors by which the respective parameters have been varied.

the respective behavior seems quite reasonable. When decreasing the osteoclastic resorption rate and at the same time increasing the osteoblastic formation rate, the vascular porosity will obviously experience considerable disturbances. The same is true for the parameters $K_{a,[RANKL-RANK]}$ and $K_{a,[RANKL-OPG]}$, see Figure 5.45 (d), when considering their role in the RANK-RANKL-OPG pathway.

For simultaneous variation of the parameter pairs ($\mathcal{D}_{OBp}$, $K_{a,[RANKL-RANK]}$) and ($\mathcal{A}_{OCa}$, $\mathcal{D}_{OCp}$) the qualitative behavior of the MSRE also shows some discrepancies when compared to the OFAT-results, see Figure 5.45 (b) and (c). For all combinations shown in Figure 5.45 one would assume the MSRE to reach its greatest value

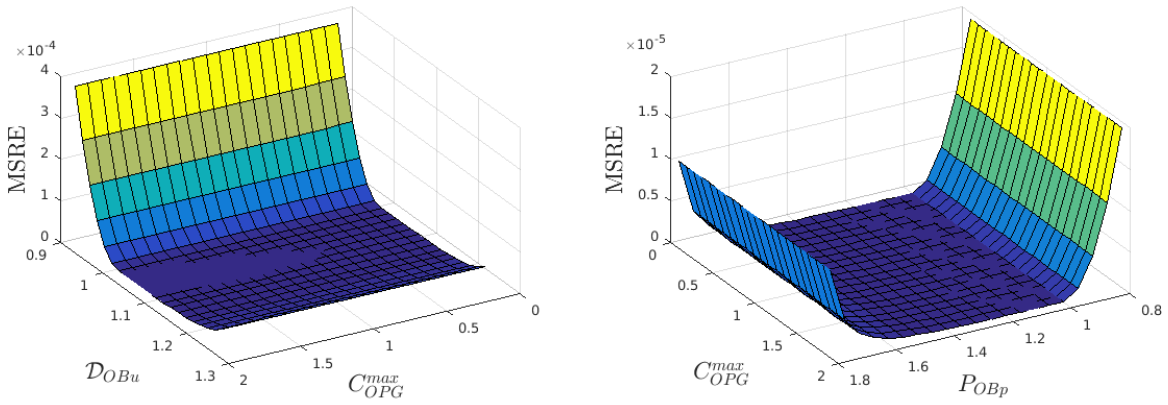

(a) (b)

Figure 5.44: Surface plots showing the MSRE upon simultaneous variation of (a) $\mathcal{D}_{OBu}$ and C^{max}_{OPG}, and (b) C^{max}_{OPG} and $\mathcal{P}_{OBp}$, for load case I. The x- and y-axis show the factors by which the parameters have been varied.

upon decreasing both parameter values to 10% of its original value. The fact that this is not the case suggests a relation between the parameters that might be hidden in the complex structure of the model. However, special care is advised when observing such relations between parameters. Even though there might be a dependence between some parameters of the mathematical model, it is not guaranteed that this dependence is actually based on biological evidence. Nevertheless, it allows a deeper insight in the structure of the model and may act as inspiration for further studies on this topic.

The results presented in this subsection are with respect to load case I. However, all calculations for the TwFAT-analysis have been performed for load case II and III as well. Since they do not entail any further insights, but essentially yield the same conclusions as for load case I, the surface plots for the disuse and osteoporosis scenarios are omitted here.

5.4 Three-dimensional (ThFAT) sensitivity analyses

When varying more than two parameters simultaneously, suitable methods for a graphical representation of the results are, for obvious reasons, not available.. As a consequence, the MSRE, as well as the factors by which the respective parameters are varied, are summarized in a table and further investigated by means of pattern recognition.

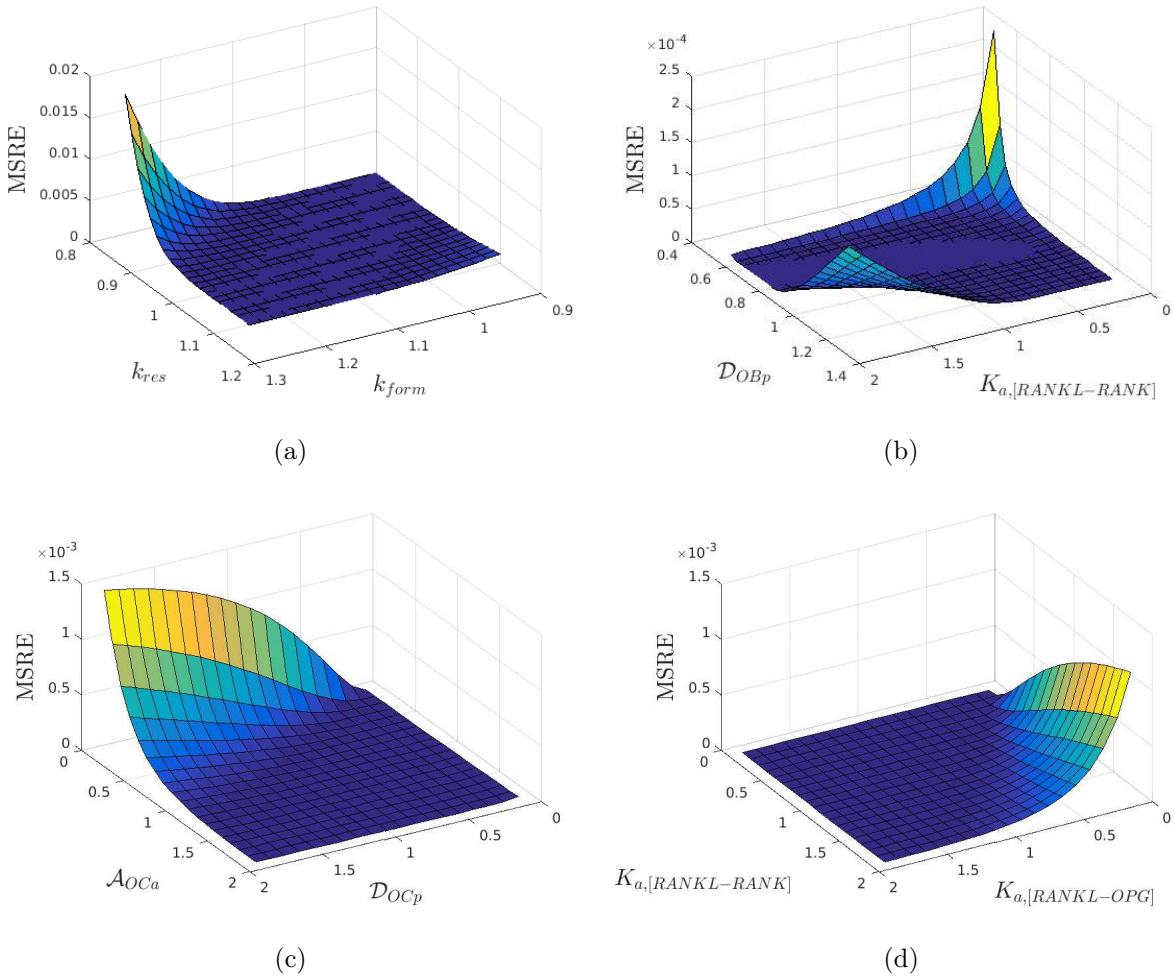

Figure 5.45: Surface plots showing the MSRE upon simultaneous variation of (a) k_{res} and k_{form}, (b) $\mathcal{D}_{OBp}$ and $K_{a,[RANKL-RANK]}$, (c) $\mathcal{A}_{OCa}$ and $\mathcal{D}_{OCp}$, and (d) $K_{a,[RANKL-RANK]}$ and $K_{a,[RANKL-OPG]}$, for load case I. The x- and y-axis show the factors by which the parameters have been varied.

Running the model for variations of all possible 3-parameter combinations yields extremely long computational times. Thus, it is recommended to first cluster the parameters in groups where interrelations are reasonable from a biological point of view.

Table 5.5 summarizes selected (representative) results for the MSRE arising upon simultaneous alteration of the three parameters $K_{a,[RANKL-RANK]}$, $K_{a,[RANKL-OPG]}$ and $K_{act,OCp}^{RANK-RANKL}$, when simulating the disuse scenario, *i.e.* load case III. It can be observed that the model reacts more sensitively to changes of $K_{a,[RANKL-RANK]}$ and $K_{a,[RANKL-OPG]}$, while varying $K_{act,OCp}^{RANK-RANKL}$ induces minor effects. More precisely, the highest errors are obtained for increasing one of the first-mentioned parameters

while decreasing the respective other one. This phenomenon was already observed by means of the TwFAT-analysis, see Figure 5.45 (d). However, for elevated levels of both $K_{a,[RANKL-RANK]}$ and $K_{a,[RANKL-OPG]}$, the MSRE reaches rather high values upon a drastic decrease of $K_{act,OCp}^{RANK-RANKL}$ to 10% of its original value. Decreasing both parameters, $K_{a,[RANKL-RANK]}$ and $K_{a,[RANKL-OPG]}$, leads in turn to a less distinct increase of the MSRE regardless of the alteration of $K_{act,OCp}^{RANK-RANKL}$.

Finally, it is emphasized that this approach of using some design of experiments (DOE) and summarizing the results in tables that are further studied by means of pattern recognition, works for arbitrarily many parameters. Thus, it is a widely applicable method, that provides a profound insight into the model mechanics and therefore constitutes a very strong analysis tool.

5.5 Correlation studies between variation factor and sensitivity measure

The next goal of the sensitivity analysis is to calculate interesting key measures that allow for conclusions concerning the influence, interaction and significance of the model parameters. The most common key measures are the so-called correlation coefficients. For that matter, the most popular one is the Pearson's correlation coefficient, ρ, which tests for a linear relation between two variables. It is calculated via

$$\rho = \frac{\mathbb{E}\left[(X-\mu_X)(Y-\mu_Y)\right]}{\sigma_X \sigma_Y} \tag{5.5}$$

where μ and σ denote the mean and standard deviation of the respective variable and $\mathbb{E}$ the expected value. Using

$$\begin{aligned}
\mu_X &= \mathbb{E}_X, \\
\mu_Y &= \mathbb{E}_Y, \\
\sigma_X^2 &= \mathbb{E}(X^2) - (\mathbb{E}X)^2, \\
\sigma_Y^2 &= \mathbb{E}(Y^2) - (\mathbb{E}Y)^2, \\
\mathbb{E}\left[(X-\mu_X)(Y-\mu_Y)\right] &= \mathbb{E}(XY) - \mathbb{E}X\mathbb{E}Y,
\end{aligned}$$

Eq. (5.5) can be rewritten as

$$\rho = \frac{\mathbb{E}(XY) - \mathbb{E}X\mathbb{E}Y}{\sqrt{\mathbb{E}(X^2) - (\mathbb{E}X)^2}\sqrt{\mathbb{E}(Y^2) - (\mathbb{E}Y)^2}}.$$

For a sample with points x_i, where $i = 1, \ldots, n$, the expectation is calculated via

$$\mathbb{E}X = \bar{x} = \frac{1}{n}\sum_{i=1}^{n} x_i.$$

Table 5.5: Summary of representative examples of the MSRE, according to Eq. (5.1), for simultaneous variation of $K_{a,[RANKL-RANK]}$, $K_{a,[RANKL-OPG]}$ and $K_{act,OCp}^{RANK-RANKL}$ for load case III. The first column contains the MSRE, while the three rightmost columns contain the factors by which the respective parameter is varied (column 2: $K_{a,[RANKL-RANK]}$, column 3: $K_{a,[RANKL-OPG]}$, column 4: $K_{act,OCp}^{RANK-RANKL}$). The yellow lines mark the parameter combinations that yield the greatest values.

2.0484e-06	0.1	0.4	0.1	1.8459e-05	1.3	1.6	0.1	2.1951e-05	1.6	1.6	0.1
1.4807e-07	0.1	0.4	0.4	1.2798e-06	1.3	1.6	0.4	2.4690e-06	1.6	1.6	0.4
4.4792e-07	0.1	0.4	0.7	3.6082e-08	1.3	1.6	0.7	2.3352e-07	1.6	1.6	0.7
7.9917e-07	0.1	0.4	1	2.5748e-08	1.3	1.6	1	3.2998e-10	1.6	1.6	1
1.2662e-06	0.1	0.4	1.3	1.1818e-07	1.3	1.6	1.3	4.1913e-08	1.6	1.6	1.3
1.8706e-06	0.1	0.4	1.6	2.1555e-07	1.3	1.6	1.6	1.1937e-07	1.6	1.6	1.6
2.6150e-06	0.1	0.4	1.9	3.0941e-07	1.3	1.6	1.9	1.9879e-07	1.6	1.6	1.9
1.9084e-07	0.1	1.9	0.1	3.8746e-05	1.6	0.1	0.1	3.7748e-05	1.9	0.1	0.1
2.4785e-06	0.1	1.9	0.4	3.8536e-05	1.6	0.1	0.4	3.9997e-05	1.9	0.1	0.4
7.1233e-06	0.1	1.9	0.7	3.0704e-05	1.6	0.1	0.7	3.3167e-05	1.9	0.1	0.7
1.2529e-05	0.1	1.9	1	2.4704e-05	1.6	0.1	1	2.7340e-05	1.9	0.1	1
1.7663e-05	0.1	1.9	1.3	1.9996e-05	1.6	0.1	1.3	2.2796e-05	1.9	0.1	1.3
2.2240e-05	0.1	1.9	1.6	1.6088e-05	1.6	0.1	1.6	1.8959e-05	1.9	0.1	1.6
2.6244e-05	0.1	1.9	1.9	1.2896e-05	1.6	0.1	1.9	1.5703e-05	1.9	0.1	1.9
3.9882e-05	1.3	0.1	0.1	2.9244e-05	1.6	1	0.1	2.7923e-05	1.9	1.3	0.1
3.6226e-05	1.3	0.1	0.4	6.9472e-06	1.6	1	0.4	5.9464e-06	1.9	1.3	0.4
2.7551e-05	1.3	0.1	0.7	1.7518e-06	1.6	1	0.7	1.3369e-06	1.9	1.3	0.7
2.1365e-05	1.3	0.1	1	3.9363e-07	1.6	1	1	2.4748e-07	1.9	1.3	1
1.6478e-05	1.3	0.1	1.3	5.1047e-08	1.6	1	1.3	1.6513e-08	1.9	1.3	1.3
1.2643e-05	1.3	0.1	1.6	9.0149e-11	1.6	1	1.6	6.1348e-09	1.9	1.3	1.6
9.6716e-06	1.3	0.1	1.9	2.4534e-08	1.6	1	1.9	4.6358e-08	1.9	1.3	1.9
2.1890e-05	1.3	1.3	0.1	2.5226e-05	1.6	1.3	0.1	2.1993e-05	1.9	1.9	0.1
2.4291e-06	1.3	1.3	0.4	4.1285e-06	1.6	1.3	0.4	2.4966e-06	1.9	1.9	0.4
2.2335e-07	1.3	1.3	0.7	6.8043e-07	1.6	1.3	0.7	2.4066e-07	1.9	1.9	0.7
1.2692e-10	1.3	1.3	1	6.1814e-08	1.6	1.3	1	5.2913e-10	1.9	1.9	1
4.4012e-08	1.3	1.3	1.3	1.8952e-09	1.6	1.3	1.3	4.0492e-08	1.9	1.9	1.3
1.2203e-07	1.3	1.3	1.6	4.5155e-08	1.6	1.3	1.6	1.1753e-07	1.9	1.9	1.6
2.0144e-07	1.3	1.3	1.9	1.0839e-07	1.6	1.3	1.9	1.9696e-07	1.9	1.9	1.9

As stated before, the Pearson's correlation coefficient is a measure for a linear correlation between two variables. A value of +1 implies that all data points lie on an increasing line, while a value of -1 is attained in case they lie on a decreasing line. A value of 0 indicates that the data sets are not linearly correlated, but there could be a nonlinear relation that can not be detected with the Pearson's correlation coefficient.

The Spearman correlation coefficient is defined as the Pearson correlation coefficient for the rank variables. The latter ones represent the order of the sample points, while forgetting about their exact values. Thus, the Spearman coefficient measures the likelihood of there being a monotonic relation between two variables. Thereby a value of 1 implies that there is a monotonically increasing relation between the two variables (which does not have to be linear), while a value of -1 indicates a monotonically decreasing relation.

One further correlation coefficient that is considered within this thesis is the partial ranked correlation coefficient. As the name indicates, this coefficient is a measure for the correlation of the rank variables and therefore provides insights as to how well the influence of the variables on the model can be described by a monotonic function. The advantage of partial correlations is that if the two variables are connected via other variables the effect of these confounding variables is removed. A partial correlation coefficient between two variables X and Y, while removing the effect of a parameter Z, can be written in terms of simple correlation coefficients as

$$\rho_{XY,Z} = \frac{\rho_{XY} - \rho_{XZ}\rho_{YZ}}{\sqrt{(1-\rho_{XZ}^2)(1-\rho_{YZ}^2)}}.$$

Thus, if X and Y are uncorrelated with Z, then $\rho_{XY,Z} = \rho_{XY}$. Just as the simple correlation coefficient describes the data in an ordinary scatter plot, the partial correlation coefficient describes the data in the partial regression residual plot. It is calculated as follows: Let Y and X_1 be the variables of primary interest and let $X_2, \dots X_p$ be the variables held fixed.

- First, calculate the residuals after regressing Y on $X_2, \dots X_p$. These are the parts of the Y's that cannot be predicted by $X_2, \dots X_p$.
- Then, calculate the residuals after regressing X_1 on $X_2, \dots X_p$. These are the parts of the X_1's that cannot be predicted by $X_2, \dots X_p$.
- The partial correlation coefficient between Y and X_1 adjusted for $X_2, \dots X_p$ is the correlation between these two sets of residuals.
- The regression coefficient when the Y residuals are regressed on the X_1 residuals is equal to the regression coefficient of X_1 in the multiple regression equation when Y is regressed on the entire set of predictors.

Table 5.6 contains the values of all the three introduced correlation coefficients between the individual parameters and the objective function MSRE in all three load cases. In order to calculate the correlation coefficients, 2000 random parameter settings were generated (within the bounds in Table 5.1), with the help of Matlabs function `sdo.sample`. By means of the function `sdo.analyze` the correlation coefficients were calculated after every 100 settings, such that one could see that the results converge rather quickly to the final values (obtained for 2000 settings). This procedure has been carried out for 3 different sets containing 2000 settings in order to guarantee that the obtained values are meaningful and not too closely dependent on the random parameter setting.

Table 5.6: Correlation coefficients for all three load cases (I, II, III); r_i denotes the Pearson coefficient, ρ_i denotes the Spearman coefficient, x_i denotes the ranked partial correlation coefficient.

Parameter	r_I	r_{II}	r_{III}	ρ_I	ρ_{II}	ρ_{III}	x_I	x_{II}	x_{III}
$\mathcal{A}_{OB_a}$	0.0265	-0.0025	-0.0165	-0.2877	-0.2796	-0.3827	-0.4179	-0.3862	-0.5094
$\mathcal{A}_{OC_a}$	-0.0484	-0.0654	-0.0663	0.0199	-0.0402	0.0221	0.0656	-0.0906	0.0281
$\mathcal{D}_{OB_u}$	-0.0181	-0.0175	-0.0178	0.2704	0.2737	0.3354	0.4002	0.3724	0.5128
$\mathcal{D}_{OB_p}$	0.0039	-0.0291	-0.0463	-0.3274	-0.3654	-0.3286	-0.4426	-0.4739	-0.5075
$\mathcal{D}_{OC_p}$	0.0293	0.0570	0.0365	-0.0593	-0.0206	-0.0636	-0.0754	-0.0180	-0.0859
C_{OPG}^{max}	-0.0121	0.0273	-0.0264	0.0089	0.0015	-0.0245	0.0010	-0.0038	0.0082
k_{res}	-0.0314	0.0181	-0.0187	-0.2911	-0.2286	-0.3184	-0.4136	-0.3321	-0.4707
$K_{a,[RANKL-RANK]}$	0.0234	0.0188	0.0377	-0.0603	-0.0405	-0.0190	-0.0713	-0.0369	-0.0216
$K_{a,[RANKL-OPG]}$	-0.0356	-0.0546	-0.0565	0.0492	0.0213	0.0061	0.0554	0.0212	0.0242
$R_{act}^{TGF-\beta}$	0.0200	0.0027	-0.0025	-0.2614	-0.2575	-0.3530	-0.3991	-0.3426	-0.4934
$R_{rep}^{TGF-\beta}$	-0.0395	-0.0594	-0.0294	-0.3474	-0.3788	-0.3556	-0.4886	-0.4989	-0.5100
R_{RANKL}^{max}	-0.0095	0.0020	-0.0086	0.0239	0.0279	-0.0093	0.0267	0.0033	0.0109
R_{OPG}^{max}	0.0321	0.0350	0.0318	-0.0322	-0.0080	-0.0171	-0.0182	-0.0024	-0.0433
R_{RANKL}	-0.0305	-0.0202	-0.0037	0.0313	-0.0086	-0.0432	0.0188	-0.0354	-0.0357
P_{OB_p}	0.0193	-0.0220	0.0009	0.0097	0.0055	-0.0537	-0.0185	0.0366	-0.0191
$K_{act,OC_p}^{RANK-RANKL}$	-0.0185	-0.0058	-0.0027	-0.0449	-0.0035	-0.0356	-0.0178	0.0152	-0.0097
k_{form}	-0.0203	-0.0449	-0.0208	0.0494	0.0120	-0.0386	0.0626	-0.0094	-0.0085

It can be seen that for all variables in the BCPM the Pearson correlation coefficients are very close to zero, which implies that the model does not depend linearly on any of its parameters. The smallest value is attained for C_{OPG}^{max}.

Furthermore, the values for the Spearman correlation coefficients are much greater than those for the Pearson coefficients. The greatest values are obtained for $\mathcal{A}_{OBa}$, $\mathcal{D}_{OBu}$, $\mathcal{D}_{OBp}$, k_{res}, R_{act}^{TGFb}, R_{rep}^{TGFb}. However, since the values are still a bit closer to 0 than to 1, it requires a more thorough investigation in order to predict a monotonic relation.

The values for the partial ranked correlations are slightly larger than the Spearman coefficients, but they are in a similar range. Absolute values of more than 0.5 are

achieved in load case III for $\mathcal{A}_{OBa}$, $\mathcal{D}_{OBu}$, $\mathcal{D}_{OBp}$, R_{rep}^{TGFb}. Thus, there is an amplified chance of there being a monotonic relation between some of the aforementioned parameters and the BCPM (or more precisely, the MSRE).

Comparing the values of the correlation coefficients for all three load cases, one can see, that they always attain roughly the same magnitude. However, one can not conclude that the model responds equally in all the load cases, but that the model response is just neither linear, nor monotonic, for all the considered scenarios. This explains, why for some parameters the sign of the correlation coefficient differs between the separate load cases.

Chapter 6

Discussion & Outlook

The model of Scheiner et al. (2013) is a conceptual model of bone remodeling (at the tissue level) aiming at comprehensively capturing its major regulatory mechanisms. Given the complexity of the process, it is not surprising that the number of model parameters is substantial. Hence, the aim of this study, namely reducing the number of and understanding the specific roles and meanings of the involved parameters, is extremely important in terms of eventually, in the long run, introducing mathematical modeling to clinical practice.

The first, and really straightforward attempt to approach the above-mentioned objective of this thesis was to merge model parameters which occur in groups, see Chapter 4. Based on very simple considerations, the number of model parameters could be reduced from 26 to 17. Nevertheless, the model accuracy and versatility was not compromised whatsoever. Hence, this strategy turned out as convincingly beneficial, as the number of free calibration parameters could be considerably reduced, by roughly 35 %. In further consequence, when aiming at designing an experimental campaign for actually measuring the model parameters, the respective effort would be much smaller.

Furthermore, sensitivity studies were performed with several different methods and strategies being thoroughly tested, see Chapter 5. While a well-defined recipe for such kind of study does not exist, the intuitively most obvious strategy would be to vary all parameters at the same time, and to analyze then the observed effects. However, for comprehensive models such as the one studied in this thesis, such approach is simply not feasible. Even for the reduced model, 17 parameters would need to be varied at the same time. While this is, in theory, possible and implementable utilizing standard mathematical software, the gained results would be extremely difficult (if not impossible) to understand. Hence, simplified sensitivity analysis modes were applied in the presented work. Varying just one, two, and groups of three parameters

at the same time, parameters could be discerned which are very influential for the model, while other parameters apparently only need to have the correct order of magnitude in order to make sure that the model predictions are not significantly altered. The implications of these results could again relate to the design of an experimental campaign for determining the parameters. The parameters which turned out as very influential should be determined as precisely as possible whereas the "not so important" parameters can also be merely estimated. It should be stressed in this context that the sensitivity studies involving variations of more than one parameter showed that the multi-dimensional sensitivity space of the studied model involves model behaviors which can simply not be revealed by varying only one parameter at a time, due to the multiple interrelations between parameters and model components. On the other hand, the more parameters are varied the more difficult the analysis of results becomes. Already when varying three parameters at once, some kind of pattern recognition techniques must be applied and just visually inspecting result plots does not suffice anymore.

Furthermore, also in Chapter 5, some additional studies related to the OFAT-method were carried out. First of all, direct comparisons of the results upon varying two arbitrary parameters were performed. For most parameters, the deviations were significant, whereas it has turned out that for a small number of parameter pairs the variations of both parameters had almost identical effects on the model predictions. This implies that parameters showing such kind of behavior could be linearly related by a fixed factor, implying additional model reductions. Correlation studies between parameters showed some moderate correlations between specific parameters, which could be interpreted in a similar way, hence relating these parameters by a suitable function could be a reasonable strategy. The third strategy in this line, *i.e.* fitting the objective functions of the sensitivity study by exponential, quadratic, cubic, and rational functions did not provide any additional insights, as the obtained fitting parameters varied strongly between the considered parameters.

In conclusion, the study presented in this thesis can be considered as some sort of benchmark model analysis. The results can certainly not be extrapolated or even directly used for different models but a suite of model analysis modalities could be pointed out which may prove useful for a wide range of different models and applications.

In the future, it may be reasonable to apply the very same analysis modalities to more recent versions of the model of Scheiner et al. (2013), e.g. the one by Pastrama et al. (2018), in order to check whether the insights gained in this work still hold. On the other hand, expanding on the idea of pattern recognition for multidimensional

sensitivity analysis could be a (challenging but) promising strategy. In any case, the presented work clearly shows that keeping models of complex processes as simple as possible is key for eventually establishing models which are actually applicable in clinical practice, and not only highly sophisticated toys without any real value.

Appendices

Appendix A

Additional plots

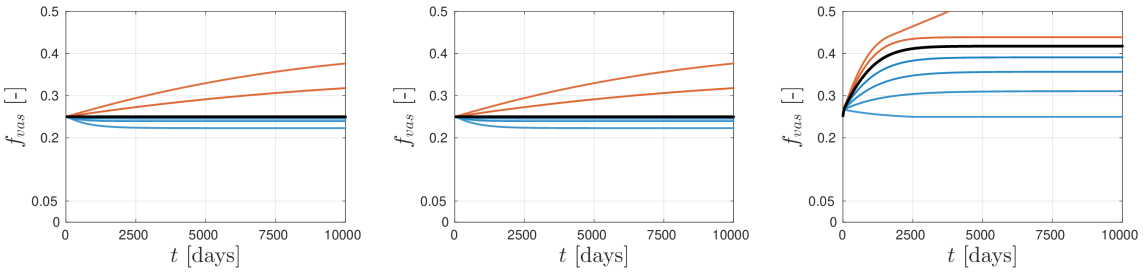

(a) L I, $\mathcal{A}_{OBa}$ (b) L II, $\mathcal{A}_{OBa}$ (c) L III, $\mathcal{A}_{OBa}$

Figure A.1: Model-predicted vascular porosities over time, when applying the OFAT-method for the parameter $\mathcal{A}_{OBa}$ and all three load cases, for $f_{vas,ini} = 0.25$.

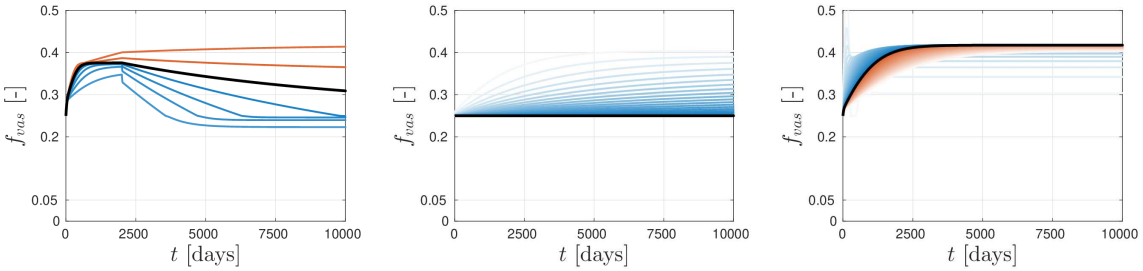

(a) L I, $\mathcal{A}_{OCa}$ (b) L II, $\mathcal{A}_{OCa}$ (c) L III, $\mathcal{A}_{OCa}$

Figure A.2: Model-predicted vascular porosities over time, when applying the OFAT-method for the parameter $\mathcal{A}_{OCa}$ and all three load cases, for $f_{vas,ini} = 0.25$.

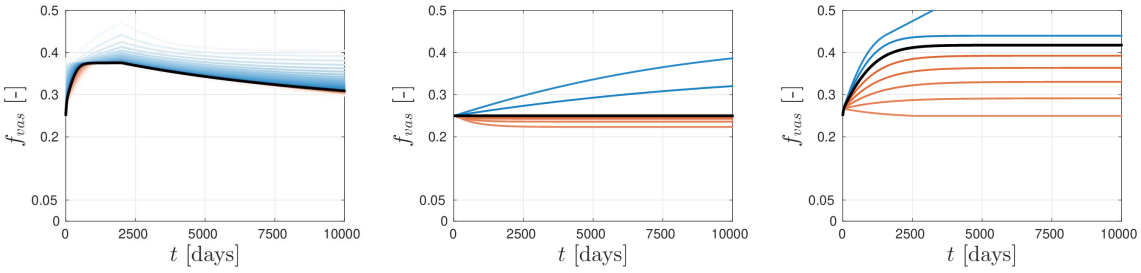

(a) L I, $\mathcal{D}_{OBu}$ (b) L II, $\mathcal{D}_{OBu}$ (c) L III, $\mathcal{D}_{OBu}$

Figure A.3: Model-predicted vascular porosities over time, when applying the OFAT-method for the parameter $\mathcal{D}_{OBu}$ and all three load cases, for $f_{vas,ini} = 0.25$.

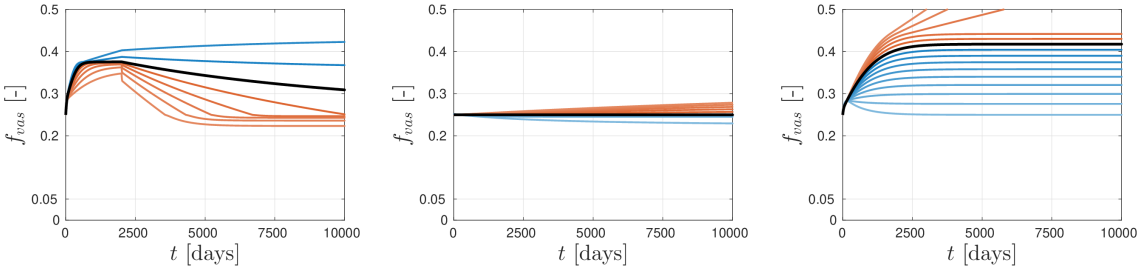

(a) L I, $\mathcal{D}_{OBp}$ (b) L II, $\mathcal{D}_{OBp}$ (c) L III, $\mathcal{D}_{OBp}$

Figure A.4: Model-predicted vascular porosities over time, when applying the OFAT-method for the parameter $\mathcal{D}_{OBp}$ and all three load cases, for $f_{vas,ini} = 0.25$.

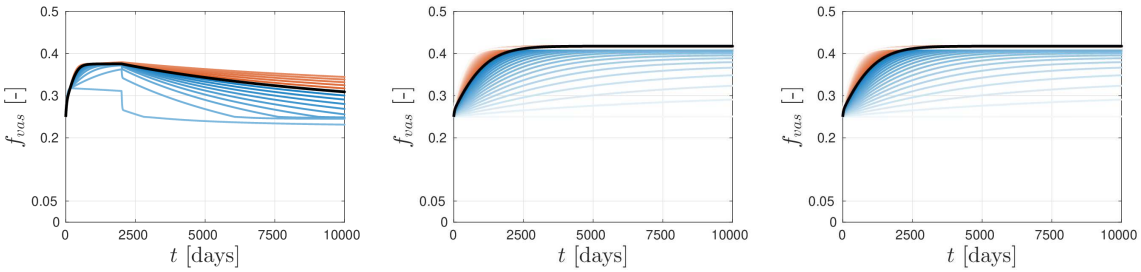

(a) L I, $\mathcal{D}_{OCp}$ (b) L II, $\mathcal{D}_{OCp}$ (c) L III, $\mathcal{D}_{OCp}$

Figure A.5: Model-predicted vascular porosities over time, when applying the OFAT-method for the parameter $\mathcal{D}_{OCp}$ and all three load cases, for $f_{vas,ini} = 0.25$.

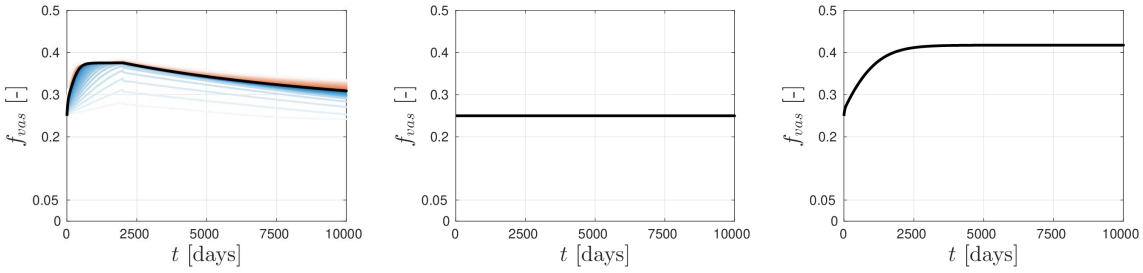

(a) L I, C_{OPG}^{max} (b) L II, C_{OPG}^{max} (c) L III, C_{OPG}^{max}

Figure A.6: Model-predicted vascular porosities over time, when applying the OFAT-method for the parameter C_{OPG}^{max} and all three load cases, for $f_{vas,ini} = 0.25$.

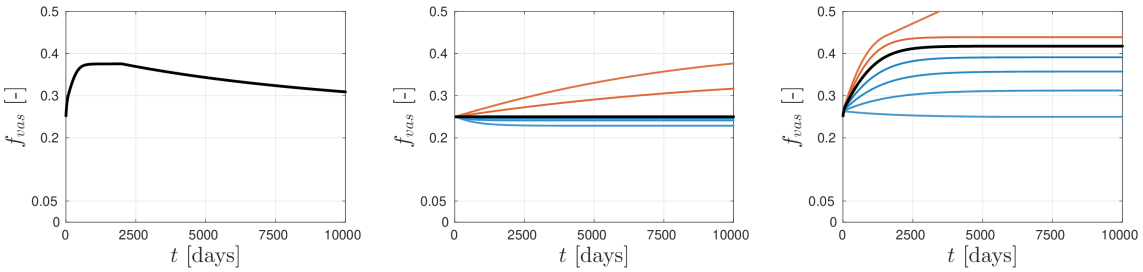

(a) L I, k_{res} (b) L II, k_{res} (c) L III, k_{res}

Figure A.7: Model-predicted vascular porosities over time, when applying the OFAT-method for the parameter k_{res} and all three load cases, for $f_{vas,ini} = 0.25$.

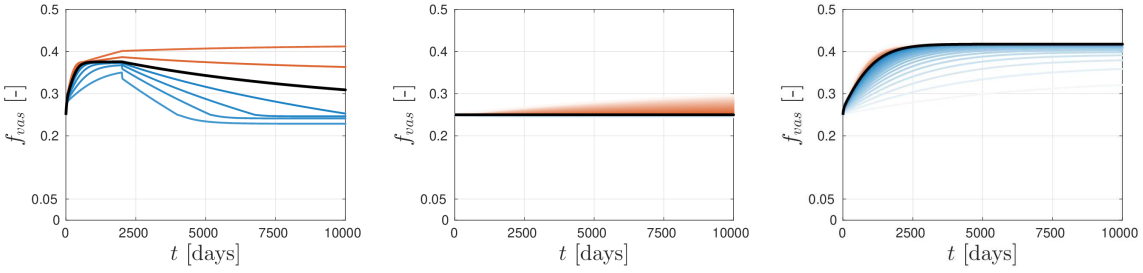

(a) L I, $K_{a,[RANKL-RANK]}$ (b) L II, $K_{a,[RANKL-RANK]}$ (c) L III, $K_{a,[RANKL-RANK]}$

Figure A.8: Model-predicted vascular porosities over time, when applying the OFAT-method for the parameter $K_{a,[RANKL-RANK]}$ and all three load cases, for $f_{vas,ini} = 0.25$.

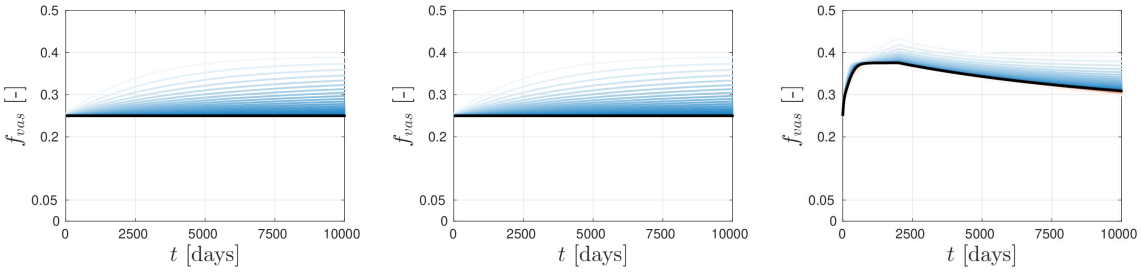

(a) L I, $K_{a,[RANKL-OPG]}$ (b) L II, $K_{a,[RANKL-OPG]}$ (c) L III, $K_{a,[RANKL-OPG]}$

Figure A.9: Model-predicted vascular porosities over time, when applying the OFAT-method for the parameter $K_{a,[RANKL-OPG]}$ and all three load cases, for $f_{vas,ini} = 0.25$.

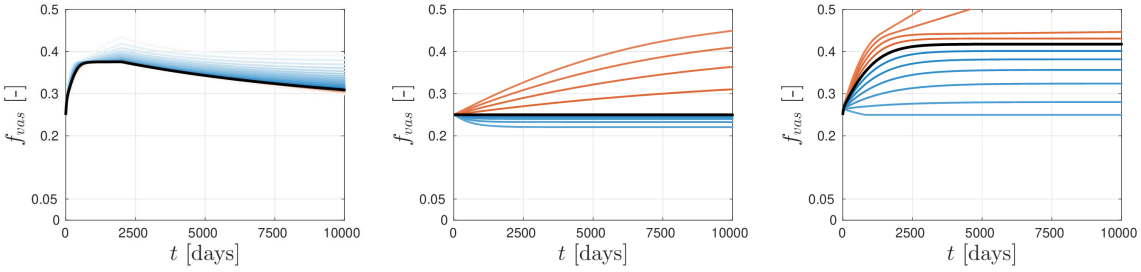

(a) L I, $R_{act}^{TGF-\beta}$ (b) L II, $R_{act}^{TGF-\beta}$ (c) L III, $R_{act}^{TGF-\beta}$

Figure A.10: Model-predicted vascular porosities over time, when applying the OFAT-method for the parameter $R_{act}^{TGF-\beta}$ and all three load cases, for $f_{vas,ini} = 0.25$.

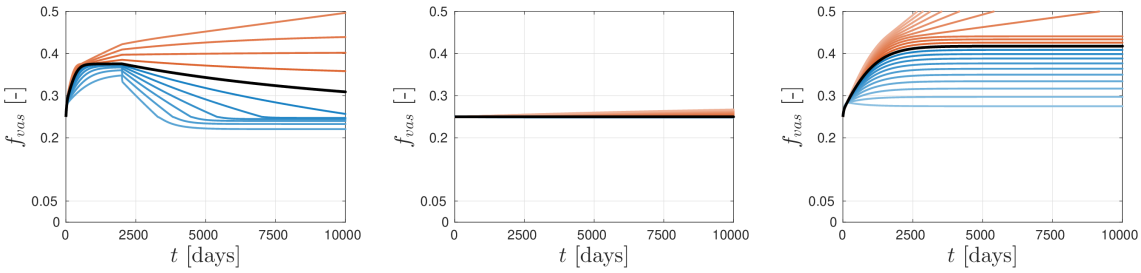

(a) L I, $R_{rep}^{TGF-\beta}$ (b) L II, $R_{rep}^{TGF-\beta}$ (c) L III, $R_{rep}^{TGF-\beta}$

Figure A.11: Model-predicted vascular porosities over time, when applying the OFAT-method for the parameter $R_{rep}^{TGF-\beta}$ and all three load cases, for $f_{vas,ini} = 0.25$.

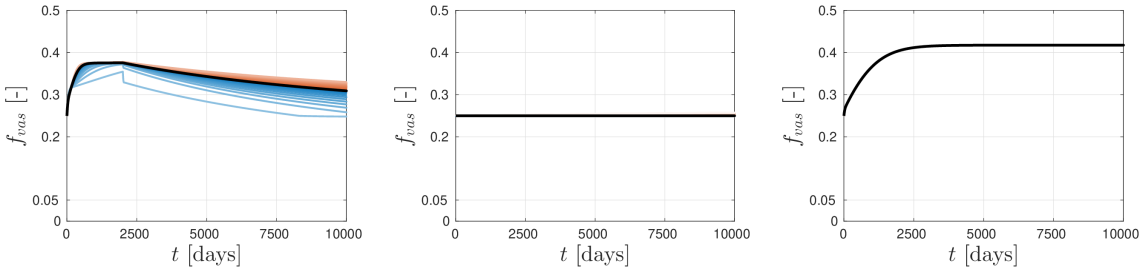

(a) L I, R^{max}_{RANKL} (b) L II, R^{max}_{RANKL} (c) L III, R^{max}_{RANKL}

Figure A.12: Model-predicted vascular porosities over time, when applying the OFAT-method for the parameter R^{max}_{RANKL} and all three load cases, for $f_{vas,ini} = 0.25$.

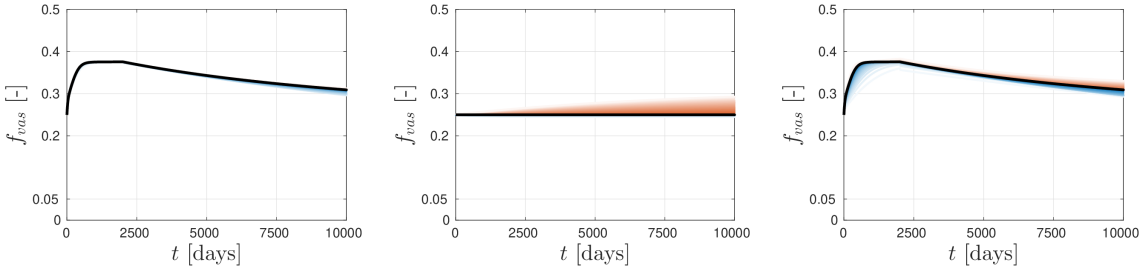

(a) L I, R^{max}_{OPG} (b) L II, R^{max}_{OPG} (c) L III, R^{max}_{OPG}

Figure A.13: Model-predicted vascular porosities over time, when applying the OFAT-method for the parameter R^{max}_{OPG} and all three load cases, for $f_{vas,ini} = 0.25$.

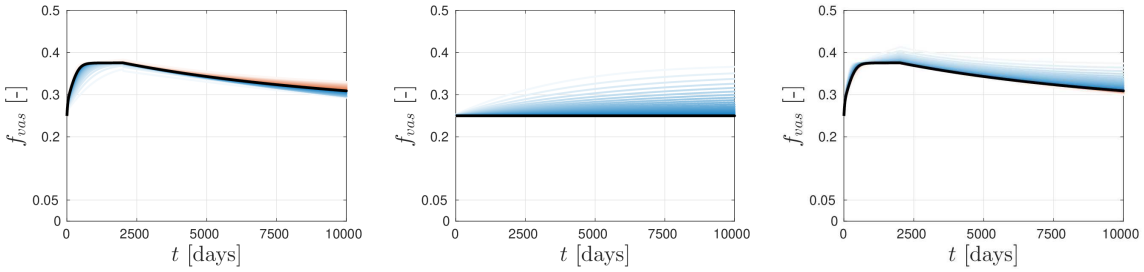

(a) L I, R_{RANKL} (b) L II, R_{RANKL} (c) L III, R_{RANKL}

Figure A.14: Model-predicted vascular porosities over time, when applying the OFAT-method for the parameter R_{RANKL} and all three load cases, for $f_{vas,ini} = 0.25$.

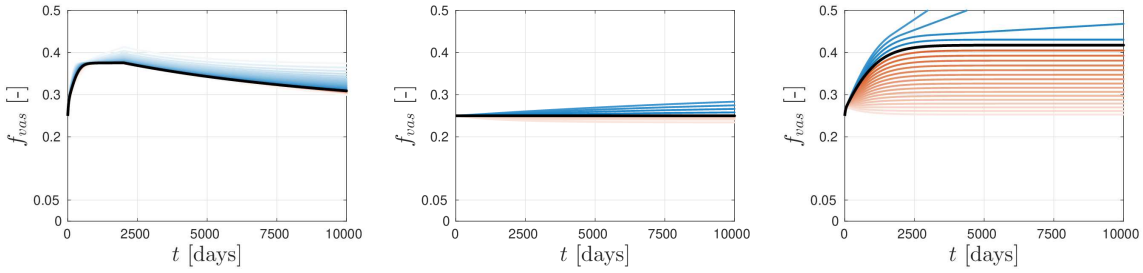

(a) L I, $\mathcal{P}_{OBp}$ (b) L II, $\mathcal{P}_{OBp}$ (c) L III, $\mathcal{P}_{OBp}$

Figure A.15: Model-predicted vascular porosities over time, when applying the OFAT-method for the parameter $\mathcal{P}_{OBp}$ and all three load cases, for $f_{vas,ini} = 0.25$.

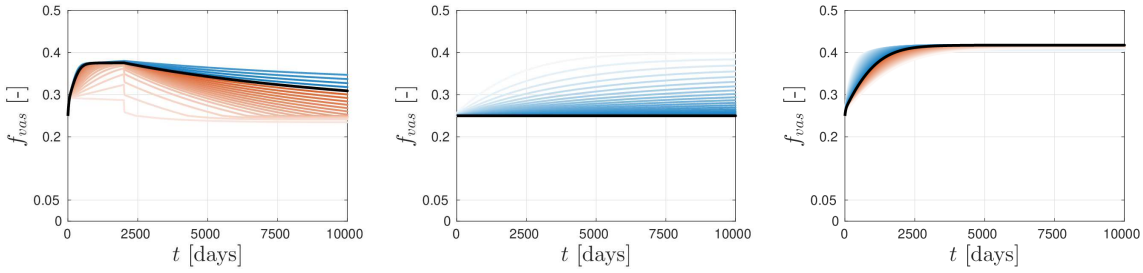

(a) L I, $K_{act,OCp}^{[RANKL-RANK]}$ (b) L II, $K_{act,OCp}^{[RANKL-RANK]}$ (c) L III, $K_{act,OCp}^{[RANKL-RANK]}$

Figure A.16: Model-predicted vascular porosities over time, when applying the OFAT-method for the parameter $K_{act,OCp}^{[RANKL-RANK]}$ and all three load cases, for $f_{vas,ini} = 0.25$.

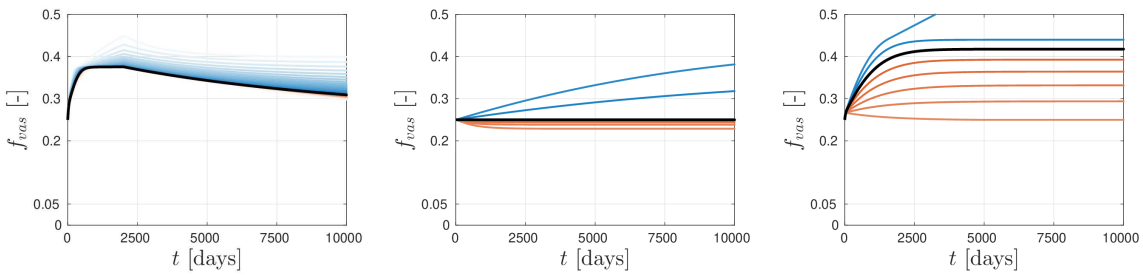

(a) L I, k_{form} (b) L II, k_{form} (c) L III, k_{form}

Figure A.17: Model-predicted vascular porosities over time, when applying the OFAT-method for the parameter k_{form} and all three load cases, for $f_{vas,ini} = 0.25$.

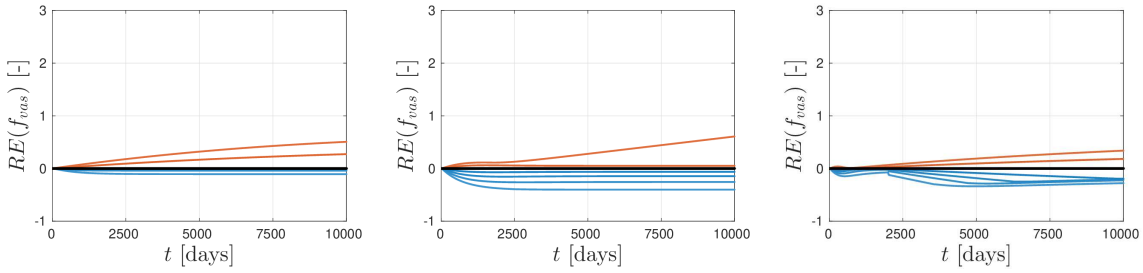

(a) L I, $\mathcal{A}_{OBa}$ (b) L II, $\mathcal{A}_{OBa}$ (c) L III, $\mathcal{A}_{OBa}$

Figure A.18: Relative errors of model-predicted vascular porosities over time for the parameter $\mathcal{A}_{OBa}$ and all three load cases, for $f_{vas,ini} = 0.25$.

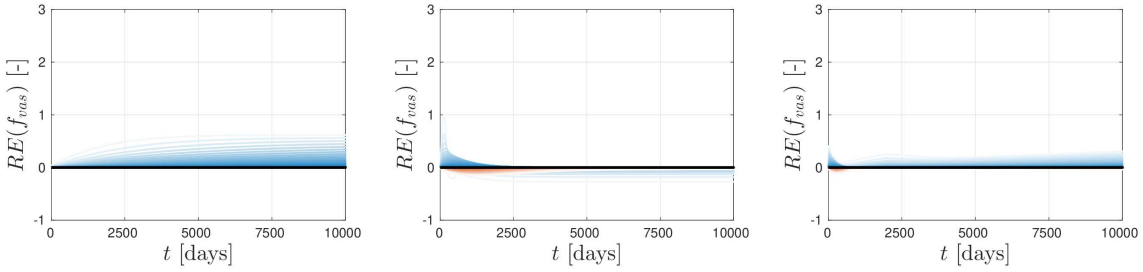

(a) L I, $\mathcal{A}_{OCa}$ (b) L II, $\mathcal{A}_{OCa}$ (c) L III, $\mathcal{A}_{OCa}$

Figure A.19: Relative errors of model-predicted vascular porosities over time for the parameter $\mathcal{A}_{OCa}$ and all three load cases, for $f_{vas,ini} = 0.25$.

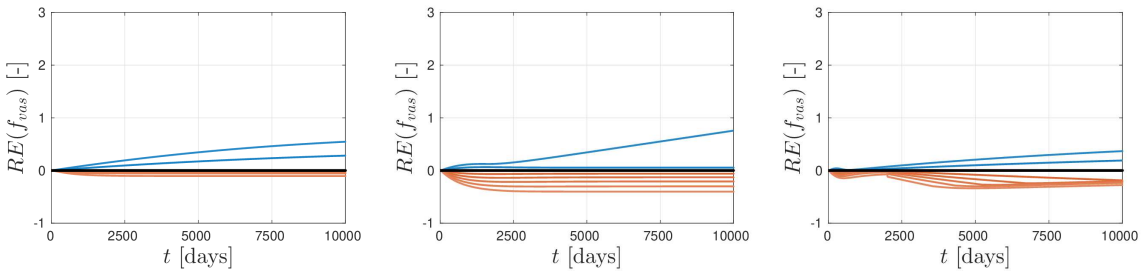

(a) L I, $\mathcal{D}_{OBu}$ (b) L II, $\mathcal{D}_{OBu}$ (c) L III, $\mathcal{D}_{OBu}$

Figure A.20: Relative errors of model-predicted vascular porosities over time for the parameter $\mathcal{D}_{OBu}$ and all three load cases, for $f_{vas,ini} = 0.25$.

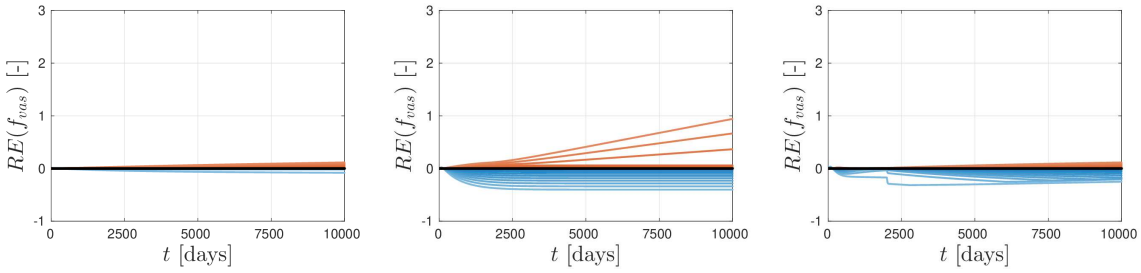

(a) L I, $\mathcal{D}_{OBp}$ (b) L II, $\mathcal{D}_{OBp}$ (c) L III, $\mathcal{D}_{OBp}$

Figure A.21: Relative errors of model-predicted vascular porosities over time for the parameter $\mathcal{D}_{OBp}$ and all three load cases, for $f_{vas,ini} = 0.25$.

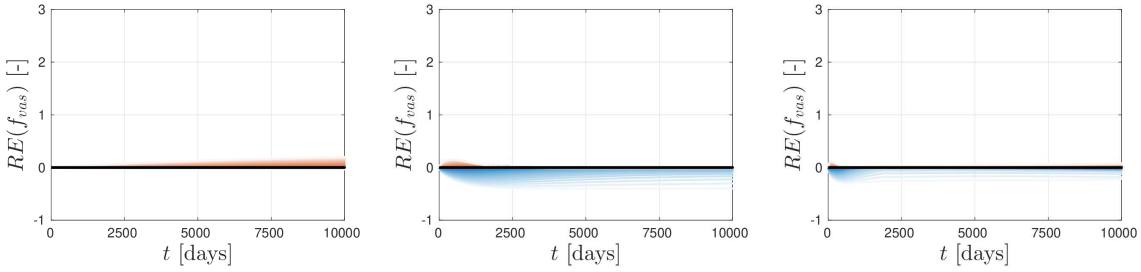

(a) L I, $\mathcal{D}_{OCp}$ (b) L II, $\mathcal{D}_{OCp}$ (c) L III, $\mathcal{D}_{OCp}$

Figure A.22: Relative errors of model-predicted vascular porosities over time for the parameter $\mathcal{D}_{OCp}$ and all three load cases, for $f_{vas,ini} = 0.25$.

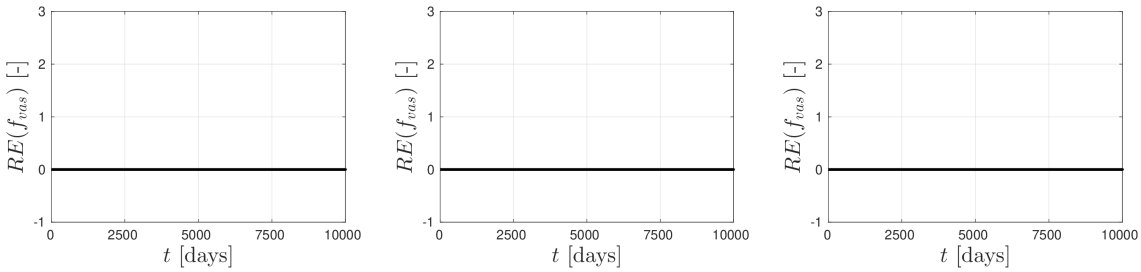

(a) L I, C_{OPG}^{max} (b) L II, C_{OPG}^{max} (c) L III, C_{OPG}^{max}

Figure A.23: Relative errors of model-predicted vascular porosities over time for the parameter C_{OPG}^{max} and all three load cases, for $f_{vas,ini} = 0.25$.

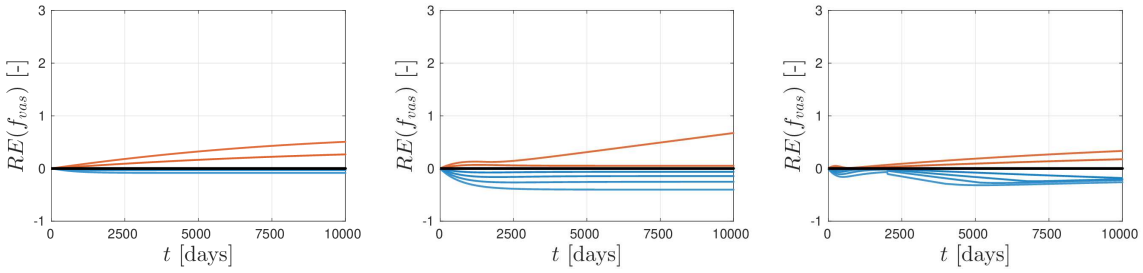

(a) L I, k_{res} (b) L II, k_{res} (c) L III, k_{res}

Figure A.24: Relative errors of model-predicted vascular porosities over time for the parameter k_{res} and all three load cases, for $f_{vas,ini} = 0.25$.

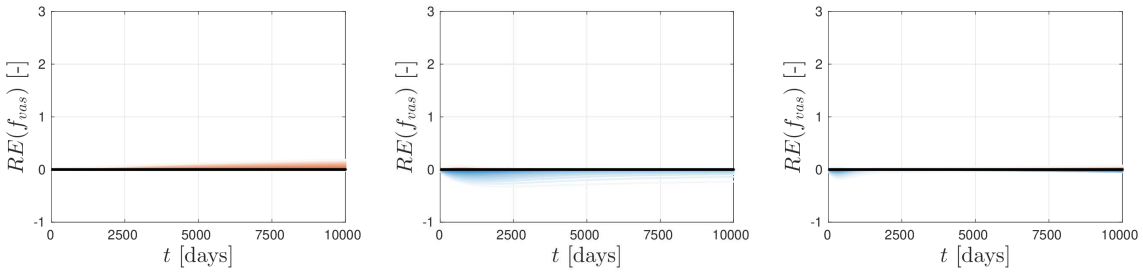

(a) L I, $K_{a,[RANKL-RANK]}$ (b) L II, $K_{a,[RANKL-RANK]}$ (c) L III, $K_{a,[RANKL-RANK]}$

Figure A.25: Relative errors of model-predicted vascular porosities over time for the parameter $K_{a,[RANKL-RANK]}$ and all three load cases, for $f_{vas,ini} = 0.25$.

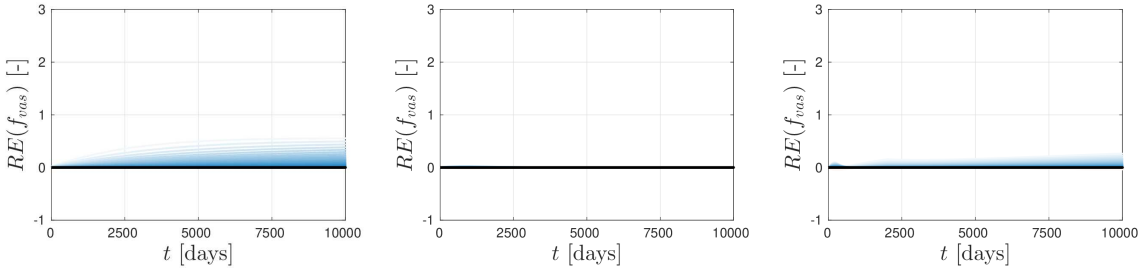

(a) L I, $K_{a,[RANKL-OPG]}$ (b) L II, $K_{a,[RANKL-OPG]}$ (c) L III, $K_{a,[RANKL-OPG]}$

Figure A.26: Relative errors of model-predicted vascular porosities over time for the parameter $K_{a,[RANKL-OPG]}$ and all three load cases, for $f_{vas,ini} = 0.25$.

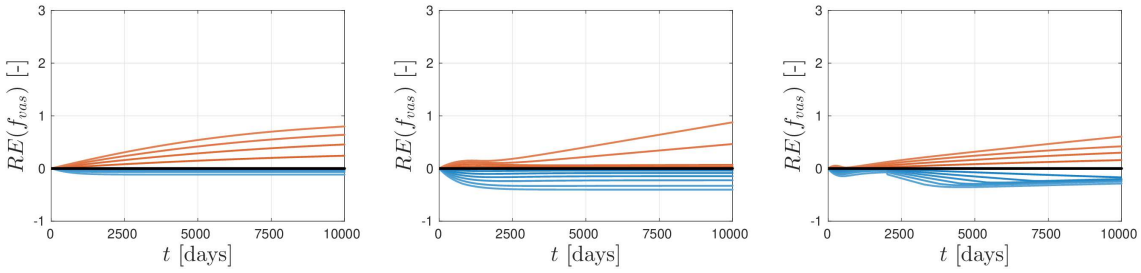

(a) L I, $R_{act}^{TGF-\beta}$ (b) L II, $R_{act}^{TGF-\beta}$ (c) L III, $R_{act}^{TGF-\beta}$

Figure A.27: Relative errors of model-predicted vascular porosities over time for the parameter $R_{act}^{TGF-\beta}$ and all three load cases, for $f_{vas,ini} = 0.25$.

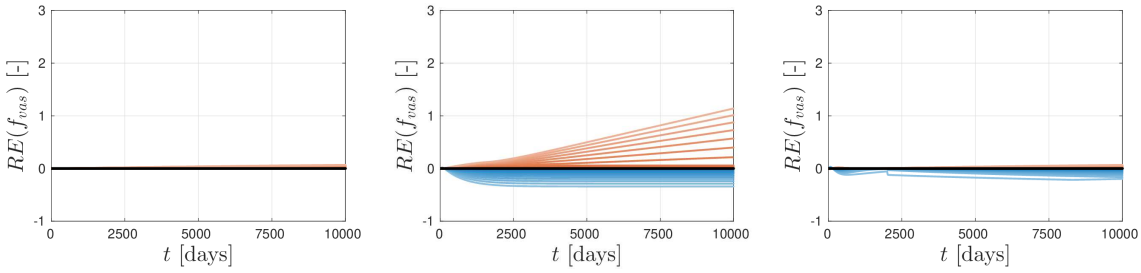

(a) L I, $R_{rep}^{TGF-\beta}$ (b) L II, $R_{rep}^{TGF-\beta}$ (c) L III, $R_{rep}^{TGF-\beta}$

Figure A.28: Relative errors of model-predicted vascular porosities over time for the parameter $R_{rep}^{TGF-\beta}$ and all three load cases, for $f_{vas,ini} = 0.25$.

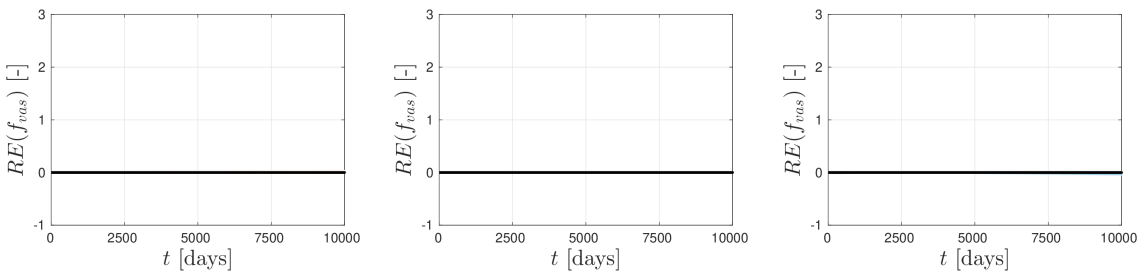

(a) L I, R_{RANKL}^{max} (b) L II, R_{RANKL}^{max} (c) L III, R_{RANKL}^{max}

Figure A.29: Relative errors of model-predicted vascular porosities over time for the parameter R_{RANKL}^{max} and all three load cases, for $f_{vas,ini} = 0.25$.

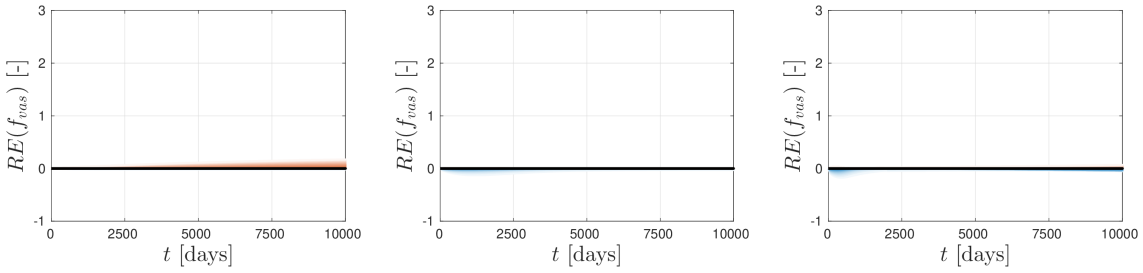

(a) L I, R^{max}_{OPG} (b) L II, R^{max}_{OPG} (c) L III, R^{max}_{OPG}

Figure A.30: Relative errors of model-predicted vascular porosities over time for the parameter R^{max}_{OPG} and all three load cases, for $f_{vas,ini} = 0.25$.

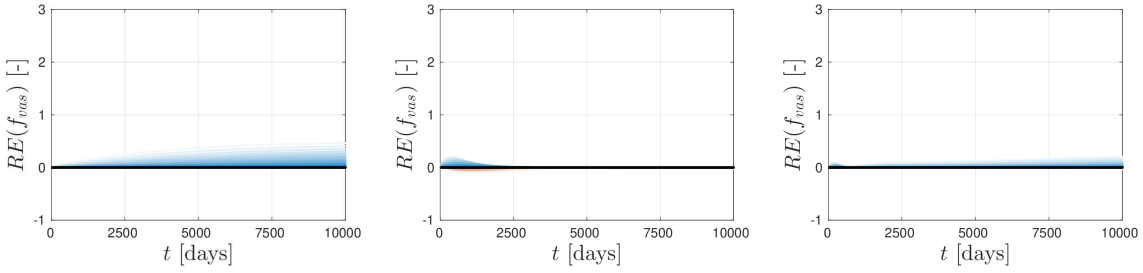

(a) L I, R_{RANKL} (b) L II, R_{RANKL} (c) L III, R_{RANKL}

Figure A.31: Relative errors of model-predicted vascular porosities over time for the parameter R_{RANKL} and all three load cases, for $f_{vas,ini} = 0.25$.

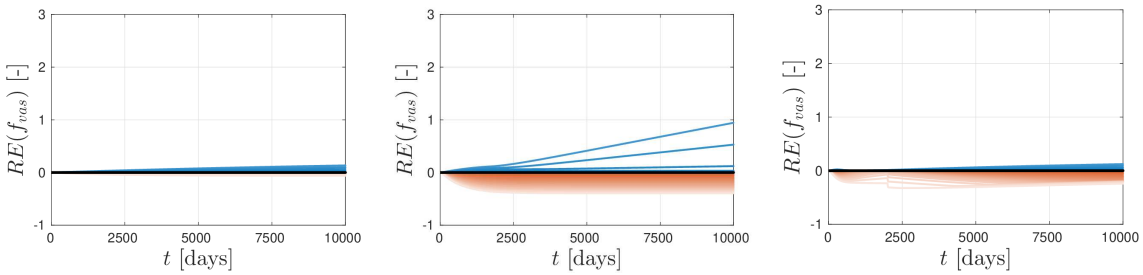

(a) L I, $\mathcal{P}_{OBp}$ (b) L II, $\mathcal{P}_{OBp}$ (c) L III, $\mathcal{P}_{OBp}$

Figure A.32: Relative errors of model-predicted vascular porosities over time for the parameter $\mathcal{P}_{OBp}$ and all three load cases, for $f_{vas,ini} = 0.25$.

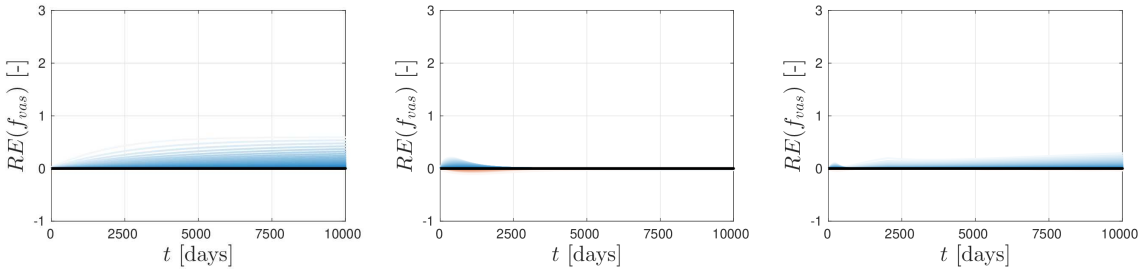

(a) L I, $K_{act,OCp}^{[RANKL-RANK]}$ (b) L II, $K_{act,OCp}^{[RANKL-RANK]}$ (c) L III, $K_{act,OCp}^{[RANKL-RANK]}$

Figure A.33: Relative errors of model-predicted vascular porosities over time for the parameter $K_{act,OCp}^{[RANKL-RANK]}$ and all three load cases, for $f_{vas,ini} = 0.25$.

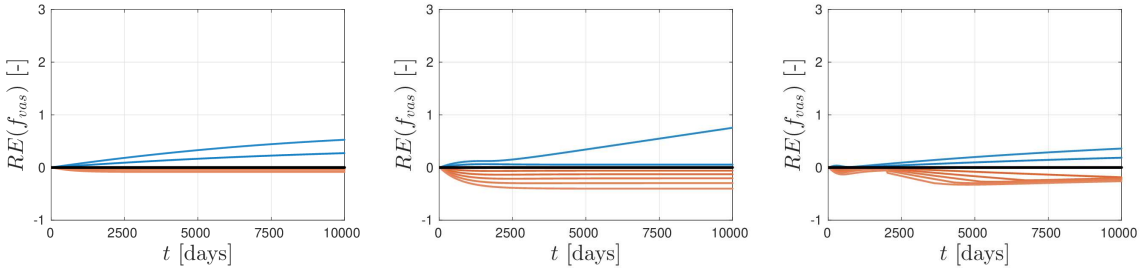

(a) L I, k_{form} (b) L II, k_{form} (c) L III, k_{form}

Figure A.34: Relative errors of model-predicted vascular porosities over time for the parameter k_{form} and all three load cases, for $f_{vas,ini} = 0.25$.

Appendix B

Matlab code

```
function bone_remodeling_model(scenario)

%initial values
C_OB_p0 = 0.001;
C_OB_a0 = 0.0005;
C_OC_a0 = 0.0001;
f_vas0 = 0.05;
f_bm0 = 1-f_vas0;

%%%%%%%%%%%%%%%%%%%%%% calculation of steady-state values %%%%%%%%%%%%%%%%%%%

%vector of state variables with initial values
x0 = zeros(4,1);
x0(1) = C_OB_p0;
x0(2) = C_OB_a0;
x0(3) = C_OC_a0;
x0(4) = f_vas0;

%definitions for the calculation of SED
c_bm = [ [18.5, 10.3, 10.4, 0, 0, 0]; [10.3, 20.8, 11.0, 0, 0, 0];
[10.4, 11.0, 28.4, 0, 0, 0]; [0, 0, 0, 12.9, 0, 0]; [0, 0, 0, 0, 11.5, 0];
[0, 0, 0, 0, 0, 9.3] ];
inc_phi = 2*pi / 50;
Pcyl = FU_P_cylincl_orthomat(c_bm, inc_phi);
II = eye(6);
KK = 1/3 * [ones(3),zeros(3);zeros(3),zeros(3)];
JJ = II-KK;
```

```
kvas = 2.3;
c_vas = 3*kvas*KK;

%definition of the different stress tensors
stress_normal = FU_mat2vec([[0,0,0];[0,0,0];[0,0,-30]]*1e-3);
stress_disuse = FU_mat2vec([[0,0,0];[0,0,0];[0,0,-25]]*1e-3);

%calculation of the initial SED
deno = inv(x0(4)*inv(II+Pcyl*(c_vas-c_bm)) + (1-x0(4))*II);
A_vas = inv(II + Pcyl*(c_vas-c_bm)) * deno;
A_bm = II*deno;
C_cort_hom = x0(4)*c_vas*A_vas + (1-x0(4))*c_bm*A_bm;
eps_bm0 = A_bm*(inv(C_cort_hom)*stress_normal');
SED_bm0 = 0.5 * eps_bm0' * c_bm * eps_bm0;

%%%%%%%%%%%%%%%%%%%%%%%%%%%%%% simulation %%%%%%%%%%%%%%%%%%%%%%%%%%%%%%

tspan = [0 10000];
global SED_vec
global time
time=[];
SED_vec=[];
%solving the ODE-system
options = odeset('RelTol',1e-6,'AbsTol',1e-6,'MaxStep',5);
tic
[t, y] = ode23s(@(t,x) cell_population_equations(t,x,Pcyl,SED_bm0,scenario),
tspan, x0, options);
toc

%%%%%%%%%%%%%%%%%%%%%%%%%%%%%%%% PLOTS %%%%%%%%%%%%%%%%%%%%%%%%%%%%%%%%

%cell concentrations
figure
hold on
plot(t, y(:,1)/C_OB_p0, '-', 'Linewidth', 2);
plot(t, y(:,2)/C_OB_a0, '--', 'Linewidth', 2);
plot(t, y(:,3)/C_OC_a0, ':', 'Linewidth', 2);
axis([0 10000 0 10])
legend('OB_p','OB_a','OC_a')
```

```
xlabel('t [days]')
ylabel('C_i(t) / C_i(0)')
hold off

%vascular porosity
figure(2)
hold on
plot(t, y(:,4),'Linewidth', 2);
plot([0 10000], [max(y(:,4)) max(y(:,4))], 'k--', 'Linewidth', 1)
axis([0 10000 0 0.35])
xlabel('t [days]')
ylabel('f_{vas}')
hold off

%strain energy density
figure(3)
plot(time, SED_vec, 'Linewidth', 2);
axis([0 10000 0.6 1.8])
xlabel('t [days]')
ylabel('\Psi_{bm}(t) / \Psi_{bm}(0)')

end

%%%%%%%%%%%%%%%%%%%%%%%%%%%% model equations %%%%%%%%%%%%%%%%%%%%%%%%%%%%

function xdot = cell_population_equations(t, x, Pcyl, SED_bm0,scenario)

%parameter values
A_OB_a = 2.1107e-1;
A_OC_a = 5.6487;
D_OB_u = 6.3e-2;
D_OB_p = 1.657e-1;
D_OC_p = 2.1;
C_OPG_max = 2e8;
k_res = 2;
K_a_RR = 3.4117e-2;
K_a_RO = 1e-3;
R_act_TGFb = 5.6328e-4;
R_rep_TGFb = 1.7543e-4;
```

```
R_RANKL_max = 5.1396e4;
R_OPG_max = 3.0285e-8;
R_RANKL = 6.0163e-2;
P_OB_p = 0.021107079892170;
K_act_OCp_RR = 5.6797;
k_form = 0.4;

%parameters that are changed in the PMO scenario
if strcmp(scenario,'PMO')
    R_RANKL_max = 2.1512e6;
    R_OPG_max = 5.6568e-6;
end

%constant cell concentrations
C_OB_u = 0.01;
C_OC_p = 0.001;

%constant RANKL-concentration
C_RANK = C_OC_p * 1e4;

%calculation of SED for every time step
II = eye(6);
KK = 1/3 * [ones(3),zeros(3);zeros(3),zeros(3)];
JJ = II-KK;
kvas = 2.3;
c_vas = 3*kvas*KK;

c_bm = [ [18.5, 10.3, 10.4, 0, 0, 0]; [10.3, 20.8, 11.0, 0, 0, 0];
[10.4, 11.0, 28.4, 0, 0, 0]; [0, 0, 0, 12.9, 0, 0]; [0, 0, 0, 0, 11.5, 0];
[0, 0, 0, 0, 0, 9.3] ];
inc_phi = 2*pi / 50;

stress_normal = FU_mat2vec([[0,0,0];[0,0,0];[0,0,-30]]*1e-3);
stress_disuse = FU_mat2vec([[0,0,0];[0,0,0];[0,0,-25]]*1e-3);

deno = inv(x(4)*inv(II+Pcyl*(c_vas-c_bm)) + (1-x(4))*II);
A_vas = inv(II + Pcyl*(c_vas-c_bm)) * deno;
A_bm = II*deno;
C_cort_hom = x(4)*c_vas*A_vas + (1-x(4))*c_bm*A_bm;
```

```
%in disuse scenario the stress is lowered in the beginning
if strcmp(scenario,'disuse')
    if t<2000
        stress = stress_disuse;
    else
        stress = stress_normal;
    end
else
    stress = stress_normal;
end

eps_bm = A_bm*(inv(C_cort_hom)*stress');
SED_bm = 0.5 * eps_bm' * c_bm * eps_bm;

global SED_vec
global time
SED = SED_bm/SED_bm0;
SED_vec = [SED_vec, SED];
time = [time, t];
lambda = 1.25;

%calculation of the functions pi_act_OB_p_mech und P_RANKL, depending on SED
if SED < 1
    pi_act_OB_p_mech = 0.5;
    P_RANKL_new = 1e3/1.6841 * (1-SED);
elseif SED <= (1/lambda + 1)
    pi_act_OB_p_mech = 0.5 * (1+lambda*(SED-1));
    P_RANKL_new = 0;
else
    pi_act_OB_p_mech = 1;
    P_RANKL_new = 0;
end


%equations of the BCPM
C_RANKL_max = R_RANKL_max * x(1);
C_OPG = 1/((1/C_OPG_max)+(R_OPG_max/x(2)));
C_RANKL = C_RANKL_max*(1+P_RANKL_new)/
```

```
((1+R_RANKL*C_RANKL_max)*(1+K_a_RO*C_OPG+K_a_RR*C_RANK));
C_RR = K_a_RR*C_RANKL*C_RANK;
pi_act_OC_p_RANKL = C_RR/(K_act_Ocp_RR+C_RR);
pi_act_TGFb = x(3)/(R_act_TGFb+x(3));
pi_rep_TGFb = R_rep_TGFb/(R_rep_TGFb+x(3));

%ODE system
xdot = zeros(4,1);
xdot(1) = D_OB_u*pi_act_TGFb*C_OB_u + P_OB_p*pi_act_OB_p_mech*x(1)
- D_OB_p*pi_rep_TGFb*x(1);
xdot(2) = D_OB_p*pi_rep_TGFb*x(1) - A_OB_a*x(2);
xdot(3) = D_OC_p*pi_act_OC_p_RANKL*C_OC_p - A_OC_a*pi_act_TGFb*x(3);
xdot(4) = k_res*x(3) - k_form*x(2);

end
```

Bibliography

Alliston, T., Choy, L., Ducy, P., Karsenty, G., and Derynck, R. (2001). TGF-β-induced repression of CBFA1 by Smad3 decreases cbfa1 and osteocalcin expression and inhibits osteoblast differentiation. *The EMBO Journal*, 20(9):2254–2272.

Alon, U. (2006). *An introduction to systems biology: design principles of biological circuits*. CRC press, Boca Raton, Florida.

Bertrand, E. and Hellmich, C. (2009). Multiscale elasticity of tissue engineering scaffolds with tissue-engineered bone: a continuum micromechanics approach. *Journal of Engineering Mechanics*, 135(5):395–412.

Black, D. M. and Rosen, C. J. (2016). Postmenopausal osteoporosis. *New England Journal of Medicine*, 374(3):254–262.

Bonewald, L. F. (2011). The amazing osteocyte. *Journal of Bone and Mineral Research*, 26(2):229–238.

Bonewald, L. F. and Dallas, S. (1994). Role of active and latent transforming growth factor β in bone formation. *Journal of Cellular Biochemistry*, 55(3):350–357.

Bonnet, N. and Ferrari, S. L. (2010). Exercise and the skeleton: how it works and what it really does. *IBMS BoneKEy*, 7(7):235–248.

Boyce, B. F. and Xing, L. (2008). Functions of RANKL/RANK/OPG in bone modeling and remodeling. *Archives of Biochemistry and Biophysics*, 473(2):139–146.

Carter, D. R. and Beaupré, G. S. (2007). *Skeletal function and form: mechanobiology of skeletal development, aging, and regeneration*. Cambridge University Press, Cambridge.

Dejaco, A., Komlev, V. S., Jaroszewicz, J., Swieszkowski, W., and Hellmich, C. (2012). Micro CT-based multiscale elasticity of double-porous (pre-cracked) hydroxyapatite granules for regenerative medicine. *Journal of Biomechanics*, 45(6):1068–1075.

Del Fattore, A., Teti, A., and Rucci, N. (2012). Bone cells and the mechanisms of bone remodelling. *Frontiers in Bioscience (Elite Ed)*, 4:2302–2321.

Erlebacher, A., Filvaroff, E. H., Ye, J.-Q., and Derynck, R. (1998). Osteoblastic responses to TGF-β during bone remodeling. *Molecular Biology of the Cell*, 9(7):1903–1918.

Felson, D. T., Zhang, Y., Hannan, M. T., Kiel, D. P., Wilson, P., and Anderson, J. J. (1993). The effect of postmenopausal estrogen therapy on bone density in elderly women. *New England Journal of Medicine*, 329(16):1141–1146.

Feng, X. and McDonald, J. M. (2011). Disorders of bone remodeling. *Annual Review of Pathology: Mechanisms of Disease*, 6:121–145.

Fritsch, A., Dormieux, L., and Hellmich, C. (2006). Porous polycrystals built up by uniformly and axisymmetrically oriented needles: homogenization of elastic properties. *Comptes Rendus Mécanique*, 334(3):151–157.

Fritsch, A. and Hellmich, C. (2007). 'universal'microstructural patterns in cortical and trabecular, extracellular and extravascular bone materials: micromechanics-based prediction of anisotropic elasticity. *Journal of Theoretical Biology*, 244(4):597–620.

Hadjidakis, D. J. and Androulakis, I. I. (2006). Bone remodeling. *Annals of the New York Academy of Sciences*, 1092(1):385–396.

Hambli, R., Katerchi, H., and Benhamou, C.-L. (2011). Multiscale methodology for bone remodelling simulation using coupled finite element and neural network computation. *Biomechanics and Modeling in Mechanobiology*, 10(1):133–145.

Hamburg, M. A. and Collins, F. S. (2010). The path to personalized medicine. *New England Journal of Medicine*, 363(4):301–304.

Hellmich, C. (2005). Microelasticity of bone. In *CISM 480 Applied Micromechanics of Porous Materials (L. Dormieux and F. J. Ulm Eds)*, pages 289–331. Springer, Wien, New York.

Hellmich, C., Kober, C., and Erdmann, B. (2008). Micromechanics-based conversion of CT data into anisotropic elasticity tensors, applied to FE simulations of a mandible. *Annals of Biomedical Engineering*, 36(1):108.

Hellmich, C., Ulm, F.-J., and Dormieux, L. (2004). Can the diverse elastic properties of trabecular and cortical bone be attributed to only a few tissue-independent phase properties and their interactions? *Biomechanics and Modeling in Mechanobiology*, 2(4):219–238.

Hill, R. (1963). Elastic properties of reinforced solids: some theoretical principles. *Journal of the Mechanics and Physics of Solids*, 11(5):357–372.

Hill, R. (1965). Continuum micro-mechanics of elastoplastic polycrystals. *Journal of the Mechanics and Physics of Solids*, 13(2):89–101.

Holzapfel, G. A., Gasser, T. C., and Ogden, R. W. (2000). A new constitutive framework for arterial wall mechanics and a comparative study of material models. *Journal of Elasticity*, 61(1-3):1–48.

Horsman, A., Jones, M., Francis, R., and Nordin, C. (1983). The effect of estrogen dose on postmenopausal bone loss. *New England Journal of Medicine*, 309(23):1405–1407.

Hruska, K. A. and Teitelbaum, S. L. (1995). Renal osteodystrophy. *New England Journal of Medicine*, 333(3):166–175.

Jacobs, C. R. (2000). The mechanobiology of cancellous bone structural adaptation. *Journal of Rehabilitation Research and Development*, 37(2):209–216.

Kanis, J. A., Melton III, L. J., Christiansen, C., Johnston, C. C., and Khaltaev, N. (1994). The diagnosis of osteoporosis. *Journal of Bone and Mineral Research*, 9(8):1137–1141.

Kobayashi, S., Inoue, S., Hosoi, T., Ouchi, Y., Shiraki, M., and Orimo, H. (1996). Association of bone mineral density with polymorphism of the estrogen receptor gene. *Journal of Bone and Mineral Research*, 11(3):306–311.

Lees, S., Ahern, J., and Leonard, M. (1983). Parameters influencing the sonic velocity in compact calcified tissues of various species. *The Journal of the Acoustical Society of America*, 74(1):28–33.

Lees, S., Tao, N.-J., and Lindsay, S. (1990). Studies of compact hard tissues and collagen by means of brillouin light scattering. *Connective Tissue Research*, 24(3-4):187–205.

Lemaire, V., Tobin, F. L., Greller, L. D., Cho, C. R., and Suva, L. J. (2004). Modeling the interactions between osteoblast and osteoclast activities in bone remodeling. *Journal of Theoretical Biology*, 229(3):293–309.

Martin, R. B., Burr, D. B., Sharkey, N. A., et al. (1998). *Skeletal tissue mechanics*, volume 190. Springer, New York.

Mishnaevsky, L. L. and Schmauder, S. (2001). Continuum mesomechanical finite element modeling in materials development: A state-of-the-art review. *Applied Mechanics Reviews*, 54(1):49–67.

Mulvihill, B. M. and Prendergast, P. J. (2010). Mechanobiological regulation of the remodelling cycle in trabecular bone and possible biomechanical pathways for osteoporosis. *Clinical Biomechanics*, 25(5):491–498.

O'Hagan, A., Buck, C. E., Daneshkhah, A., Eiser, J. R., Garthwaite, P. H., Jenkinson, D. J., Oakley, J. E., and Rakow, T. (2006). *Uncertain judgements: eliciting experts' probabilities*. John Wiley & Sons, Chichester.

Pannell, D. J. et al. (1997). Sensitivity analysis of normative economic models: theoretical framework and practical strategies. *Agricultural Economics*, 16(2):139–152.

Papachroni, K. K., Karatzas, D. N., Papavassiliou, K. A., Basdra, E. K., and Papavassiliou, A. G. (2009). Mechanotransduction in osteoblast regulation and bone disease. *Trends in Molecular Medicine*, 15(5):208–216.

Pastrama, M.-I., Scheiner, S., Pivonka, P., and Hellmich, C. (2018). A mathematical multiscale model of bone remodeling, accounting for pore space-specific mechanosensation. *Bone*, 107:208–221.

Pivonka, P., Buenzli, P. R., Scheiner, S., Hellmich, C., and Dunstan, C. R. (2013). The influence of bone surface availability in bone remodelling — a mathematical model including coupled geometrical and biomechanical regulations of bone cells. *Engineering Structures*, 47:134–147.

Pivonka, P., Zimak, J., Smith, D. W., Gardiner, B. S., Dunstan, C. R., Sims, N. A., Martin, T. J., and Mundy, G. R. (2008). Model structure and control of bone remodeling: a theoretical study. *Bone*, 43(2):249–263.

Pivonka, P., Zimak, J., Smith, D. W., Gardiner, B. S., Dunstan, C. R., Sims, N. A., Martin, T. J., and Mundy, G. R. (2010). Theoretical investigation of the role of the RANK–RANKL–OPG system in bone remodeling. *Journal of Theoretical Biology*, 262(2):306–316.

Raggatt, L. J. and Partridge, N. C. (2010). Cellular and molecular mechanisms of bone remodelling. *Journal of Biological Chemistry*, pages jbc–R109.

Ralston, S. H. and Layfield, R. (2012). Pathogenesis of paget disease of bone. *Calcified Tissue International*, 91(2):97–113.

Rubin, J., Fan, X., Biskobing, D., Taylor, W., and Rubin, C. (1999). Osteoclastogenesis is repressed by mechanical strain in an in vitro model. *Journal of Orthopaedic Research*, 17(5):639–645.

Rubin, J., Murphy, T. C., Fan, X., Goldschmidt, M., and Taylor, W. R. (2002). Activation of extracellular signal–regulated kinase is involved in mechanical strain inhibition of RANKL expression in bone stromal cells. *Journal of Bone and Mineral Research*, 17(8):1452–1460.

Rubin, J., Rubin, C., and Jacobs, C. R. (2006). Molecular pathways mediating mechanical signaling in bone. *Gene*, 367:1–16.

Rucci, N. (2008). Molecular biology of bone remodelling. *Clinical Cases in Mineral and Bone Metabolism*, 5(1):49.

Sacks, J., Welch, W. J., Mitchell, T. J., and Wynn, H. P. (1989). Design and analysis of computer experiments. *Statistical Science*, pages 409–423.

Saxena, R., Pan, G., Dohm, E. D., and McDonald, J. M. (2011). Modeled microgravity and hindlimb unloading sensitize osteoclast precursors to RANKL-mediated osteoclastogenesis. *Journal of Bone and Mineral Metabolism*, 29(1):111–122.

Scheiner, S., Pivonka, P., and Hellmich, C. (2013). Coupling systems biology with multiscale mechanics, for computer simulations of bone remodeling. *Computer Methods in Applied Mechanics and Engineering*, 254:181–196.

Scheiner, S., Pivonka, P., Smith, D., Dunstan, C., and Hellmich, C. (2014). Mathematical modeling of postmenopausal osteoporosis and its treatment by the anti-catabolic drug denosumab. *International Journal for Numerical Methods in Biomedical Engineering*, 30(1):1–27.

Seeman, E. (2009). Bone modeling and remodeling. *Critical Reviews in Eukaryotic Gene Expression*, 19(3).

Sims, N. A. and Martin, T. J. (2014). Coupling the activities of bone formation and resorption: a multitude of signals within the basic multicellular unit. *BoneKEy Reports*, 3.

Sözen, T., Özışık, L., and Başaran, N. Ç. (2017). An overview and management of osteoporosis. *European Journal of Rheumatology*, 4(1):46.

Stein, E. and Shane, E. (2003). Secondary osteoporosis. *Endocrinology and Metabolism Clinics of North America*, 32(1):115–34.

Suda, T., Takahashi, N., Udagawa, N., Jimi, E., Gillespie, M. T., and Martin, T. J. (1999). Modulation of osteoclast differentiation and function by the new members of the tumor necrosis factor receptor and ligand families. *Endocrine Reviews*, 20(3):345–357.

Tolar, J., Teitelbaum, S. L., and Orchard, P. J. (2004). Osteopetrosis. *New England Journal of Medicine*, 351(27):2839–2849.

Turner, C. H., Rho, J., Takano, Y., Tsui, T. Y., and Pharr, G. M. (1999). The elastic properties of trabecular and cortical bone tissues are similar: results from two microscopic measurement techniques. *Journal of Biomechanics*, 32(4):437–441.

Weinans, H., Huiskes, R., and Grootenboer, H. (1992). The behavior of adaptive bone-remodeling simulation models. *Journal of Biomechanics*, 25(12):1425–1441.

Wharton, B. and Bishop, N. (2003). Rickets. *The Lancet*, 362(9393):1389–1400.

Wiltink, A., Nijweide, P. J., Scheenen, W. J., Ypey, D. L., and Van Duijn, B. (1995). Cell membrane stretch in osteoclasts triggers a self-reinforcing Ca^{2+} entry pathway. *Pflügers Archiv*, 429(5):663–671.

Xing, L. and Boyce, B. F. (2005). Regulation of apoptosis in osteoclasts and osteoblastic cells. *Biochemical and Biophysical Research Communications*, 328(3):709–720.

Yosibash, Z., Trabelsi, N., and Hellmich, C. (2008). Subject-specific p-FE analysis of the proximal femur utilizing micromechanics-based material properties. *International Journal for Multiscale Computational Engineering*, 6(5).

Zaoui, A. (2002). Continuum micromechanics: survey. *Journal of Engineering Mechanics*, 128(8):808–816.